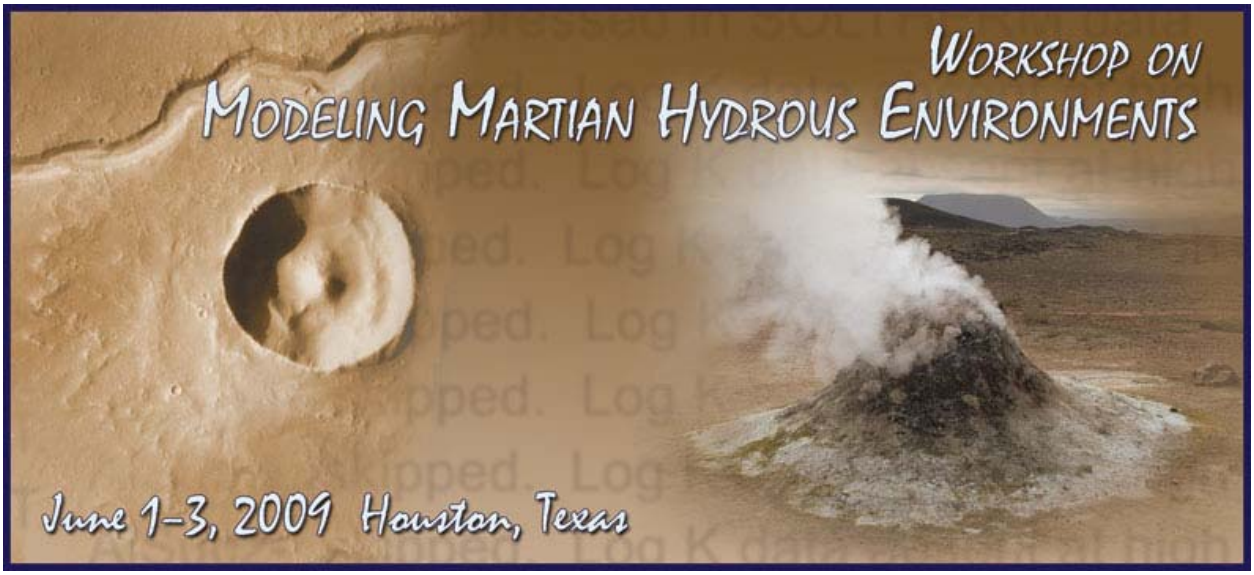

Program and Abstract Volume

LUNAR AND PLANETARY INSTITUTE

LPI Contribution No. 1482

WORKSHOP ON
MODELING MARTIAN HYDROUS ENVIRONMENTS

June 1–3, 2009 • Houston, Texas

Sponsors

Lunar and Planetary Institute
National Aeronautics and Space Administration

Scientific Organizing Committee

Susanne Schwenzer
Lunar and Planetary Institute

David Kring
Lunar and Planetary Institute

Stephen Clifford
Lunar and Planetary Institute

Scientific Organizing Committee

Oleg Abramov
University of Colorado

Jean-Pierre Bibring
Institut d'Astrophysique Spatiale

Allan Treiman
Lunar and Planetary Institute

David Vaniman
Los Alamos National Laboratory

Mikhail Zolotov
Arizona State University

Lunar and Planetary Institute 3600 Bay Area Boulevard Houston TX 77058-1113

LPI Contribution No. 1482

Compiled in 2009 by
LUNAR AND PLANETARY INSTITUTE

The Lunar and Planetary Institute is operated by the Universities Space Research Association under a cooperative agreement with the Science Mission Directorate of the National Aeronautics and Space Administration.

Abstracts in this volume may be cited as

Author A. B. (2009) Title of abstract. In *Workshop on Modeling Martian Hydrous Environments*, p. XX. LPI Contribution No. 1482, Lunar and Planetary Institute, Houston.

This volume is distributed by

ORDER DEPARTMENT
Lunar and Planetary Institute
3600 Bay Area Boulevard
Houston TX 77058-1113, USA
Phone: 281-486-2172
Fax: 281-486-2186
E-mail: order@lpi.usra.edu

A limited number of copies are available for the cost of shipping and handling.
Visit the LPI Online Store at https://www.lpi.usra.edu/store/products.cfm.

ISSN No. 0161-5297

Preface

This volume contains abstracts that have been accepted for presentation at the Workshop on Modeling Martian Hydrous Environments, June 1–3, 2009, Houston, Texas.

Administration and publications support for this meeting were provided by the staff of the Publications and Program Services Department at the Lunar and Planetary Institute.

Contents

Program

Monday, June 1, 2009
HYDROLOGY OF THE MARTIAN CRUST
8:45 a.m. Lecture Hall

8:45 a.m. Clifford S. M. * Lasue J. [INVITED]
The Role of Thermal Vapor Diffusion in the Subsurface Hydrologic and Mineralogic Evolution of the Martian Crust **[#4017]**

9:15 a.m. Lasue J. * Clifford S. M.
The Impact of Astronomically Induced Insolation Variations on the Extent of the Martian Cryosphere **[#4016]**

9:30 a.m. Harrison K. P. * Grimm R. E.
Regionally Compartmented Groundwater Flow on Mars **[#4012]**

9:45 a.m. Travis B. J. * Palguta J. Barnhart C. McGraw M. Feldman W. C.
MAGHNUM — A Numerical Simulator for Non-Isothermal Flow and Transport Processes in the Martian Regolith and Other Permeable Media **[#4022]**

10:00 a.m. BREAK

10:15 a.m. Möhlmann D. T. F. *
Liquid Interfacial and Melt-Water in the Upper Sub-Surface of Mars **[#4001]**

10:30 a.m. Rivera-Valentin E. G. * Chevrier V. F. Ulrich R.
Time Dependent Model for Heat Transfer and Water Vapor Diffusion/Adsorption at the Phoenix Landing Site **[#4020]**

10:45 a.m. Chevrier V. F. * Ulrich R. Altheide T. S.
Viscosity of Liquid Ferric Sulfate Solutions and Application to the Formation of Gullies on Mars **[#4011]**

11:00 a.m. Howe K. L. * Rivera-Valentin E. G. Chevrier V. F. Dixon J. C.
Experimental Simulation of the Effect of Viscous Fluids on Martian Gully Forms **[#4024]**

11:15 a.m. Wilkinson M. J. * Miller R. McG. Allen C. C. Kreslavsky M. H. Eckardt F.
Megafans as Hydrous Environments **[#4034]**

11:30 a.m. LUNCH

Monday, June 1, 2009
ON MARS I: ORBITERS, LANDERS, AND METEORITES
1:00 p.m. Lecture Hall

1:00 p.m. Mustard J. F. * Murchie S. L. Bibring J.-P. Bishop J. L. Ehlmann B. L. McKeown N. Milliken R. E. Poulet F. Roach L. E. [INVITED]
Hydrous Environments on Mars from Visible-Infrared Orbital Data **[#4033]**

1:30 p.m. Morris R. V. * Ming D. W. [INVITED]
Chemical and Mineralogical Constraints for Modeling Hydrous Environments on Mars from the Mars Exploration Rovers **[#4018]**

2:00 p.m. Ruff S. W. *
Gusev-Style Alteration: Unique or Ubiquitous on Mars? **[#4027]**

2:15 p.m. Treiman A. H. * [INVITED]
Martian Aqueous Alterations in ALH 84001 and the Nakhlite Meteorites **[#4031]**

2:45 p.m. BREAK

3:00 p.m. Rao M. N. * Nyquist L. E. Sutton S. R.
Fluid-Evaporation Records Preserved in Meridiani Rocks **[#4007]**

Monday, June 1, 2009
ON MARS II: INTERPRETING MARTIAN MINERALOGY
3:15 p.m. Lecture Hall

3:15 p.m. Berger G. * Toplis M. J. Treguier E. d'Uston C. Pinet P.
Evidence from Chemical Modeling for Small Amounts of Ephemeral Water During Alteration at Meridiani Planum, Mars **[#4003]**

3:30 p.m. Sutter B. * Ming D. W. Golden D. C.
The Duration of Chemical Weathering of Gusev Crater's Wishstone-Watchtower Sequence **[#4032]**

3:45 p.m. Hanley J. * Chevrier V. F. Altheide T. S.
Aqueous Perchlorate Liquid Solutions at the Phoenix Landing Site **[#4026]**

4:00 p.m. Sobron P. * Sobron F. Sansano A.
Hybrid Experimental/Theoretical Models for Acidic Sulfate Waters **[#4013]**

4:15 p.m. END OF SESSION

Monday, June 1, 2009
POSTER SESSION
5:00 p.m. Great Room

Lefort M. Maurette M.
A Meteoroid "Super-Volcanism" on the Earth and Mars in the Hadean Eon **[#4005]**

Lane M. D. Bishop J. L. Dyar M. D. King P. L. Hyde B. C.
Iron Sulfate and Sulfide Spectroscopy at Thermal Infrared Wavelengths **[#4009]**

Velbel M. A.
Corrosion Textures Formed by Aqueous Alterations of Mars Meteorite Olivine and Terrestial Analogs **[#4036]**

McGovern P. J. Morgan J. K.
Large-Scale Structural Manifestations of Phyllosilicate Generation and Deposition in Early Martian History **[#4037]**

Tuesday, June 2, 2009
ON MARS II: INTERPRETING MARTIAN MINERALOGY (continued)
8:30 a.m. Lecture Hall

8:30 a.m. Zolotov M. Yu. * [INVITED]
Aqueous Chemical Processes in Mars' History **[#4028]**

9:00 a.m. Vaniman D. T. * [INVITED]
Mineralogy in the Martian Hydrosphere — Data, Analogs and Experiments **[#4008]**

9:30 a.m. Chevrier V. F. *
Early Martian Surface Conditions from Thermodynamics of Phyllosilicates **[#4010]**

9:45 a.m. McAdam A. C. * Zolotov M. Yu. Mironenko M. V. Sharp T. G.
Effect of Temperature on Silica Formation During Acid-Basalt Alteration: Chemical Equilibrium Constraints **[#4025]**

10:00 a.m. BREAK

10:15 a.m. Reed M. H. * Palandri J. [INVITED]
Geochemical Models of Reactions of Seawater and Meteoric Water with Basalt and Peridotite **[#4019]**

Tuesday, June 2, 2009
THEMOCHEMICAL MODELING
10:15 a.m. Lecture Hall

10:30 a.m. Marion G. M. * [INVITED]
FREZCHEM: A Geochemical Model for Cold Aqueous Solutions **[#4006]**

11:00 a.m. OPEN DISCUSSION

12:00 p.m. LUNCH

Tuesday, June 2, 2009
COMPUTER PRESENTATIONS:
RUNNING CODES: HYDROLOGIC AND THERMOCHEMICAL CALCULATIONS IN REAL TIME!
1:30 p.m. Berkner Room

1:30 p.m. Travis B. J. *
MAGHNUM

2:30 p.m. Reed M. H. *
CHILLER

3:30 p.m. Marion G. M. *
FREZCHEM

4:30 p.m. END OF PRESENTATIONS

Wednesday, June 3, 2009
IMPACT CRATERS: HYDROLOGY, MINERALOGY, AND HYDROTHERMAL ACTIVITY
8:30 a.m. Lecture Hall

8:30 a.m. Kring D. A. * [INVITED]
Delivery and Redistribution of Volatiles on Mars During the Basin-forming Epoch: An Overview **[#4035]**

9:00 a.m. Maurette M. * Lefort M.
Formation and Impact "Maturation" of the Early Acrid Meteoroid Atmosphere of Mars **[#4004]**

9:15 a.m. Abramov O. * [INVITED]
Modeling Hydrothermal Activity Associated with Martian Impact Craters: An Overview **[#4029]**

9:45 a.m. Barnhart C. J. * Nimmo F. Travis B. J.
Geochemical and Geomorphological Effects of Post-Impact Hydrothermal Systems Incorporating Freezing **[#4023]**

10:00 a.m. BREAK

10:15 a.m. Newsom H. E. *
Constraints for Modeling Chemical Transport During Hydrothermal Alteration in Large and Small Impact Craters **[#4014]**

10:30 a.m. Schwenzer S. P. * Kring D. A.
Impact-generated Hydrothermal Systems in Mafic to Ultramafic Noachian Crust on Mars **[#4015]**

10:45 a.m. El Maarry M. R. * Markiewicz W. Mellon M. Goetz W.
Crater Floor Polygons: Desiccation Patterns of Crater Paleolakes? **[#4021]**

11:00 a.m. Altheide T. S. * Chevrier V. F. Rivera-Valentin E. G. Wray J. J.
Modeling the Stability of an Ancient Paleolake in Columbus Crater, Terra Sirenum, Mars **[#4030]**

11:15 a.m. CONCLUDING DISCUSSION

12:00 p.m. MEETING ADJOURNS

MODELING HYDROTHERMAL ACTIVITY ASSOCIATED WITH MARTIAN IMPACT CRATERS: AN OVERVIEW. O. Abramov, Department of Geological Sciences, University of Colorado, 2200 Colorado Ave., Boulder, CO 80309. (Oleg.Abramov@Colorado.edu)

Introduction: Impact events locally increase the temperature of a planetary crust, initiating hydrothermal activity if water or ice is present. Impact-induced hydrothermal activity is responsible for mineralogically and morphologically modifying many terrestrial craters [e.g., 1], and has been suggested for Martian craters [2, 3]. Present-day subsurface ice has been inferred at high latitudes (poleward of 60°) based on the detection of hydrogen by the Gamma Ray Spectrometer (GRS) onboard Mars Odyssey [4] (and confirmed by the Phoenix lander), and indirectly by the presence of fresh craters with fluidized ejecta blankets [e.g., 5] and rootless cones [6] at lower latitudes. Thus, a present-day impact may still generate hydrothermal activity.

Modeling history: The first modeling effort of impact-induced hydrothermal systems on Mars [2] focused on impact melt sheets and suggested that (i) hydrothermal circulation of steam in Martian melt sheets may have produced iron-rich alteration clays, ferric hydroxides, and near-surface accumulations of salts, (ii) the ability of vapor-dominated hydrothermal systems of concentrate sulfate relative to chloride is consistent with the high sulfate to chloride ratio found in the Martian soil by the Viking landers, and (iii) a major fraction of the Martian soil may consist of the erosion products of hydrothermally altered impact melt sheets. Further analytical modeling suggested that the formation of large impact craters on Mars (>65 km diameter) may have resulted in the creation of ice-covered impact crater lakes, which would not freeze for thousands of years, even under present climatic conditions [3].

The first numerical effort to model Martian impact-induced hydrothermal systems [7] used the finite-difference computer modeling code HYDROTHERM [8] to explore system mechanics, estimate lifetimes, and predict expected mineralogies. This work predicted cessation of any significant hydrothermal activity at a simple (~7 km) Martian crater in under 10,000 years. However, their simulations were limited to 50,000-100,000 years.

Abramov and Kring (2005) study: Building on the work by [7], hydrothermal activity was simulated for up to several million years, allowing estimates of system lifetimes for larger craters [9]. Crater lakes and the latent heat of fusion are were explicitly included in the model. The crater topography was improved based on observations of lunar craters, and was preserved throughout the simulation, rather than being removed shortly after crater formation. In addition, the post-impact temperature distributions that serve as starting conditions have been generated by hydrocode simulations either specifically for Mars [10] or were adapted for Mars with consideration of the different kinetic energy requirements for the formation of Martian craters.

While there are probably no active impact-induced hydrothermal systems today, they may have been prevalent at ~3.9 Ga, during an intense period of bombardment lasting 20 to 200 Ma [11, 12]. This cataclysm (also termed Late Heavy Bombardment) likely affected Mars, because meteorites from the asteroid belt, as well as the only sample of the ancient Martian crust (meteorite ALH 84001), show effects of impact-induced metamorphism at ~3.9 Ga [13, 14]. Thus, this study focused on an early Martian environment because it coincides with a sharply higher impact rate, and also because liquid water was likely stable in the subsurface and perhaps on the surface as well.

Hydrothermal activity in early Martian craters 30, 100, and 180 km in diameter was modeled using a modified version of a publicly available program HYDROTHERM [8], a three-dimensional finite difference code developed by the U.S. Geological Survey. Our modeling (e.g., Fig. 1) suggested the evolution of a post-impact hydrothermal system on early Mars proceeded as follows. The first step was the gravity-driven rapid draining of the rim and the flooding of the crater cavity by groundwater and any other available water source. The interaction between the incoming water and the hot interior of the crater may have produced large quantities of steam. Eventually, a crater lake should have formed in the basin of the crater, changing the flow of water from a gravity-driven to a hotspot-driven state. Our model simulations, plus observations at terrestrial impact sites [e.g., 1, 15], suggest that the most extensive hydrothermal alteration would have occurred in the central peak (for smaller craters) or the peak ring (for larger craters), and the modification zone where fluid flow is facilitated by faults. The region of active hydrothermal circulation extends laterally almost to the crater rim and to a depth of several kilometers. The habitable volume for thermophilic organisms (volume of rock that has water flow and a temperature between 50 and 100 °C) reaches a maximum of ~6000 km^3 in the 180 km crater.

The average lifetimes of impact-induced hydrothermal systems on early Mars are estimated at ~0.065 Ma for the 30-km crater, ~0.29 Ma for the 100-km crater, and ~0.38 Ma for the 180-km crater, and depend strongly on assumed ground permeability (Fig 2). The combination of relatively long lifetimes and long-lived upwellings suggest that impact-induced hydrothermal systems on early Mars would have resulted in a significant mineralogical alteration of the crust.

Follow-on studies: A study by Barnhart et al. [16] expanded the modeling of Martian impact-induced hydrothermal system to include freezing and an approximation of present-day atmospheric environment. This study found that convective systems subjected to surface temperatures below freezing force heat and fluid flow towards the center of the crater. This prolongs high temperatures, yields W/R ratios > 1000, and may explain mineral assemblages and fluvial features associated with central peaks of craters.

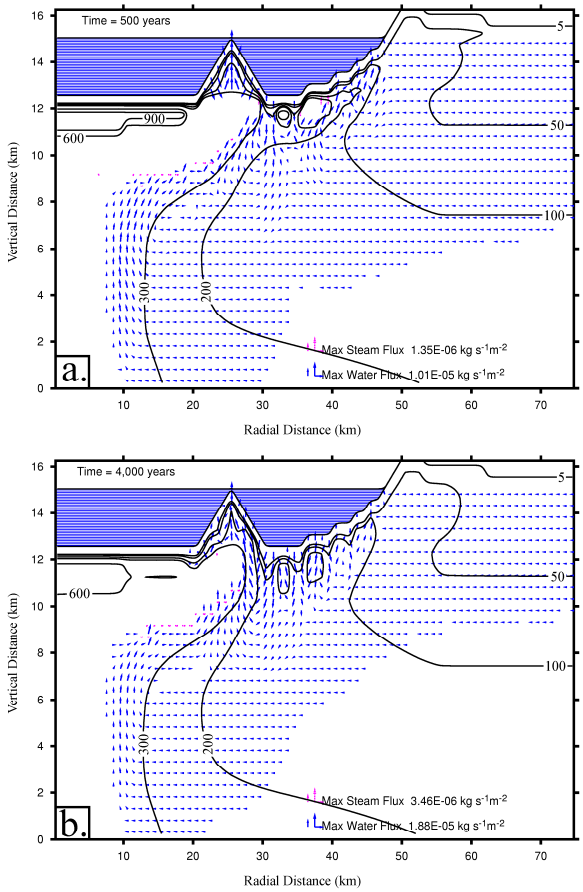

Figure 1. Results of a numerical simulation of the hydrothermal system at a 100-km impact crater on early Mars. Surface permeability is 10^{-2} darcies. Black lines are isotherms, labeled in degrees Celsius, and blue and red arrows represent water and steam flux vectors, respectively. The length of the arrows scales logarithmically with the flux magnitude, and the maximum value of the flux changes with each plot.

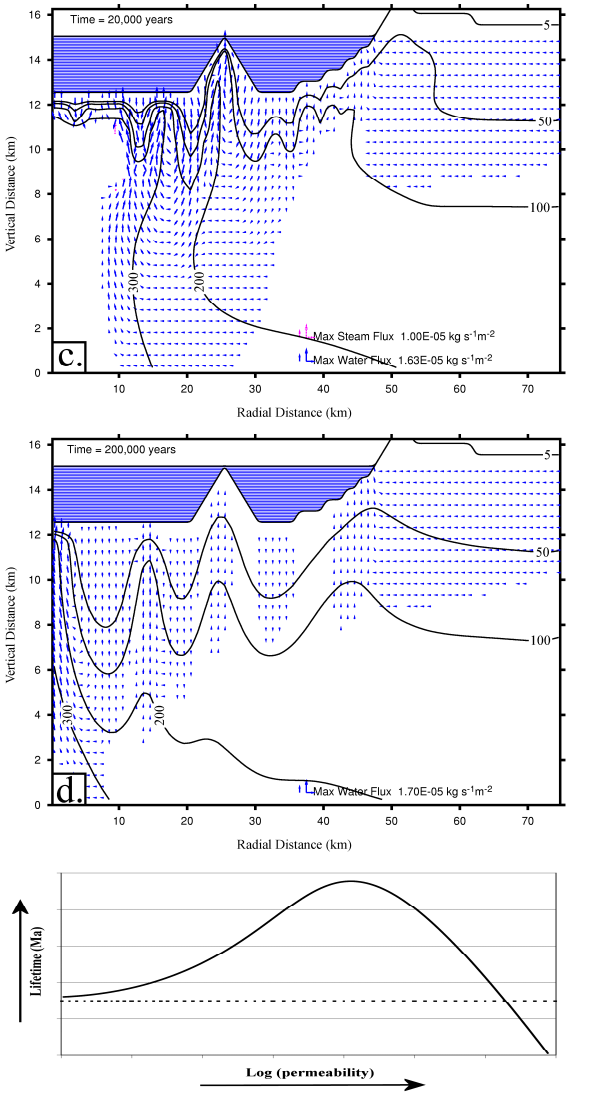

Figure 2. General dependence of system lifetime (defined by near-surface temperatures) on the average permeability of the subsurface. The dashed line indicates the lifetime in the absence of water.

References: [1] Naumov M.V. (2002) In: Plado J. & Pesonen L.J. (eds.) *Impacts in Precambrian Shields,* 117-171, Springer. [2] Newsom, H. E. (1980) *Icarus*, *44*, 207-216. [3] Newsom, H. E. et al. (1996) *JGR*, *101*, 14951-14956. [4] Boynton, W. V., et al. (2002), *Science* 297, 81 – 85. [5] Mouginis-Mark, P. J. (1987) *Icarus* 71, 268 – 286. [6] Lanagan, P. D., et al. (2001) *Geophys. Res. Lett*. 28, 2365 – 2368. [7] Rathbun J. A. and Squyres S. W. (2002) *Icarus 157*, 362-372. [8] Hayba, D. O. and Ingebritsen, S. E. (1994) *U.S. Geol. Surv. Water Resour. Invest. Rep*., *94-4045*, 85 pp. [9] Abramov O. and Kring D. A. (2005) *J. Geophys. Res.* 110, E12S09, doi:10.1029/2005JE002453. [10] Pierazzo E., et al. (2005*) Geol. Soc. Am. Spec. Paper 384*, 443-457. [11] Tera, F. et al. (1974) *Earth Planet. Sci. Lett.*, *22*, 1-21. [12] Ryder, G. (2000) *Eos Trans. AGU*, *81*(19), Spring Meet. Suppl., abstr. B22B-01. [13] Kring, D. A., and Cohen, B. A. (2002) *JGR*, *107*(E2), 4-1 to 4-6. [14] Bogard D. D. (1995) *Meteoritics, 30*, 244-268. [15] Osinski, G. R. et al. (2001) *Meteor. and Planet. Sci.*, *36*, 731-745. [16] Barnhart et al. (2009) *LPSC XXXX*, Abstract #2013.

MODELING THE STABILITY OF AN ANCIENT PALEOLAKE IN COLUMBUS CRATER, TERRA SIRENUM, MARS. T. S. Altheide[1], V. F. Chevrier[1], E. G. Rivera-Valentin[1], J. J. Wray[2]. [1]W. M. Keck Laboratory for Space Simulation, Arkansas Center for Space and Planetary Science, MUSE 202, University of Arkansas, Fayetteville, AR, 72701, talthei@uark.edu. [2]Department of Astronomy, Cornell University, Ithaca, NY 14853.

Introduction: Numerous fluid flow features [1-3] and abundant hydrous minerals [4-6] have been detected at the martian surface, including large deposits of sulfates, as well as those of chlorides [7, 8], minerals which have most likely evaporated from a liquid water source. Certain hydrous minerals also provide a mechanism for stabilizing liquid water under martian surface conditions by freezing point depression [9], making their presence on Mars significant for maintaing the water cycle.

Experimental studies have reported that salts can further stabilize liquid water by lowering the evaporation rate under simulated martian surface pressure and temperature [10], and have shown the evaporation of liquid water is dependent on the concentration of salt in solution [12], as well as, on the precipitation of hydrated mineral phases from solution [13]. The stability of brines on the surface of Mars has been additionally characterized through the mergering of kinectic behavior with thermodynamic processes, specifically, describing evaporation processes during phase changes in solution [13].

With the information provided by previous studies, we propose to more accurately describe the stability of a potential paleolake on Mars, as a function of martian temperature and humidity, with respect to evolving changes in solution concentration over time. This paleolake is located in an impact crater, which simplifies the geometry of the system.

Columbus Crater: The martian scenario used in the present study is Columbus crater (Fig. 1), located in Terra Sirenum, approximately 29.8°S, 166.1°W. It is roughly 100 km in diameter, with a depth of ~1.5 km, however, sedimentary materials have filled the crater over time so that the original depth may have been at least twice as much [14]. Various hydrated minerals have been identified in the crater rim and floor by the MRO-CRISM instrument. These minerals include: gypsum, Mg-sulfate, kaolinite, and possibily jarosite and ferrous sulfate [14]. Gypsum, Mg-sulfate, and kaolinite occur mainly in the crater rim, approximately 0.6 km above the crater floor. The deposits in the crater rim suggest a lower limit on the volume occupied by liquid water at ~ 5000 km^3. For this reason, we will use this value as our initial water resevoir, with the detected hydrated minerals as the components in the system.

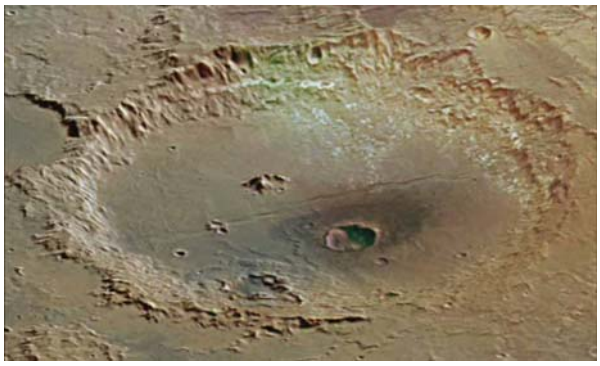

Figure 1. Perspective view of Columbus crater from the High Resolution Stereo Camera (HRSC) on Mars Express [14]. Two mosaic HRSC images are overlaying a digital elevation model. Light-toned hydrated mineral deposits are visible in the top portion of the crater rim [14].

Evaporation model: The evaporation of liquid water, pure or brine, is modeled using the modified semi-empirical Ingersoll equation [12, 13], which accounts for the buoyancy of water vapor in the heavier CO_2 atmosphere:

$$E = 0.17 D_{H_2O/CO_2} a_{H_2O} \frac{\rho_{sat} - \rho_{atm}}{\rho_{sol}} \left[\frac{\Delta\rho / \rho \, g}{\nu^2} \right]^{\frac{1}{3}} \qquad (1)$$

where E is the evaporation rate, ρ_{sat} is the saturation density of water vapor, ρ_{sat} the atmospheric density of water vapor, ρ_{sol} is the brine/solution density, $D_{H2O/CO2}$ is the interdiffusion coefficient of CO_2 and water vapor, a_{H2O} is the water activity in solutioin, $\Delta\rho/\rho$ is the relative density difference between the surface and the atmopshere v is the kinematic viscosity of CO_2 and g is the acceleration due to gravity (in m s^{-2}).

According to our previous studies and eq. (1), the determination of the evaporation rate requires the following parameters (Fig. 2): temperature, total pressure, humidity in the atmosphere, water activity and phases precipitating out of the liquid [12]. Therefore, several independent models, including the evaporation model, will be applied together.

Temperature Model: The evaporation rate is strongly dependent on the temperature of the brine/solution. We developed our own model to determine the evolution of the surface temperature with time [15]. An important hypothesis is that we will not consider variations of precipitating phases with temperature. Indeed, most geochemical models calculate precipitating phases with evaporation (like GWB) or

freezing like FREZCHEM [16], but not both simulataneously. In our case, we will consider that if the surface temperature drops under the freezing temperature of the solution, the lake is frozen. Our ultimate goal is the determine the minimual lifetime of the lake, which depends mostly on the evaporation.

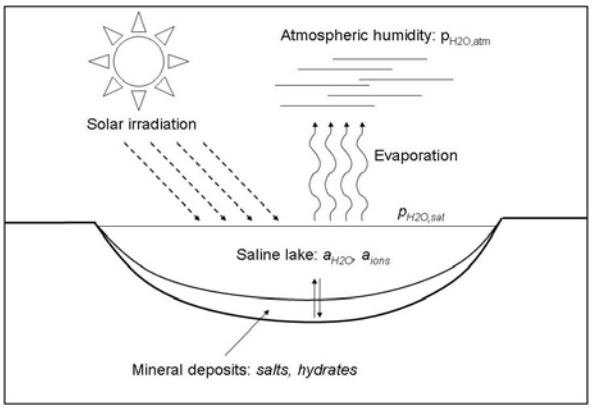

Figure 2. Conceptual model of the evaporation of a crater lake. Major controls on the evaporation rate are the insolation of the surface (temperature), atmospheric humidity, activity of water in solution (concentration of dissolved ions) and the nature of the precipitating phases.

Geochemical Modeling: We use the Gechemical Workbench software and the *thermo-phrqpiz* database, updated for ferric and ferrous components [17]. This model allows us to determine the phases precipitating once the solution reaches saturation (Fig. 3A) and also the activity of water in the liquid (Fig. 3B), which affects the evaporation rate [12, 13].

Humidity and pressure determination: Humidity directly affects the evaporation rate, and also the stability of the solution. Pressure mostly affects $\Delta\rho/\rho$ in eq. (1) and the diffusion coefficient, therefore, we will model humidity and pressure fluctuations using the GCM model [18].

Conclusions: We are modeling the stability of a potential paleolake using a combination of established models: GWB, for mineral precipitation and water activity, and our temperature and evaporation models, for determining longevity of liquid water in paleolake as a function of concentration, surface temperature, and humidity (using GCM), during periods of low and high obliquity. This work is an important step toward a more accurate understanding of water stability on the surface of Mars over time, which ultimately will address issues of geochemical evolution and potential habitability.

References: [1] Heldmann, J. L., *et al.*, (2007) *Icarus* 188, 324-344. [2] Mangold, N., *et al.*, (2003) *JGR* 108, #5027. [3] Mellon, M. T. and R. J. Phillips, (2001) *JGR* 106, 23165–23180. [4] Bibring, J. P., *et al.*, (2006) *Science* 312, 400-404. [5] Poulet, F., *et al.*, (2007) *JGR* 112,. [6] Squyres, S. W., *et al.*, (2004) *Science* 306, 1709-1714. [7] Gendrin, A., *et al.*, (2005) *Science* 307, 1587-1591. [8] Osterloo, M. M., *et al.*, (2008) *Science* 319, 1651-1654. [9] Brass, G. W., (1980) *Icarus* 42, 20-28. [10] Sears, D. W. G. and J. D. Chittenden, (2005) *GRL* 32,. [11] Chittenden, J. D., *et al.*, (2008) *Icarus* 196, 477-487. [12] Chevrier, V. and T. Altheide, (2008) *GRL* 35, L22101. [13] Altheide, T., *et al.*, (2009) *EPSL* in press,. [14] Wray, J. J., *et al.*, (2009) 40th Lunar and Planetary Institute Science Conference. [15] Ulrich, R., *et al.*, (2008) *Astrobiology* Submitted,. [16] Marion, G. M., *et al.*, (2008) *GCA* 72, 242-266. [17] Tosca, N. J., *et al.*, (2008) *JGR (Planets)* 113, 05005. [18] Forget, F., *et al.*, (1999) *JGR* 104, 24155-24176.

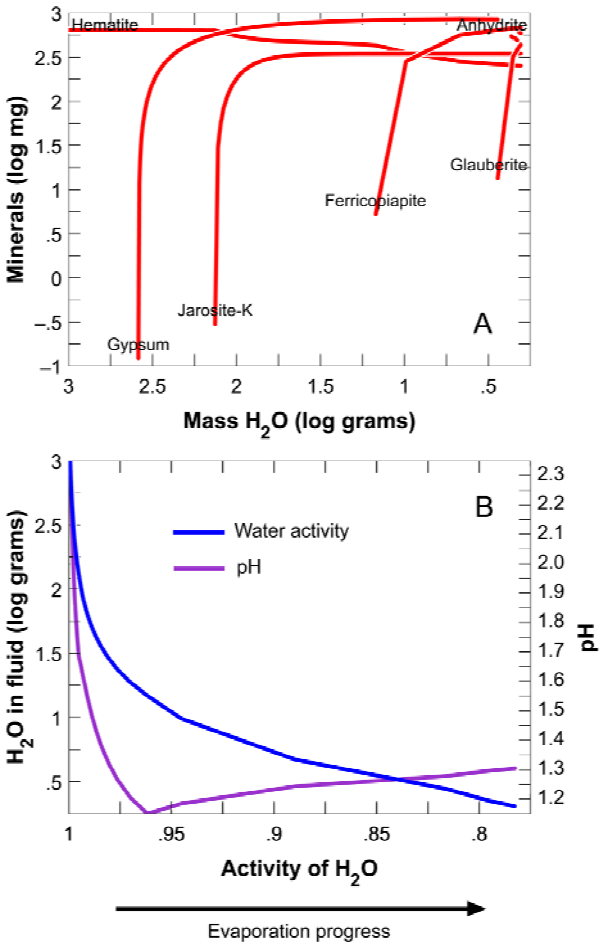

Figure 3. Results from the evaporation model of a sulfur-rich solution [12]. **(A)** Precipitated phases. We can compare these results to observations by CRISM and directly validate the model. **(B)** pH and water activity in solution. The water activity is used to calculate the evaporation rate at each step.

GEOCHEMICAL AND GEOMORPHOLOGICAL EFFECTS OF POST-IMPACT HYDROTHERMAL SYSTEMS INCORPORATING FREEZING. C. J. Barnhart[1], F. Nimmo[1], and B. J. Travis[2] [1]Dept. of Earth and Planetary Sciences, Univ. of California, Santa Cruz, 1156 High St. Santa Cruz, CA 95064 (barnhart@pmc.ucsc.edu), [2]Earth and Environmental Sci. Div., EES-2/MS-F665, LANL, Los Alamos, NM 87545

Summary: Post-impact hydrothermal (PIH) systems subjected to mars-like surface temperatures (-53 °C) and reasonable surface permeabilities (10^{-14} to 10^{-10} m^2) produce flow patterns with spatially diagnostic, surface-exposed water-to-rock (W/R) ratios of ~1 to 1000, channel-carving surface discharge rates of ~1 to 10 m^3/s and lake-forming total discharges of ~10^9 to 10^{12} m^3. A bolide 3.9 km in diameter traveling at 7 km/s generates a 45 km crater and delivers enough energy to heat subsurface water, and drive hydrothermal circulation (figure 1). This PIH circulation can lead to surface discharge of water, and chemical alteration – both are potentially detectable [1,2,3]. Our models differ from previous efforts [4,5,6,7,8] in that we incorporate freezing.

Model: We simulate the evolution of PIH systems using MAGHNUM (cf. [12]). MAGHNUM solves the time-dependent transport of water and heat through a porous medium. It incorporates phase transitions between ice, water and vapor. Given a particular crater size and associated heat sources, two principal dichotomies control PIH behavior: (1) frozen vs unfrozen surface and (2) conductive vs convective heat and fluid transfer.

Results: Discharge rates, total discharge and W/R ratios increase with permeability [13] (figures 2, 3 and 4). Systems with higher permeabilities (10^{-10} m^2) allow convection: rendering them capable of mining heat from the central uplift before the surface freezes. Convective systems subjected to surface temperatures below freezing are particularly interesting because an impermeable freezing front – the surface ice/water interface that marches from mid-floor to the central peak – forces flow towards the center of the crater. This effect prolongs modest near-surface temperatures (0 to 100 ° C for 50 kyr) and yields W/R ratios > 1000. For systems with lower permeability, the upper 200 m of rock at the crater's center experience fluid temperatures between 0 and 100 °C for 3500 yrs and W/R ratios of ~ 10. These results imply that different surface permeabilities should produce spatially diagnostic mineral alteration patterns (figure 3). This may explain mineral assemblages and fluvial features associated with central peaks of craters [3]. Discharge rates and total discharges are capable of producing gullies, ponds and lakes, but not alluvial fans (table 1).

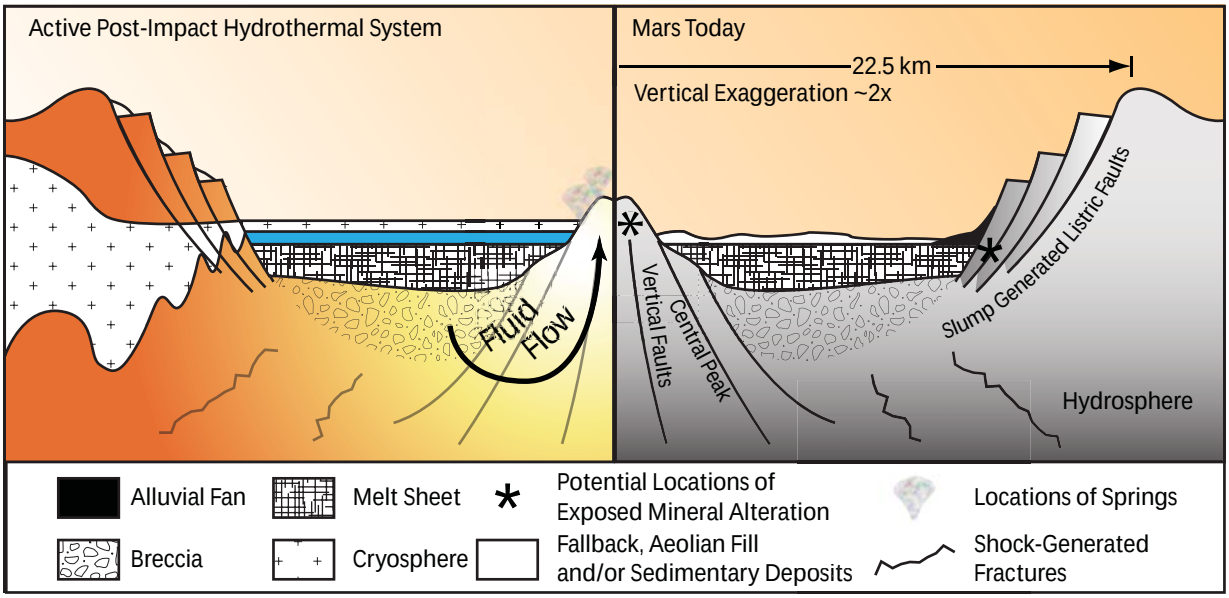

Figure 1: A schematic diagram of an active (left) and fossilized (right) PIH system (*motivated by* [4-11]). The energy delivered by a bolide and the redistribuiton of shock-heated material sets the stage for subsequent hydrothermal activity [*cf. 9,10,11*]. We model PIH systems exposed to clement (5 °C) and subfreezing (- 53 °C) atmospheres in effort to predict their observable effects. Simulations run for 330 kyrs in a 2D axisymmetric domain that spans 30 km radially and 10 km deep (dr = 333 m, dz = 200 m). We assume surface permeabilities of 10^{-10}, 10^{-12}, 10^{-14}, and 10^{-16} m^2 that, along with porosity, decay exponentially with depth. The initial temperature profile used in our simulations exhibits four notable characteristics: a radially decaying shock-heated region, a subsurface field at radius that remains frozen, hot material that is brought from depth as the crater collapses from transient to final form, and a background geothermal profile of 32.5 or 40 mW m^{-2}.

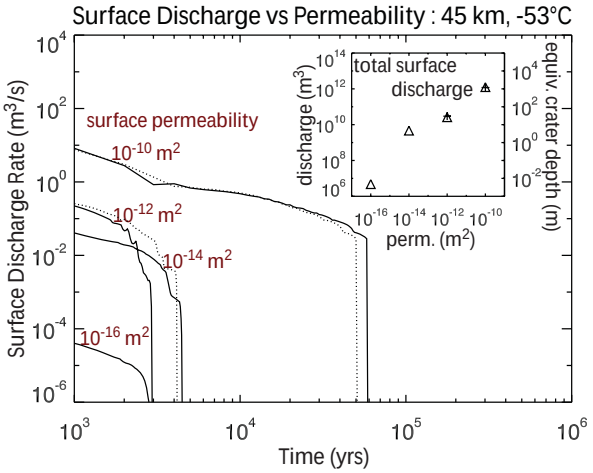

Figure 2: Discharge rate, total discharge, and system lifetime as a function of permeability for PIH systems exposed to a surface temperature of -53 °C. Solid lines and dotted lines indicate a background geothermal flux of 32.5 and 40 mW m^{-2} respectively. The inset shows the equivalent depth that the total discharge would fill a 45 km crater ignoring atmospheric loss. Convective systems (10^{-10} m^2) exhibit prolonged lifetimes and significant surface discharge. Conductive systems (10^{-12} and 10^{-14} m^2) experience a trade-off between system lifetime and discharge rate but produce similar total discharges.

PIH System →	Rate (m^3/s) 1 to 10	Time Active 10^3 to 10^5 yrs	Discharge (m^3) 10^9 to 10^{12}
Outflow Channels	10^4 to 10^9	Uncertain days to yrs	Uncertain 10^{15} to 10^{16}
Valley Networks	10^2 to 10^3	10^3-10^6 yrs episodically	Uncertain 10^{12} to 10^{14}
Alluvial Fans	10^3 to 10^5	< 10^2 yrs	10^{12} to 10^{14}
Gullies	~10 to 30	1-100 days	10^6

Table 1: Discharge rate, periods of activity, and total discharge for Martian fluvial morphologies. PIH system discharge rates are capable of producing gullies but are likely incapable of generating alluvial fans even if permeability structures favored their formation. In all cases a permenantly frozen region prevents discharge near the rim. PIH systems associated with 45 km diameter craters are incapable of supporting valley networks or larger fluvial morphologies. *Values Obtained from*: [15-22]

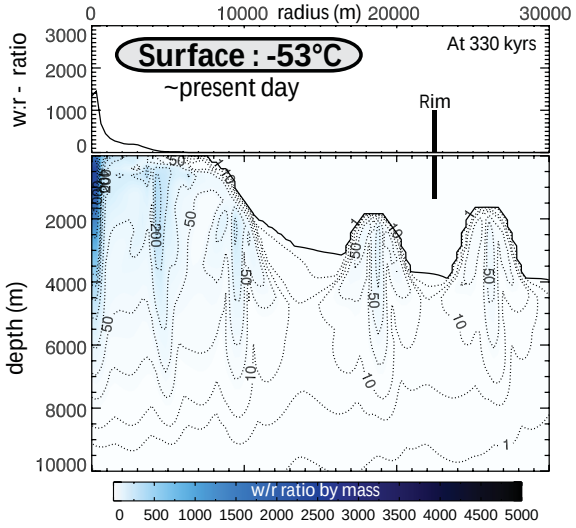

Figure 3: Surface (upper 200 m) W/R ratios as a function of radius for a PIH system with a surface permeability of 10^{-10} m^2 are enhanced at the central peak (top). At depth (contour plot), convective plumes are unable to reach the surface near the rim and do not produce surface discharge there.

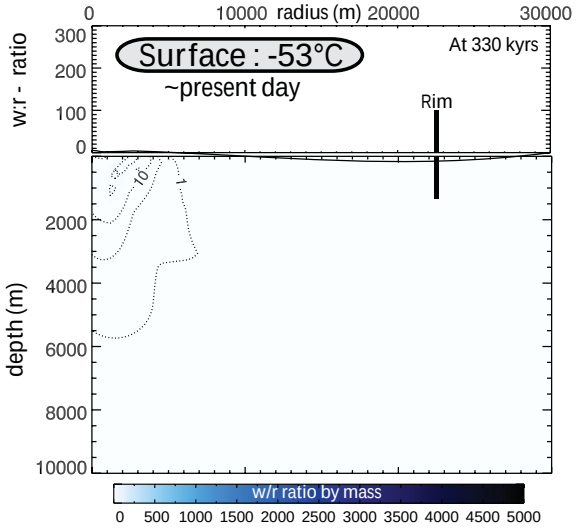

Figure 4: A PIH system with a surface permeability of 10^{-12} m^2 yields low W/R ratios. Low W/R ratios will produce phyllosilicates, chlorites, smectites, mica, amphibole and garnets [2,14]. These clays and minerals are detected in the central peak of a 45 km crater in Nili Fossae [23]. A PIH system with modest surface permeabilities exposed to a frozen atmosphere may have geochemically altered the rock and produced these minerals.

References: [1] Moore J.M. and Howard A.D. (2005) *JGR* 110, E04005. [2] Schwenzer S.P. and Kring D.A. (2008) *LPSC* XXXIX, 1817. [3] Elhman B.L. et al. (2008) *Nat. Geosci.* 1, 355. [4] Newsom H. E. (1980) *Meteoritics*, 15: 339. [5] Newsom H. E. et al. (1996) *JGR*, 101: 14951-14956. [6] Rathbun J. A. and Squyres, S. W. (2002), *Icarus*, 157: 362-372. [7] Abramov O. and Kring, D.A. (2005), *JGR* 110, E9:12. [8] Barnhart C.J. et al., (2008) *LPSC* XXXIX, 2294. [9] Melosh, H.J. (1989), New York, *Oxford Univ. Press*. [10] Davies, G.F. and Arvidson, R.E. (1981) *Icarus*, 45: 339- 346. [11] Shubert, G. and Solomon, S.C. (1992) Mars, *Univ. of Arizona Press*: 147-183. [12] Travis B.J. et al. (2003) *JGR*, 108, E4. [13] Barnhart C.J. et al., (2009) LPSC XXXX, #2013. [14] Schwenzer, S. P. and Kring, D. A., (2009) LPSC XXXX, #1421. [15] Williams, R. M., et al., (2000) *GRL* 27: 1073. [16] Tanaka, K. L. and Chapman, M. G., (1990) *JGR* 95: 14315-14323. [17] Baker, V. R. et al., (1992) Mars, *Univ. of Arizona Press*. [18] Carr, M. H., (1987) *Nature* 326: 30-35. [19] Irwin, R. P., et al., (2005) *JGR* 110 E9. [20] Barnhart, C. J. et al., (2009) *JGR* 114 E13. doi:10.1029/2008JE003122. [21] Kraal, E., et al., (2008) *Nature* 451, 21 doi:10.1038/nature06615. [22] Parsons, R. A. and Nimmo, F. (2009) LPSC XXXX, #1947. [23] Elhmann, B.L., *(submitted to JGR CRISM special issue)*

EVIDENCE FROM CHEMICAL MODELING FOR SMALL AMOUNTS OF EPHEMERAL WATER DURING ALTERATION AT MERIDIANI PLANUM, MARS. G. Berger[1], M. J. Toplis[2], E. Treguier[3,4], C. d'Uston[3], P. Pinet[2], [1]LMTG, [2]DTP, [3]CESR, Observatoire Midi-Pyrénées, 14 av. E. Belin, 31400 Toulouse, France, [4]ESAC, 28691 Villanueva de la Cañada, Spain.

Introduction: Thanks to the instruments onboard recent ground-based and orbital missions, an unprecedented amount of high quality data exists relevant to the secondary minerals characteristics of the altered martian surface. One of the most striking results is that sulfates are among the most abundant secondary phases and are concentrated in geological units intermediate in age between older Noachian terrains where clays are observed and younger Amazonian terrains dominated by the presence of nanophase iron oxides [1]. These observations are of interest as they are relevant to important questions, such as the abundance and lifetime of liquid water over geological time.

In this respect the sulfate-rich bedrocks analyzed by the rover *Opportunity* in Eagle and Endurance craters at Meridiani Planum provide important constraints on the physical and thermodynamic conditions at the time of sulfate deposition. Among the different interpretations proposed in literature [2-4], the models involving *in-situ* alteration of basaltic sands have the advantage that they alleviate the need for large unidentified external sources of altered grains and/or brines. With these issues in mind we have used a geochemical simulator (JChess) to model basalt alteration as a function of time, with the aim of identifying self-consistent scenarios for rock-formation at Meridiani.

Model parameters: The initial silicate material modeled is unaltered olivine-rich Martian basalt Adirondack from Gusev crater, described in [5]. The initial fluid phase is assumed to be pure H_2O at 0°C, produced by melting of near-surface ground ice. One of the originalities of our model is that the source of sulfur, as well as the driving force of alteration, is assumed to be gaseous SO_3, the most soluble and most acidic of the potential sour gases assumed to be derived from oxidation volcanic SO_2, the aqueous phase simply acting as a medium allowing the chemical reactions to proceed. Dissolution of SO_3 into water at 0°C is considered to be instantaneous, and simulations were performed assuming partial pressures for O_2 and CO_2 close to values observed in the current Martian atmosphere. For kinetic reasons the precipitation of quartz (replaced by chalcedony), hematite (replaced by goethite) and secondary mafic minerals is suppressed in the calculations.

Previous calculations [6] assuming congruent dissolution and corresponding to an embedded dune situation (W/R=6), showed that at low SO_3/basalt the solution is neutralized by hydrolysis of the rock to produce a secondary assemblage dominated by clays and carbonates, while at the highest modeled SO_3/basalt (~1), alteration produces amorphous silica and sulfates (jarosite and gypsum). However, reproduction of the mineralogy observed at Meridiani required the addition of a large amount of SO_3, largely in excess of that measured by the rover *Opportunity*. To assess the effect of kinetic, additional simulations as a function of time are presented here, using specific dissolution kinetics for each rock-forming mineral. Dissolution rates were calculated for initial grains 1 millimeter in diameter, using dissolution constants derived from laboratory data at low pH [7] and taking into account variations of pH and deviation from equilibrium. Assuming closed system alteration, the bulk-rock sulfur content of Meridiani samples provides a direct estimate of the SO_3/basalt ratio of to be used (~0.25).

Results: Based upon a series of simulations with W/R from 0.5 to 100, we tested whether it is possible to explain the compositional variations previously highlighted [3] by a variation in local proportions of altered solids and dry salts from the coexisting brine (coming from the in-situ evaporation of the final brine). We find that the Meridiani trend lies along such a mixing line only (Fig. 1A) at W/R≤1 and for short reaction times (around 2 years at W/R=0.5). However, the calculated mineralogy (Fig. 1B), suggests that significant quantities of unreacted olivine remain, in contrast to spectroscopic observations [8].

Finally, we explored higher values of SO_3/basalt. Best fit with mineralogical data (SO_3/basalt > 0.25) necessarily implies loss of at least part of the brine component at the end of reaction. As an example (not showed), at W/R = 1, SO_3/basalt = 0.48 (the maximum value compatible with Meridiani data) and alteration times in the range 12 to 20 years, the compositions of the altered solids fall very close to Meridiani bulk-rock data with little or no contribution of the brine component being necessary: olivine has been eliminated, but significant primary pyroxenes and plagioclase remain, secondary mineralogy is dominated by sulfates (jarosite, gypsum, and epsomite), iron oxide, and amorphous silica, all these mineralogical characteristics being consistent with mini-TES and Mössbauer measurements of the rocks at Meridiani Planum [9].

Conclusion: We conclude that the best working hypothesis to explain the petrogenesis of rocks ana-

lyzed by Opportunity is that they are dominated by the solid residues of *in-situ* alteration of basalt, a significant fraction of the coexisting brines having been transported elsewhere before evaporation.

Furthermore, we highlight the fact that these kinetic calculations predict that continued hydrolysis acts to neutralize the aqueous solution, destabilizing jarosite and stabilizing phyllosilicates. Thus, the close correspondence between modeled and observed mineralogy is limited in time (in this case <~20 years), consistent with an emerging picture of conditions at Martian surface during the last 3.5Ga [10-12].

References:

[1] Bibring J.-P. *et al.* (2006) *Science* **312**, 400-404. [2] McLennan S.M. *et al.* (2005) *E.P.S.L.* **240**, 95-121. [3] Squyres S.W. *et al.* (2006) *Nature* **443**, doi:10.1038/nature05212. [4] McCollom T.M. and Hynek B.M. (2005) *Nature* **438**, 1129-1131. [5] McSween H.Y. *et al.* (2006) *JGR* **111**, E02S10. [6] Treguier E. *et al.* (2008) *J.G.R.* **113**, E12S34. [7] Zolotov M.Y. and Mironenko (2007) *J.G.R.* **112,** E07006. [8] Glotch T.D. *et al.* (2006) *J.G.R.* **111**, E12S03. [9] Squyres S.W. et al. (2006), JGR, 111, E12S12. [10] Hurowitz J.A. and McLennan S.M. (2007) *EPSL* **260**, 432-443. [11] Chevrier V. and Mathé P.E. (2007) *Planet. Space Sci.* **55**, 289-314. [12] Niles P.B. and Michalski J. (2009) *40th LPSC*, # 1972.

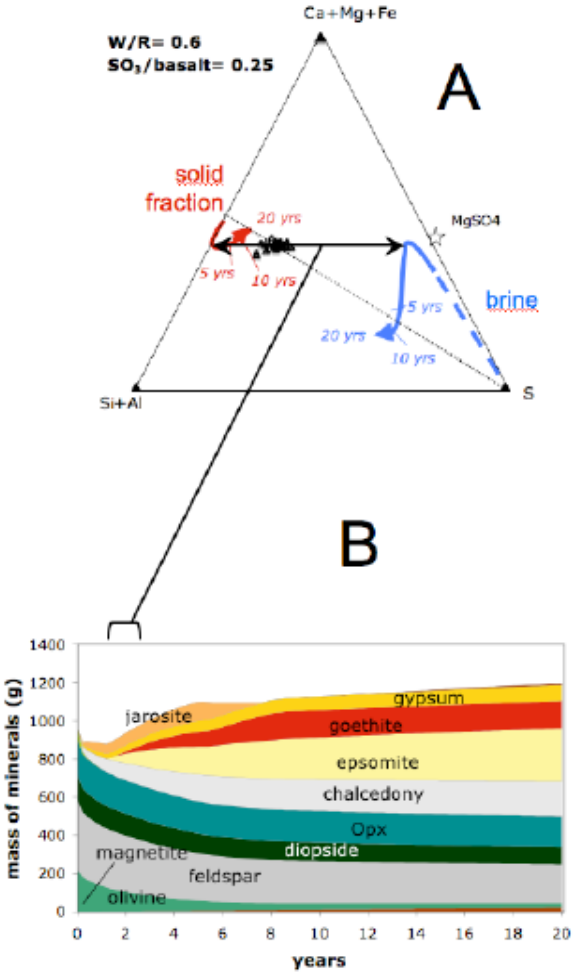

Figure 1: Kinetic model of alteration with SO_3/basalt = 0.25 and W/R = 0.6. Panel A represents chemical compositions in the ternary diagram. The red line is the trend of the solid fraction, the blue line of the coexisting brine. Panel B represents the mineralogy of the solid fraction.

EARLY MARTIAN SURFACE CONDITIONS FROM THERMODYNAMICS OF PHYLLOSILICATES.

V.F. Chevrier[1], [1]W.M. Keck Laboratory for Space Simulations, Arkansas Center for Space and Planetary Sciences, 202 Old Museum Building, University of Arkansas, Fayetteville, AR 72701, USA. vchevrie@uark.edu.

Introduction: The Mars Express OMEGA and Mars Reconnaissance Orbiter CRISM imaging spectrometers have identified phyllosilicates (Fe, Mg, Ca-smectites, kaolinite and chlorite) in Noachian aged terrains [1-3], often associated with lacustrine or fluvial deposits [4,5]. Carbonates have also been recently identified in similar areas [6]. Clay minerals usually result from long term weathering of primary minerals by liquid water at neutral to alkaline pH [7]. Their presence and association with carbonates [6] suggests an early environment completely different from the acidic conditions responsible for the formation of sulfate outcrops widely observed on Mars [8].

Starting from the hypothesis that phyllosilicates are formed by liquid water induced weathering of the primary basaltic outcrops, thermodynamic models are used to study the conditions on the surface during the Noachian. Focus was placed on the effect of CO_2 partial pressure and solution temperature on the precipitating parageneses.

Methods: The water composition data presented in Table 1 was used as input of the models. This composition reflects possible primary solutions on Mars [9]. Al^{3+} and SiO_2 have been set up at typical terrestrial values, being generally driven by their low solubility. The Geochemical Workbench software package was used to model thermodynamic equilibria, with the *thermo.com.v8.r6+* database, which contains about 350 common silicates. This database uses Debye–Huckel theory for ionic activities, which is perfectly accurate to describe behavior of solutions at relatively to very low concentrations.

Table 1. Concentrations and activities of dissolved species from [9] except for Al^{3+} which is estimated in this work.

Specie	Log (Activity, 10^{-3} mol l^{-1})	Concentration (mg L^{-1})
SiO_2	-4.5	60.1
Al^{3+}	-5	0.3
$Fe^{2+/3+}$	-3.1	44.7
Mg^{2+}	-3.0	24.3
Ca^{2+}	-3.3	20
K^{+}	-4.2	2.7
Na+	-3.1	18.4
SO_4^{2-}	-3.7	17.3
Cl^{-}	-3.2	23

Evaporation simulations: In all simulations, the evaporation paragenesis is largely dominated by ferric phases. The early paragenesis (high water content) includes mostly nontronite, magnetite and chalcedony (Fig. 1). Nontonite and magnetite precipitate from the very beginning of the simulation, indicating that the early solution is largely supersaturated at neutral pH and high pe. Indeed, dividing the concentrations in Table 1 by 100 still shows supersaturation in nontronite and magnetite.

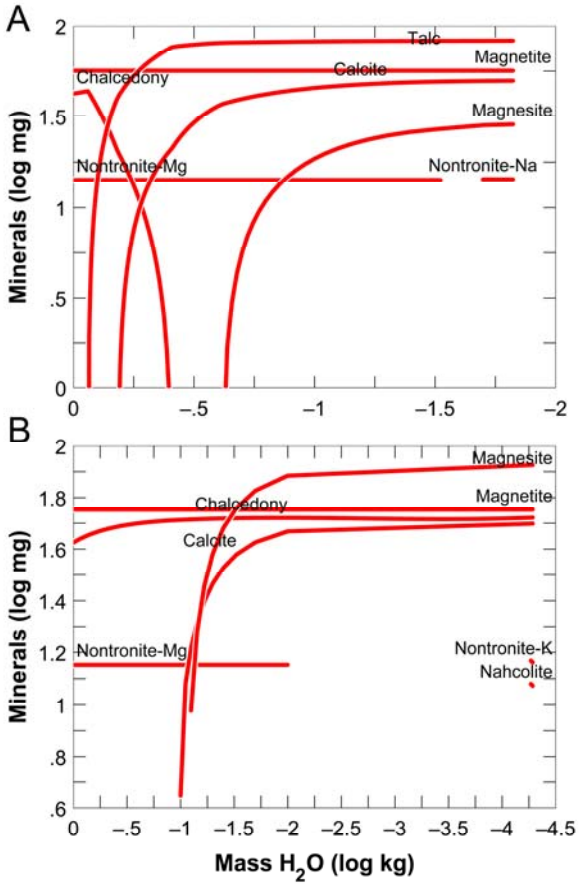

Figure 1. Simulations of solution evaporation at 25ºC using initial compositions presented in Table 1, with pe = 13 (high oxidation level). **(A)** p_{CO2} = 0.006 bar, pH = 7. **(B)** p_{CO2} = 1 bar, pH = 7.

At higher concentration levels, and in low p_{CO2} (6 mbar), talc and calcite precipitate in addition to nontronite, chalcedony and magnetite (Fig. 1A). Interestingly calcite has been suggested to be present at the Phoenix landing site, along with a phyllosilicate phase [10], and thus could result from present-day alteration in the CO_2-rich, but low-pressure atmosphere. Magnesite, recently observed ion Nili Fossae [6], is the last phase to precipitate, in minor amounts, because of the low CO_2 pressure.

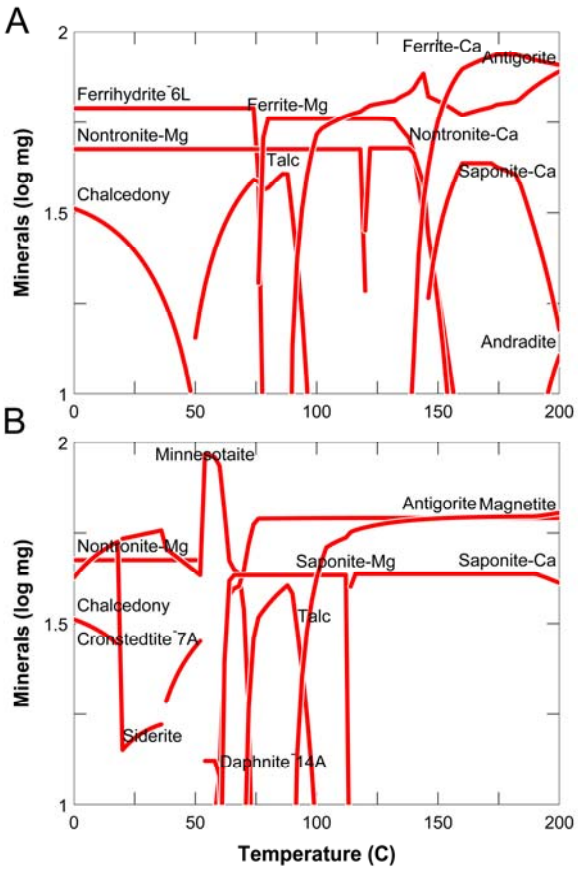

Figure 2. Evolution of the secondary paragenesis as a function of the temperature of the system. **(A)** Oxidant conditions pH = 7 and pe = 13. **(B)** Reducing conditions with pH = 7 but pe = 0. Nontronite is much more stable at high pe, but the conditions need to be reducing for chlorite to precipitate.

At higher CO_2 pressure (1 bar), carbonates become logically predominant (Fig. 1B) leading to early precipitation of magnesite, which becomes a major phase, at the expense of talc.

Temperature effect: Three different thermal scenarios were tested. The first one has oxidizing conditions (pe=13.05) which can simulate the effect of increasing temperature on the surface, for example by volcanic activity. In this case, nontronite appears remarkably stable, destabilizing only at temperature above 150ºC (Fig. 2A), being replaced by talc, saponite and spinel.

In reducing conditions (pe=-5), corresponding to typical terrestrial hydrothermal systems, the mineralogical paragenesis appears very complex, with several assemblages of Fe^{2+} and Fe^{3+} phyllosilicates evolving with the temperature (Fig. 2B). Globally, nontronite is stable only up to ~50ºC, at which it is replaced by saponite. We also observe the presence of Fe^{2+} phyllosilicates (minnesotaite). In both scenarios, at higher temperature the formation of serpentine (talc and antigorite) and chlorite (Daphnite) phases occurs.

The third simulation combined high temperature and high p_{CO2} (Fig. 3). In this case, the carbonate was not magnesite but siderite ($FeCO_3$). Moreover, kaolinite replaced nontronite as the low-T phyllosilicate. Except these two differences, the overall paragenesis remains relatively similar to the other thermal simulations.

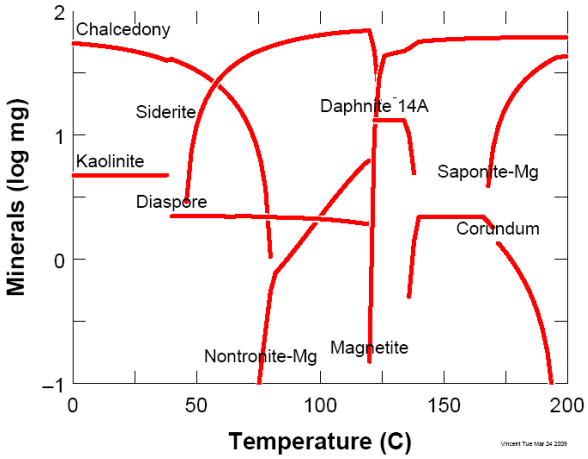

Figure 3. Secondary paragenesis as a function of the temperature in reducing conditions (pe=0) and for a p_{CO2} = 1 bar.

Conclusions: These simulations confirm that the Noachian parageneses are controlled by the CO_2 partial pressure and temperature, rather than pH or water abundance [7]. The observation of serpentine in Nili Fossae [11] indicates hydrothermal alteration of olivine, although magnesite shows rather evaporation. Conditions probably evolved from early hydrothermalism at the end of the emplacement of the olivine bedrock, to surface weathering and evaporation in a transient CO_2-rich atmosphere. Hydrothermalism could not have happened during the high-p_{CO2} era or siderite would have formed instead of magnesite. The high abundance of smectites compared to carbonates suggest however that the overall Mars atmosphere remained relatively poor in CO_2.

References: [1] Poulet F. et al. (2005) *Nature* 481, 623-627. [2] Mustard J. F. et al. (2008) *Nature* 454, 305-309. [3] Bishop J. L. et al. (2008) *Science* 321, 830-833. [4] Ehlmann B. L. et al. (2008) *Nature Geosci.* 1, 355-358. [5] Grant J. A. et al. (2008) *Geology* 36, 195-198. [6] Ehlmann B. L. et al. (2009) *Science* 322, 1828-1832. [7] Chevrier V. et al. (2007) *Nature* 448, 60-63. [8] Bibring J. P. et al. (2006) *Science* 312, 400-404. [9] Catling D. C. (1999) *J. Geophys. Res.* 104, 16453-16469. [10] Boynton W. V. et al. (2008) *AGU fall meeting, December 15-19, 2008, San Francisco, USA.* [11] Ehlmann B. L. et al. (2009) *LPSC* XL, #1787.

VISCOSITY OF LIQUID FERRIC SULFATE SOLUTIONS AND APPLICATION TO THE FORMATION OF GULLIES ON MARS. V.F. Chevrier[1], R. Ulrich[1,2], T.S. Altheide[1], [1]Arkansas Center for Space and Planetary Science, [2]Department of Chemical Engineering, University of Arkansas, Fayetteville, AR 72701, USA; vchevrie@uark.edu.

Introduction: Almost all flow models for martian gullies to date have assumed liquids that exhibit viscosities on the order of 1 cP (10^{-3} Pa.s) such as pure water [1,2] and liquid carbon dioxide [3]. Alternatively, salt solutions have been suggested based on thermodynamic and kinetic arguments as a way to stabilize liquid water in present day martian conditions [4,5].

We have recently proposed that concentrated aqueous solutions of ferric sulfate $Fe_2(SO_4)_3$ might be a liquid under martian conditions because it has amongst the lowest eutectic temperature (205 K) of common ionic materials [6]. This paper reports on experimental measurements of the visocity of ferric sulfate solutions as a function of temperature and concentration [7]. We then use this information in a numerical flow model of a standard gully as a bridge between the composition and temperature of the brine and the fluid dynamics, to identify geomorphological characteristics that might be observed on Mars [8,9]. Specifically, in this study we estimate the flow velocity and the drag forces on boulders within the gullies for these highly viscous fluids.

Methods: Viscosity of various concentrations of $Fe_2(SO_4)_3$ brines was measured using EZ/Zahn (ASTM) Dip Viscosity Cups (#1 – 5). These cups were filled with ferric sulfate brines and the time for the solution to drain through a calibrated hole in the bottom was measured. Empirical equations produced by the manufacturer were used to determine the viscosity from the drain time.

Results: The viscosity of ionic solutions increases with higher concentrations and lower temperatures (Fig. 1). Values range from 7.0 10^{-3} Pa.s for 38.8 wt% at 285 K to 4.6 Pa.s for 58.2 wt% at 260 K. The total error on the final dynamic viscosity was estimated to be approximately 10%.

To determine the dependency of viscosity on concentration and temperature, we used an extended version of the usual Arrhenius-type law. Fitting the dependency of our data, we obtain the following semi-empirical equation:

$$\mu = \exp\left[aC^b\right]\exp\left[\frac{\Delta E}{R}\left(\frac{1}{273.15}-\frac{1}{T}\right)\right] \qquad (1)$$

where μ is the viscosity in Pa.s, C the concentration in kg kg^{-1}, T the temperature of the fluid in K, ΔE the activation energy in J, R the ideal gas constant (8.314), and a and b are empirical constants (Fig. 1B). This equation is used to model the behaviour of fluids under martian conditions (Fig. 1).

Modeling: The gully modeled is V-shaped with a 60° bottom angle, a 15° slope, and an average roughness of 0.1 m (Fig. 2A,B). The independent variables are kinematic viscosity (10^{-6} to 10^{-2} m^2/s, corresponding to water densities of 1 to 10,000 cP) and depth of liquid in the gully (1 to 5 m). Gravity is 3.73 m/s^2 and the flow is uniform and steady.

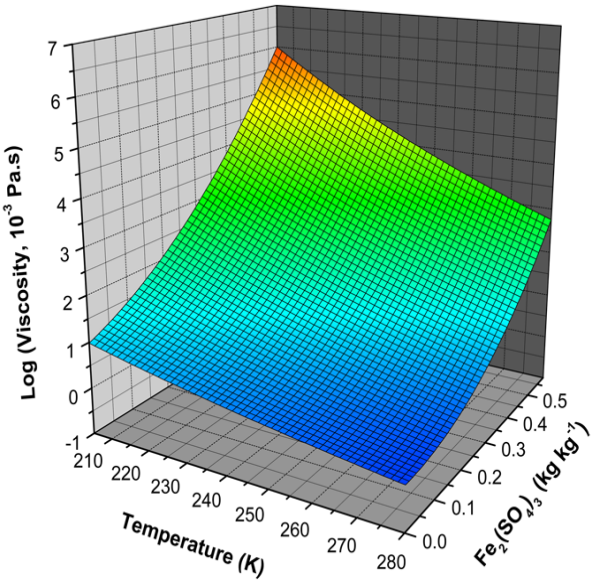

Figure 1. 3D view of viscosity data of $Fe_2(SO_4)_3$ as a function of concentration and temperature, calculated using eq. (1). This equation was determined from experimental data. Ferric sulfate solutions exhibit viscosities up to 6 orders of magnitude higher than pure water at 273 K.

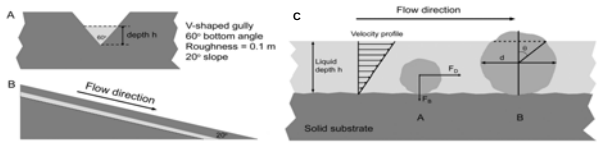

Figure 2. Schemes of the gully model used in this study. **A**. Front view. **B**. Side view. **C**. Boulder displacement with the two cases where the boulder is below or above the surface of the liquid.

We used a general Bernoulli energy balance relating potential energy supplied by the 15° slope to energy dissipated by friction against the wetted perimeter. Three regimes are observed: at low temperature, laminar flow dominates, and the velocity is strongly dependent on the viscosity, at higher temperature, turbulent flow is observed, with constant velocity around 8.5 m s^{-1} (Fig. 3). The transition regime shows a strong

increase of velocity, up to 14 m s^{-1}. In regions of turbulence, at high T and low viscosity, the flowrate is a very weak function of viscosity. Indeed, at high Reynolds number, above 10^5, faster flow only amplifies the random eddy motion without changing its scale.

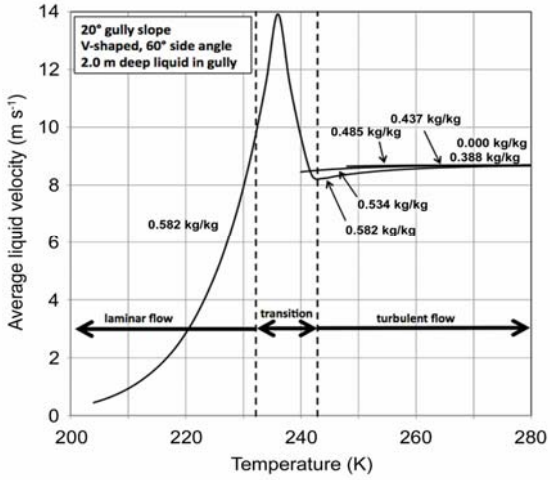

Figure 3. Results of numerical modeling of flow velocity as a function of temperature and concentration in the typical gully described by our model.

Drag Forces on Boulders: Viscous flows tend to remove smaller-sized rocks because of their high surface area to volume ratio. Drag force depends on surface area and weight on volume. Our flow model is used to estimate the force that these flows would impart on a boulder. To a first order, if neglecting the friction forces between the boulder and the gully floor, the limit of boulder displacement may be defined as the equilibrium between the weight force F_B and the drag force F_D (if $F_D > F_B$, then the boulder moves). This amounts to a rolling resistance, F_B/F_D, of one. The two forces are:

$$F_B = \left(\frac{\pi}{6}d^3\right)\left(\rho_b - \rho_f\right)g \text{ and } F_D = \frac{1}{2}\rho_f C_D\left(\frac{\pi}{4}d^2\right)V^2$$

The boulder density (ρ_b) is 3000 kg m^{-3}. The dependency of the solution density (ρ_f) with concentration was empirically determined from experimental measurements as correlated with the ARrhenius-type equation. The drag coefficient (C_D) is a function of the boulder's Reynolds number. Then the two forces are set equal and numerically solved for the diameter d.

Results show that most of the flow occurs in turbulent conditions (green), where the boulder limit size is constant at 3 m (Fig. 3). The transition zone appears at low temperature and high concentrations (around 230 K and 0.45-0.5 kg kg^{-1}) in red, where high velocities move boulders up to 4 m (Fig. 3). The laminar regime occurs only at very low temperatures, close to the eutectic (red to green to blue), and is characterized by overall much lower boulder sizes (down to ~0.5 m).

Conclusions: MRO-HiRISE observations have shown that boulders with sizes ranging from 0.5 to 3 m are more abundant in gullies than in the surrounding terrains [10], suggesting that smaller size objects have been removed. The results of our model are consistent with this observation, since our size limit is 3 m for the greatest part of the flow space in the turbulent regime. The fact that abundant boulders of lower size are found in gullies suggest that low-velocity laminar flows are also occurring, which is once again supported by other observations [9]. Ferric sulfate solutions provide an excellent analogue for brines and visous fluids in general, due to the large range of viscosities covered. Yet, the very reduced field of temperature and concentration to reach very high viscosities suggests that the liquid phase probably contain a large amount of debris.

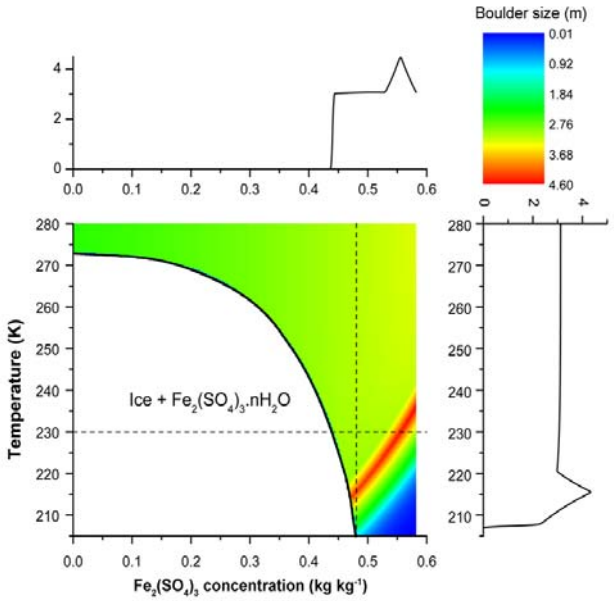

Figure 4. Results of numerical model determining the boulder size threshold for flow-induced displacement. The legend for the colour map is in the top right corner. In the white area, ferric sulfate brine is frozen. The thick black line is the liquidus line: from 273.15 K for pure water (C = 0) to ~205 K for saturated ferric sulfate solution (C = 0.48 kg kg^{-1}).

References: [1] Costard F. et al. (2002) *Science* 295, 110–113. [2] Heldmann J. L., M. T. Mellon (2004) *Icarus* 168, 285-304. [3] Musselwhite D. S. et al. (2001) *Geophys. Res. Lett.* 28, 1283-1285. [4] Brass G. W. (1980) *Icarus* 42, 20-28. [5] Sears D. W. G., J. D. Chittenden (2005) *Geophys. Res. Lett.* 32. [6] Chevrier V., T. S. Altheide (2008) *Geophys. Res. Lett.* 35. [7] Chevrier V. et al. (2009) *J. Geophys. Res.* In press. [8] Coleman K. A. et al. (2008) *Planet. Space Sci.* In press. [9] Mangold N. et al. (2003) *J. Geophys. Res.* 108, #5027. [10] McEwen A. S. et al. (2007) *Science* 317, 1706-1709.

THE ROLE OF THERMAL VAPOR DIFFUSION IN THE SUBSURFACE HYDROLOGIC AND MINERALOGIC EVOLUTION OF THE MARTIAN CRUST. S. M. Clifford and J. Lasue, Lunar and Planetary Institute, 3600 Bay Area Blvd, Houston, TX 77058, clifford@lpi.usra.edu.

Introduction: Based on a conservative estimate of the volume of water required to erode the outflow channels, and the likely extent of their subsurface source regions, Carr [1] has estimated that Mars may possess a planetary inventory of water equivalent to a global ocean 0.5–1 km deep, the vast bulk of which is believe to be stored as ground ice and, possibly, as groundwater, in the subsurface [1, 2].

The distribution of ground ice on Mars is determined by the thermal structure of the crust, which mirrors the first-order variation in topography, but will extend down to a depth of from several to many km beneath the surface [2, 3]. In contrast, in the absence of atmospheric replenishment, groundwater will saturate the lowermost porous regions of the crust, having a water table (where unconfined by the cryosphere) that will conform to a surface of constant geopotential. As shown in Figure 1, the vertical distance separating any groundwater from the base of the cryosphere may, in some regions, be many kilometers while, in others, these two reservoirs of subsurface H_2O may be in direct contatct.

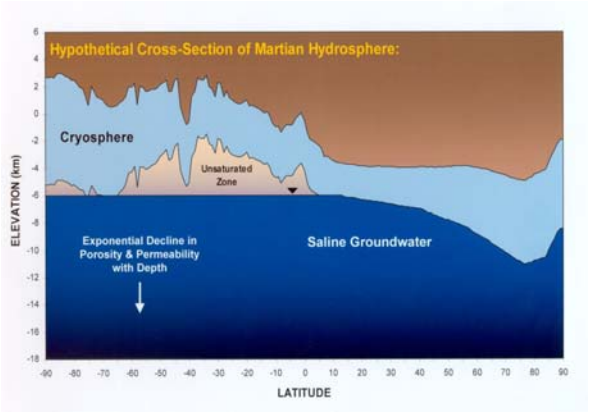

Figure 1. A hypothetical pole-to-pole cross-section of the Martian hydrosphere, illustrating the potential relationship of the cryosphere and groundwater.

Thermal vapor diffusion. Where there exists an unsaturated zone, between the base of cryosphere and groundwater table, the presence of a geothermal temperature gradient will give rise to a corresponding vapor pressure gradient, such that vapor will diffuse from the the higher temperature (higher vapor pressure) depths to the colder (lower vapor pressure) region at the base of the cryosphere by a process known as thermal vapor diffusion [2, 4].

The physical basis for this thermally-driven flux of vapor can be understood by considering first the equilibrium distribution of vapor in an isothermal crust. For this condition, the distribution of H_2O above the water table is given by the standard barometric relationship, where the scale-height of water vapor, above the water table, depends on the groundwater temperature.. For example, if the temperature at the grounwater table is 290 K, the water vapor scale-height will be ~36 km. Therefor, at a height of 1 km above the water table, the resulting baramotric reduction in vapor pressure is ~3% (Figure 2).

Now consider the effect of a geothermal gradient. Assuming a temperature gradient of 15 K km^{-1}, the crustal temperature at a height of 1 km above the water table is 275 K, which reduces the saturated vapor pressure at this height by 68%. Thus, the thermally induced gradient in saturated vapor pressure greatly exceeds the barometric gradient – causing vapor to diffuse upward in an effort to achieve an equilibrium barometric profile. However, as this vapor encounters the shallower and colder regions of the crust, the associated reduction in saturated vapor pressure causes some of the ascending vapor to condense, ultimately draining back to the water table as a liquid. As a result, the flux of vapor that leaves the groundwater table greatly exceeds that which finally reaches the freezing front at the base of the cryosphere. As shown by *Jackson et al.* [5], once a closed system has been established (i.e., the pore volume of the cryosphere has been saturated with ice), a dynamic balance of opposing fluxes is achieved, creating a circulation system of rising vapor and descending liquid condensate (Figure 3).

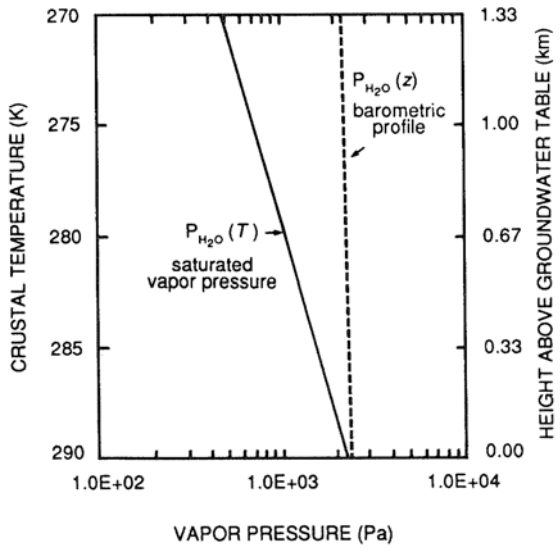

Figure 2. Comparison of the vapor pressure of H2O above a Martian groundwater table given by the barometric relationship (dashed line) and resulting from a geothermal gradient of 15 K km^{-1}.

For a geothermal gradient of 15 K km^{-1}, a groundwater temperature of 290 K, and effective crustal pore sizes of 1 and 10 μm, the flux of water vapor (per unit area) reaching the freezing front at the base of the cryosphere is ~8.3×10^{-3} – 2.8×10^{-4} m H_2O yr^{-1}. This flux is equivalent to the vertical transport of ~1 km of water every 10^6–10^7 years, or roughly 10^2–10^3 km of water over the course of Martian geologic history.

The magnitude of this thermally induced vapor flux was almost certainly greater in the past. Models of the thermal history of Mars suggest that 4 billion years ago the planet's internal heat flow was ~3–5 times larger than it is today [6, 7]. Since the flux rate is directly proportional to the temperature gradient, this implies a similar increase in the volume of water cycled through the early crust.

Consequences for the hydrologic and mineralogic evolution of the Martian crust. If the Martian valley networks were carved by atmospheric precipitation during a warmer, wetter Noachian climate, it suggests that Mars must have once

possessed groundwater flow systems similar to those now found on Earth, where, as a consequence of atmospheric recharge, the water table conformed to the shape of the local terrain (Figure 4, T0). However, with the transition to a colder climate -- and the progressive decline in Mars' internal heat flow -- a freezing front eventually developed in the regolith that propagated downward with time, creating a thermodynamic sink for any H_2O within the crust. Initially, water may have been cold-trapped within this developing region of frozen ground from both the atmosphere and underlying groundwater. However, as the pores of the near-surface regolith becames saturated ice, the deeper crust was ultimately sealed off from any further communication with the atmosphere. From that point on, the only source of water for the thickening cryosphere would have been the thermally driven upward flux of vapor from the underlying groundwater (Figure 4, T1)

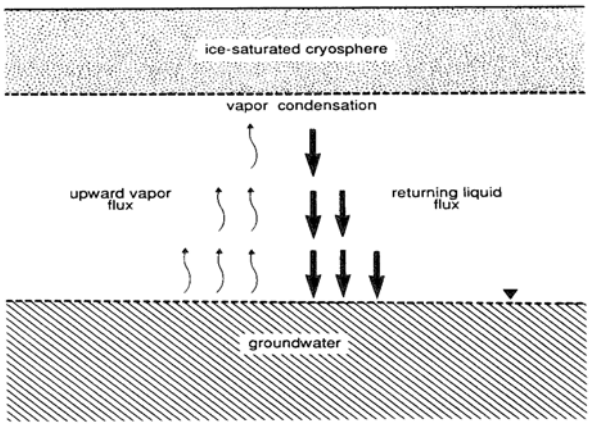

Figure 3. Low temperature hydrothermal cuirculation between the groundwater table and base of the cryosphere in response to the presence of a geothermal gradient.

With the elimination of atmospheric recharge, the elevated water tables that once followed the local topography eventually decayed. The continuity of pore space provided by the large-scale permeability of the crust would have then allowed the water table to hydrostatically readjust until it ultimately conformed to a surface of constant geopotential (Figure 4, T2) – a conclusion is supported by studies of areally extensive groundwater systems on Earth that experience little or no precipitation [2].

The time scale for any reasonable scenario of the transition from an early warm and wet Martian climate, to a sub-freezing one, is sufficiently great (i.e., $>10^6$ yrs) that the base of the cryosphere can be considered to have been in effective thermal equilibrium with the mean temperature environment at the surface. For transition times this long, the downward propagation of the freezing front at the base of the cryosphere would have proceeded at a rate that is suffi ciently slow (compared to the geothermally-induced vapor flux arising from the groundwater table) that the geothermal gradient would have had little trouble in supplying enough vapor to keep the cryosphere saturated with ice throughout its development.

From a mass balance perspective, the thermal evolution of the early crust effectively divided the subsurface inventory of water into two reservoirs: (1) a slowly thickening ice-rich region of frozen ground and (2) a deeper region of subpermafrost groundwater [2, 3]. Regardless of how rapid the transition to a colder climate actually was, the cryosphere has continued to thicken as the geothermal output from the planet's interior has gradually declined. One possible consequence of this evolution is that, if the planet's initial inventory of outgassed water was small, the cryosphere may have eventually grown to the point where all of the available H_2O was taken up as ground ice. Alternatively, if the inventory of H_2O exceeds the current pore volume of the cryosphere, then Mars has always had extensive bodies of subpermafrost groundwater.

Figure 4. The impact of the transition from a warm to cold early Mars on the evolution of the hydrosphere.

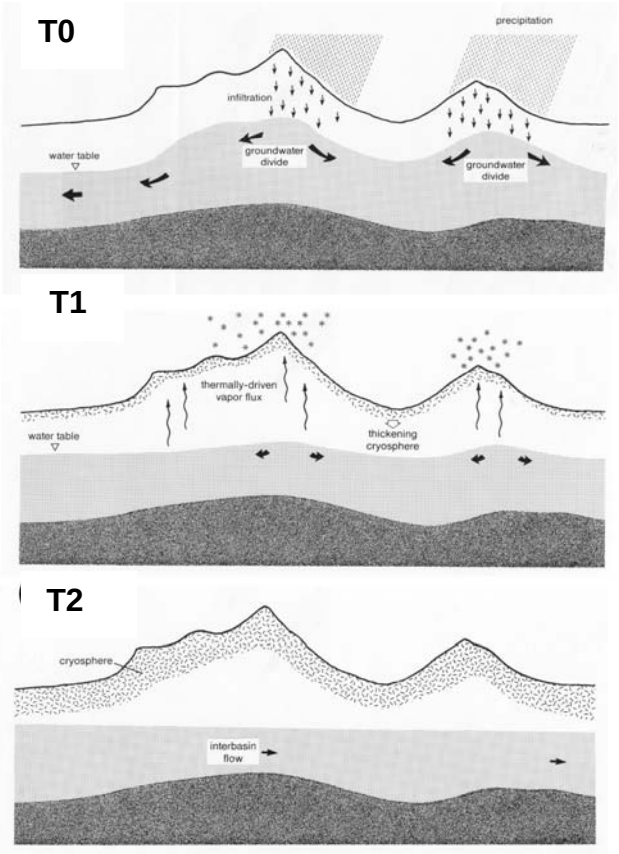

Ths geochemical evolution of the Martian crust was likely strongly affected by the convective cycling of 10^2–10^3 km of water (per unit area) between the water table and the base of the cryosphere (Figure 3) – which would have deplete the intervening crust of any easily dissolved substances, concentrating them in the underlying groundwater to levels far in excess of saturation. The resulting precipitation of these minerals beneath the water table is expected to have lead to widespread diagenesis and to the development of distinct geochemical horizon within the crust [*Soderblom and Wenner*, 1978].

References: [1] Carr, M. H. (1986) Icarus 68, 187-216. [2] Clifford, S. M. (1993) JGR 98, 10973-11016. [3] Clifford, S. M. and T. J. Parker (2001) Icarus 154, 40-79. [4] Clifford, S. M. (1991) Geophys. Res. Lett. 18, 2055–2058. [5] Jackson, R. D. et al. (1965) Nature 205, 314-316. .Fanale, F. P. (1976) Icarus 28, 170-202. [6] Solomon, S. C. and J. W. Head (1990) JGR 95, 11073-11083. [7] McGovern P. J. et al. (2004) JGR 109, E07007.

SPECTRAL REFLECTANCE DIVERSITY OF SILICA-RICH MATERIALS: INSIGHTS INTO STRUCTURE AND PETROGENESIS AND IMPLICATIONS FOR MARS. E. A. Cloutis[1], M. S. Rice[2], J. F. Bell III[2], S. A. Mertzman[3], D. L. Bish[4], and R. Renaut[5], [1]University of Winnipeg, Dept. of Geography, 515 Portage Ave., Winnipeg, MB, Canada R3B 2E9; e.cloutis@uwinnipeg.ca. [2] Dept. of Astronomy, 424 Space Sciences Building, Cornell University, Ithaca, NY, USA 14853; mrice@cornell.edu, jfb8@cornell.edu, [3] Dept. of Geosciences, Franklin and Marshall College, Lancaster, PA, USA; stan.mertzman@fandm.edu, [4]Dept. of Geological Sciences, Indiana University, Bloomington, IN, USA 47405-7000; bish@indiana.edu, [5] Dept. of Geological Sciences, University of Saskatchewan, Saskatoon, SK, Canada S7N 5E2; robin.renaut@usask.ca.

Introduction: Recently silica-rich materials have been discovered on the surface of Mars. They have been identified directly at Gusev crater by the APXS instrument on the MER rover [1] and spectrally by mini-TES [2], Pancam [3], and in the Valles Marineris area by CRISM [4]. To determine whether reflectance spectra of silica-rich materials can be applied to constrain possible formation conditions, we have undertaken a spectral reflectance study of a diverse suite of silica-rich materials and are subjecting a silica-rich sinter (opal-A) to long-duration (since Aug. 2008) exposure to simulated Mars surface conditions [5].

Background: Silica-rich materials can form on Earth in a wide variety of environments, including sedimentary, metamorphic, and igneous. Initially this suggests that the spectral reflectance detection and characterization of silica-rich materials on Mars may not be able to provide insights into petrogenetic conditions. However, the spectral reflectance properties of different silica-rich materials do vary as a function of formation and environmental conditions.

Spectral properties of silica-rich materials: Figure 1 shows the reflectance spectrum of common (non-gem quality) opal. Silica is spectrally featureless in the 0.35-2.5 µm region, and all the absorption bands arise from OH and H_2O, which can be present in a variety of forms, such as fluid inclusions and silanol (Si-O-H) groups. The absorption bands seen in the spectrum can be assigned as follows:

~0.95 µm: H_2O: $2\nu_1 + \nu_3$ and OH: $3\nu_{OH}$
~1.14 µm: H_2O: $\nu_1 + \nu_2 + \nu_3$
~1.36 µm: H_2O: $\nu_1 + \nu_3$
~1.41 µm: OH: $2\nu_{OH}$
~1.46 µm: H_2O: $2\nu_2 + \nu_3$
~1.78 µm: H_2O: rotational 2nd overtone (2d)+ ν_1 or ν_3 and OH: 2d + ν_{OH}
~1.9 µm: H_2O: $\nu_2 + \nu_3$
~1.94 µm: H_2O: $\nu_2 + \nu_3$
~2.25 µm: (Si-)OH: d + ν_{OH}

Many silica-rich materials are sufficiently transparent to discern low wavelength absorption bands.

The fine structure seen in the 1.9 µm region was also noted by [6], who resolved two bands: a higher-energy (lower wavelength; ~1.91 µm) (A) and lower-energy (higher wavelength; ~1.96 µm) (B) band. The strength of the B band relative to the A band was found to increase from amorphous to partially ordered opal. The A band was attributed to isolated H_2O molecules encased in the silica structure, free from hydrogen bonding. The broader B band was attributed to hydrogen-bonded more liquid-like H_2O molecules, as would be expected for H_2O molecules in larger voids.

The 2.2 µm region also exhibits two overlapping absorption features. Both are attributable to Si-OH rotation plus stretching with the difference being due to differences in hydrogen bonding. The higher-energy (lower wavelength; ~2.22 µm) (A) band has weaker hydrogen bonding than the lower-energy (higher wavelength; ~2.26 µm) (B) band. This suggests that the type A-OH molecules are present within the SiO_2 matrix while the type B OH molecules are present as surface silanol (SiOH) groups [6].

From this brief overview, it is evident that silica-rich materials yield a variety of OH/H_2O absorption bands that can potentially provide clues to both formation and environmental conditions. Conditions such as desiccation and freezing [7] should have variable effects on silica-rich reflectance spectra. For example, the loss of readily removed H_2O molecules should manifest iself in decreases in absorption band depths in the 1.94 and 2.26 µm regions versus the 1.91 and 2.22 µm regions. Fine structure in the lower-wavelength H_2O bands (<1.4 µm) has previously not been examined in as great detail. Upon freezing, spectral changes are expected in all of the H_2O-associated absorption bands with the exception of the 1.91 and 2.22 µm features; i.e., all of the H_2O bands where H_2O is present in clusters capable of forming an ice-like structure [7]. It is worth noting that the first few layers of H_2O molecules in contact with silanol groups may not be capable of forming an ice-like structure at lower temperatures due to strong hydrogen bonding with the underlying silanol groups [9].

Opal spectrum – temperature effects: The opal spectrum shown in Figure 1 provides a good illustration of some of the spectral details of silica-rich materials. The 1.4 µm region displays at least two partially overlapping absorption bands, near 1.41 and 1.46 µm. The shorter-wavelength band is assigned to the $2\nu_{OH}$ overtone, while the longer-wavelength band is associated with the H_2O $2\nu_2 + \nu_3$ combination/overtone (see table above) [6, 7]. The 1.9 µm region feature is also asymmetric looking, indicative of multiple absorption bands, specifically near 1.90 and 1.94 µm.

The shapes of the 1.4 and 1.9 µm absorption features are different between the -60°C and +20°C spectra. The silanol bands in the 2.25-µm region appear unaffected. Upon freezing, H_2O molecules in larger clusters can assume an ice-like structure, which has different band positions than liquid water [7]. The increase in relative intensity of the 1.46 and 1.94 µm bands is also seen in transmission spectra [7].

Silica gel spectrum – temperature effects: These spectral variations can extend to shorter wavelengths. Figure 2 shows spectra of silica gel exposed to 100% RH for 22 hours measured at 22° and -13°C. The 0.96µm region feature is to longer wavelengths at lower temperature (0.963 vs 0.962 µm), as expected.

Silica sinter – low pressure effects: Figure 3 shows reflectance spectra of a silica sinter (opal-A) from Wairakei, NZ. The spectra were acquired seven months apart, during which the sample was exposed to 5 Torr CO_2. The spectral changes include a shift of the 1.4 µm absorption feature to shorter wavelengths, a decrease in the 1.9 µm absorption feature depth, and the appearance of an absorption feature near 2.2 µm. Collectively these changes suggest a change in the form of the H_2O (1.4 µm feature), a loss of H_2O (depth of 1.9 µm feature), and an increase in silanol groups (appearance of 2.2 µm feature). They also indicate that exposure of silica-rich materials to Mars surface conditions can have dramatic spectral effects due to loss and rearrangement of any preexisting H_2O.

Discussion: Spectral detection of silica rich materials on Mars has been based on a downturn in Pancam reflectance from 934 to 1009 nm [3] and on the position, width and symmetry of the SiOH absorption feature in the 2.21-2.26 µm region [4].

The results from this study suggest that temperature, H_2O content and form of H_2O/OH can affect all of these spectral parameters. Ongoing studies are elucidating the effects of all of these parameters on reflectance spectra of silica-rich materials.

References: [1] Squyres S. W. et al. (2008) *Science, 320,* 1063-1067. [2] Ruff S. W. et al. (2008) *LPS XXXIX* Abstract #2213. [3] Rice M. S. et al. (2009) *Icarus,* in press. [4] Milliken R. E. et al. (2008) *Geology, 36,* 847-850. [5] Cloutis E. A. et al. (2008) *Icarus, 195,* 140-168. [6] Langer K. and Flörke O. W. (1974) *Fortschr. Miner., 52,* 17-51. [7] Aines, R. D. et al. (1984) *Phys. Chem. Min., 11,* 204-212.

Acknowledgments: This study is supported by research grants from NSERC, the Canadian Space Agency, the University of Winnipeg, and NASA MFRP.

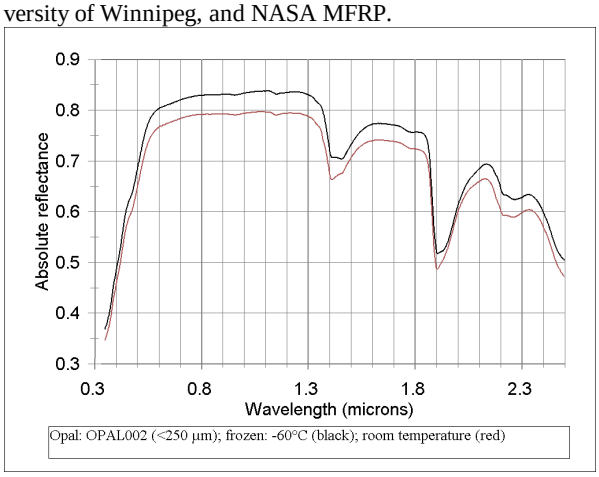

Fig. 1. Reflectance spectra of opal: room T and -60°C.

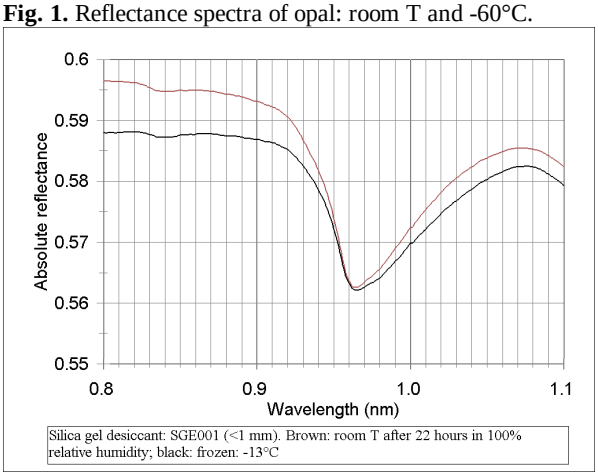

Fig. 2. Reflectance spectra of silica gel: room T and -13°C.

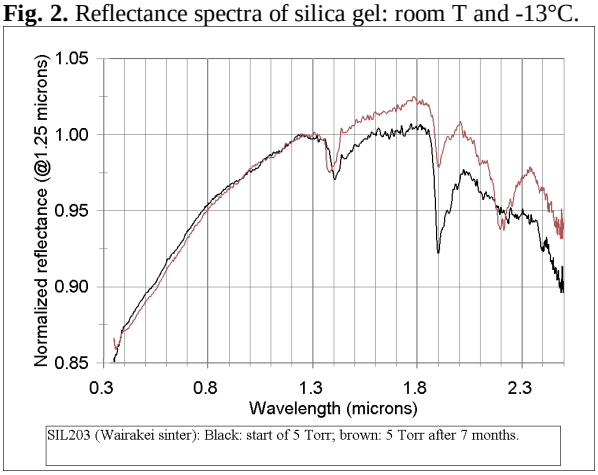

Fig. 3. Reflectance spectra of silica sinter (opal-A): ambient conditions and 5 Torr after seven months.

CRATER FLOOR POLYGONS: DESICCATION PATTERNS OF CRATER PALEOLAKES? M. R. El Maarry[1], W. Markiewicz[1], M. Mellon[2], W. Goetz[1] . [1]MPI für Sonnensystemforschung, 37191Katlenburg-Lindau, Germany, elmaarry@mps.mpg.de, markiewvicz@mps.mpg.de, goetz@mps.mpg.de. [2]Laboratory for Atmospheric and Space Physics, University of Colorado, Boulder, CO 80309 USA, mellon@lasp.colorado.edu.

Introduction: Crater-floor polygons have been reported before by [1]. The authors identified this feature through the use of the high resolution Mars Orbital Camera (MOC) images that were available at that time, among three other types of polygons in the circumpolar regions on Mars. Crater-floor polygons (CFPs) show a range of size from 75 to 200 meters in width, and have variable shapes, with mostly an orthogonal pattern of intersecting cracks. This cracking pattern resembles, albeit on a larger scale, those of dried-up karst lakes on Earth in certain periglacial environments such as Tuktoyaktuk in Canada [2], and even ancient dessicated lakes such as Coyote and Guano Lakes in the USA[3].

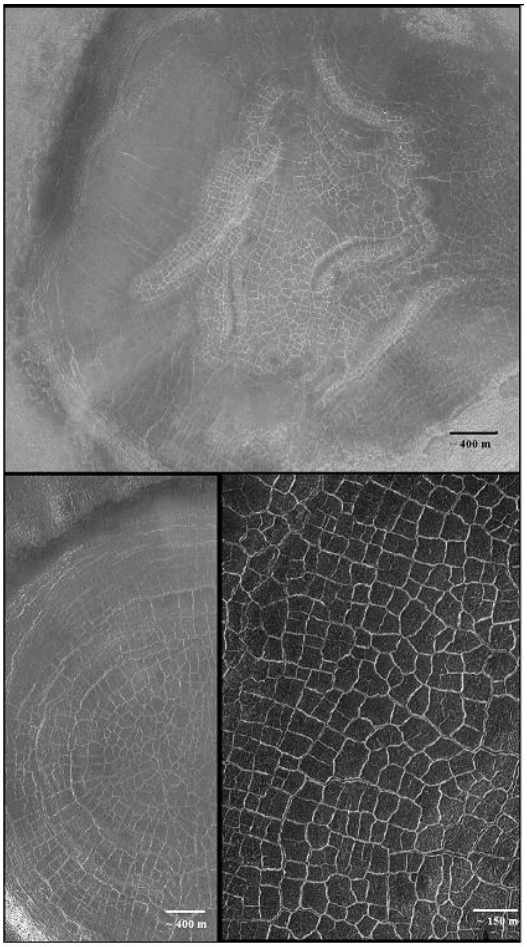

Fig.1. Various Crater-floor cracks by different imaging instruments: Upper panel: CTX. Lower left: MOC, and Lower right: HiRISE (Image IDs: MOC: M1900047, CTX: P17007514, HiRISE: PSP007372)

Using a larger database of high resolution images, i.e., complete data set of MOC, in addition to HiRISE and Context Imager (CTX), we buildup on the work of [1], by mapping all the craters that show cracked polygonal patterns in their floors. Our future work involves modeling these features to investigate weather they are infact, desicction patterns or thermal contraction polygons.

Observations: All the available MOC high resolution images (1.5-12 m/pixel) at good atmospheric conditions for latitudes from 0° to 80°N have been used for identifying the cracked patterns on crater floors, in addition to the datasets of the CTX camera (6m/ pixel resolution), and the HiRISE camera (0.3 m/ pixel resolution), that were available at the time of investigation. Fig. 1 shows examples of polygonal cracks in crater floors as seen by the different imaging instruments. Fig. 2 shows the locations of the craters that have been observed so far. It is clear that such features have a latitudinal dependence similar to other periglacial features, i.e., they are most visible in a band from 60° to 80° North. Similar mapping is being made for the southern hemisphere, but initial observations indicate that the features are following the same latitudinal trends.

Discussion & future work: Further investigation with HiRISE camera onboard the Mars Reconnaissnce Orbiter (MRO) shows that cracking patterns are extended to smaller and smaller scales in a fractal like manner within every 80-200m wide block. Mapping of the cracking features shows that they have a strong latitudinal dependence, with little or no regional or longitudinal preference. In regards to crater size dependence, there is no lower limit since these features are available in craters as small as 1 km in diameter. On the other hand, there seems to be un upper limit of almost 40 km. Craters larger than 40 km in diameter show either tentative features or none at all. There could be several reasons for that: Larger craters are generally older which may indicate that the features have eroded away with time. Another explanation is that the features are there but are obscured by glacial, or aeolian deposits, which is indeed, fairly common in high latitudes.

Morphological analysis of these cracking patterns shows that indeed, it is very difficult to differentiate between the two proposed mechanisms of formation, i.e., cyclic thermal contraction versus desiccation.

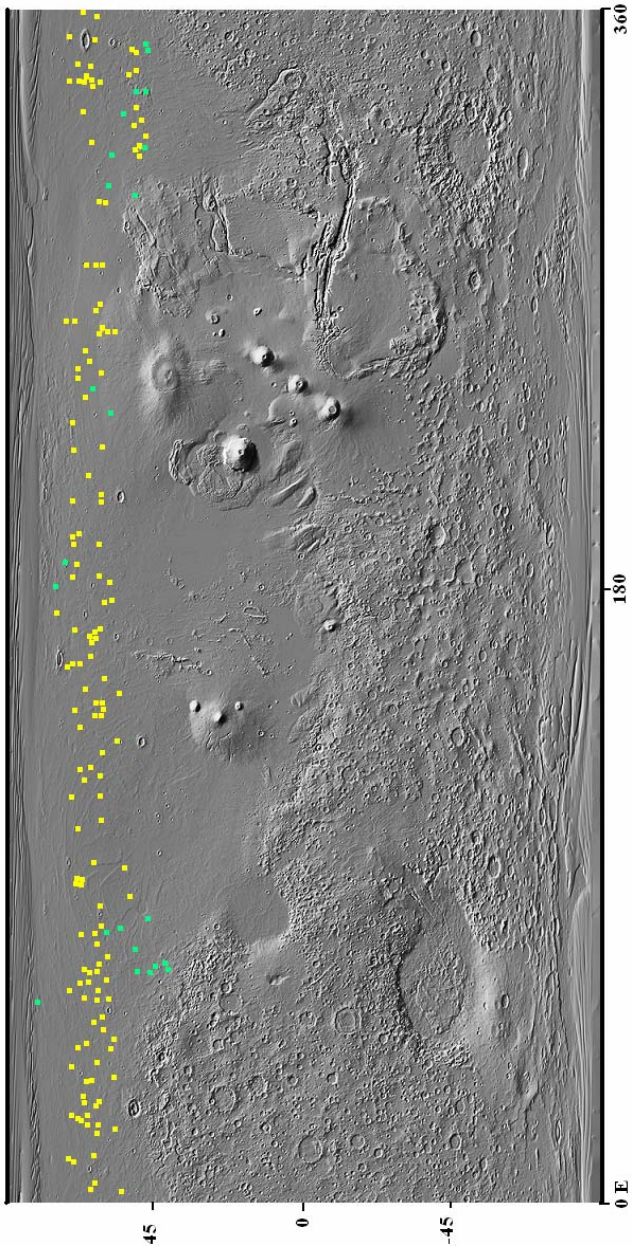

Fig.2. The map of spatial distribution of the crater-floor polygons in the northern plains on the surface of Mars. Yellow squares indicate definite observations, while green one indicate tentative signs due to erosion or the presence of a mantle material.

Thermal contraction would imply that the features are fairly recentrecent, and as a consequence are much younger than the craters themselves. An important distinctive property of polygons formed in this manner is that the cracks are continuously filled with aeolian deposits, which leads with cyclic thermal contraction and expansion to the development of polygonal terrains with slightly elevated ridges in place of the deep cracks. While this seems to be evident in some of the crater polygons, most of the polygonal cracks show no such elevated features. Furthermore, the size of the polygons
themselves is at least an order larger than typical thermal contraction polygons that are seen on Mars.

On the other hand, a desiccation mechanism would imply that the ground was fairly rich in volatiles at some point, and later suffered a loss of these volatiles either through sublimation or diffusion to deeper and more stable depths away from the surface, leading to increased surface tension on the surface, that ultimately led to formation of cracked fissures to relieve the strain. An origin for the volatile rich surface inside a crater could well be an ancient lake that formed after the crater impact as a result of the impact generated hydrothermal system, or simply the near surface circulation of volatiles by the same mechanism in smaller craters that are net expected to form a crater lake [4, 5]. Indeed, there are analogs on Earth that show similar cracking patterns in dried up lakes as seen in Fig. 3. However, this implies that a) these features are almost as old as the craters themselves, and b) there has to be a certain mechanism to explain the the larger size of these features compared to the ones seen on Earth which are almost an order of magnitude smaller. We hope that the future modeling will lead to a better understanding of the favorable mode of formation which indeed is essential to understanding the evolution of these interesting features.

References: [1] Kuzmin R. & Zabalueva E.. (2003)LPS Abstract #1912. [2] Soare R.J. et al., (2008), EAPS Letters, 272 382-393. [3] Neal J. et al., (1968), Geo. Soc. of America Bulletin v79, 69-90. [4] Newsom et al., (1996), JGR 101, 14951-14955. [5] Abramov O. & Kring D (2005), JGR 110, E12S09, doi: 10.1029/2005JE002453.

Fig.3. Dried-up lakes on earth as seen by Google Earth. Left Panel: Dried Karst lake in Koktoyaktuk, Canada. Polygons sizes are typically 15-20m. Right Panel: Cayote Lake, California. Polygon size range is 50-80m.

AQUEOUS PERCHLORATE LIQUID SOLUTIONS AT THE PHOENIX LANDING SITE. J. Hanley, V. F. Chevrier, T. S. Altheide, Arkansas Center for Space and Planetary Sciences, MUSE 202, University of Arkansas, Fayetteville, AR 72701, jhanley@uark.edu.

Introduction: The possibility of liquid water or brines on the surface of Mars is one of the most important topics in Mars research [1]. Recent results from NASA's polar lander, Phoenix, have indicated the presence of perchlorates (ClO_4^-) in the soil surrounding the landing site [2]. It is likely that these ions associate with either sodium or magnesium [3], which would make them ideal candidates for liquid brines on the surface [4, 5]. Very little is known regarding the behavior of these salts and their solutions in water, especially at low temperatures. Through evaporation experiments and geochemical modeling, we have studied the stability of perchlorates in a simulated Martian environment, and applied these results to Phoenix observations.

Experimental: Experiments were performed in a Martian simulation chamber using previously described methods [1]. Samples of $NaClO_4$ or $Mg(ClO_4)_2$ solutions at various concentrations (~20 to 50 wt%) are placed into a chilled CO_2 atmosphere (~263 K), which is then pumped down to Martian pressure (7 mbar). Using a precision balance, the mass loss rate was then measured and converted into evaporation rate.

Results: At temperatures between 256 and 269 K, evaporation rates of sodium perchlorate (Fig. 1A) range from 0.07 mm h^{-1} (55 wt% concentration at 258 K) to 0.49 mm h^{-1} (20 wt% concentration at 266 K). As seen in previous studies, evaporation rate is dependent on both temperature and concentration of the solution [1]. For instance, the evaporation rate of a 55 wt% solution ranges from 0.07 to 0.19 mm h^{-1} over a temperature range of 11 K. The evaporation rate is also dependent on perchlorate concentration: at 266 K, the 20 wt% sodium perchlorate evaporates at 0.49 mm h^{-1}, while the 55 wt% evaporates at 0.14 mm h^{-1}.

Magnesium perchlorate behaves in a similar manner (Fig. 1B). Evaporation rates range from 0.29 mm h^{-1} (20 wt% at 267 K) to 0.06 mm h^{-1} (49 wt% at 260 K). Again, evaporation rates are dependent on both temperature and concentration. For instance, at 264 K, the 20 wt% magnesium perchlorate evaporates at 0.29 mm h^{-1}, while a 49 wt% solution evaporates at 0.07 mm h^{-1}. In addition, temperature plays a suppressive role as seen in the 49 wt%: evaporation rates range from 0.17 mm h^{-1} (272 K) to 0.06 mm h^{-1} (260 K).

Experimental evaporation rates are slightly lower in magnesium perchlorate than for sodium perchlorate, due to lower water activity in magnesium perchlorate solutions (from stronger ionic interactions with Mg^{2+} and ClO_4^-), as demonstrated by the Pitzer model [6].

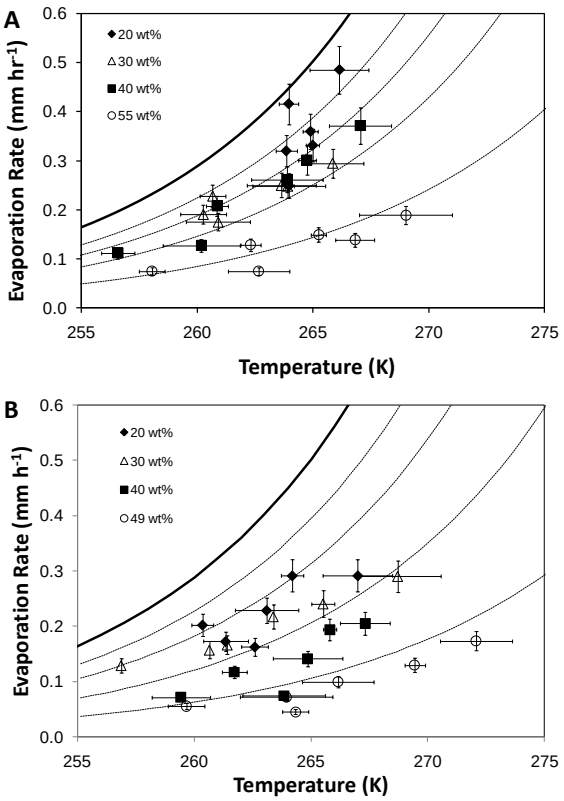

Figure 1. Evaporation rate of $NaClO_4$ (A) and $Mg(ClO_4)_2$ (B) as a function of sample temperature and concentration. Dashed lines are theoretical evaporation rates for each concentration, calculated from the Ingersoll (1970) equation and Pitzer model [1]. The solid line is for pure liquid water.

Discussion: From data collected from various sources [6, 7], and calculating the corresponding thermodynamic parameters, we determined the phase diagrams (Fig. 2). Three phases are known for sodium perchlorate: $NaClO_4$ (anhydrous), $NaClO_4 \cdot H_2O$ and $NaClO_4 \cdot 2H_2O$. The eutectic temperature was determined to be 236 K at a concentration of 52 wt%.

Less is known about the low-temperature properties of magnesium perchlorate $Mg(ClO_4)_2$. Calculated eutectic temperature was found to be 200 K at 43.9 wt% (Fig. 2B), close to previous measurements [8]. Mg-perchlorate has one of the lowest eutectic temperatures ever observed, allowing it to easily be liquid even at the Phoenix site. At low temperature, magnesium perchlorate has only one hydrate, $Mg(ClO_4)_2.6H_2O$. This hexa-hydrate is stable up to ~409 K, where it converts to $Mg(ClO_4)_2.4H_2O$ [9]. Thus the deliquescence property suggested before for magnesium perchlorate may not be valid on Mars,

since temperatures remain too low for the tetra-hydrate phase to form.

While temperatures are more favorable for liquid solutions on the warmest day, equilibrium vapor pressure values are also higher, and thus liquid perchlorate solutions are evaporating (Fig. 3). Paradoxically, on the coldest days, the atmospheric water vapor pressure crosses above the saturation value of eutectic $Mg(ClO_4)_2$ solutions, making the liquid thermodynamically stable for a few hours (Fig. 3A). This is not the case for $NaClO_4$ where a higher eutectic makes it evaporating or frozen, but never stable.

Using the Pitzer model to calculate the activity of liquid water in the solutions and our kinetic model of water evaporation [1], we extrapolated evaporation rates to the Phoenix landing site conditions. Input data included water vapor pressure and temperature measured by Phoenix's TECP [10] (Fig. 3A). We obtained the cumulated evaporated thickness over time (Fig. 3B). As previously demonstrated, the main control on the evaporation rate remains the temperature [1]. Liquid, if formed, could easily remain metastable for several days.

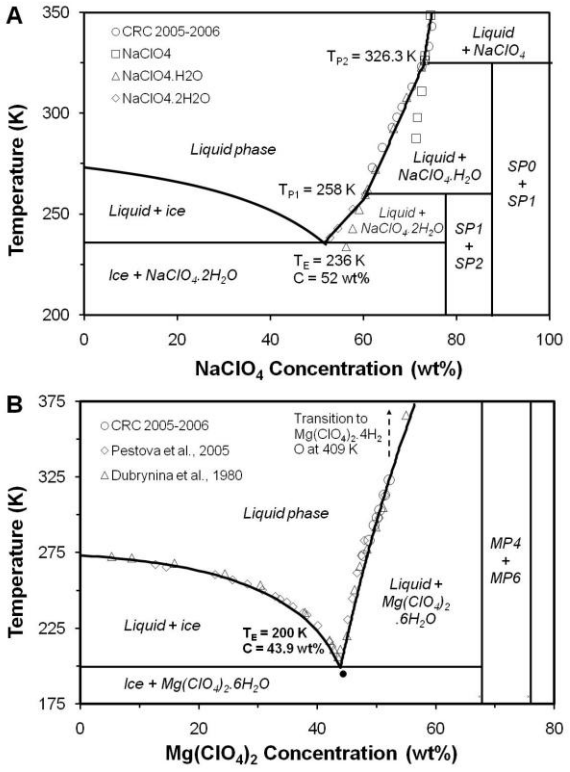

Figure 2. Phase diagram for (A) sodium and (B) magnesium perchlorates. Solid lines are determined by theoretical calculations based on data from various sources.

Conclusions: Thermodynamic calculations show that magnesium perchlorate remains liquid at much lower temperatures than sodium perchlorate. In these conditions, the combination of a larger stability field for liquid and lower evaporation rates show that magnesium perchlorate should be the dominant liquid phase at the Phoenix landing site. While there are short periods of time when $Mg(ClO_4)_2$ is stable on the surface, the majority of the time it is either evaporating or frozen (and likely sublimating). Thus, there must be an efficient mechanism to replenish the lost water for a solution to remain stable over long timescales.

References: [1] Chevrier, V. F., and T. S. Altheide (2008), *GRL*, *35*, L22101, doi:10.1029/2008GL035489. [2] Hecht, M. H. et al (2009) *LPS XL*, Abstract #2420. [3] Marion, G.M. et al (2009) *LPS XL*, Abstract #1959. [4] Hanley, J. et al (2009) *LPS XL*, Abstract #1380 [5] Renno, N.O. et al (2009) *LPS XL*, Abstract #1440. [6] Pitzer, K. S. (1991), Ch. 3. *Activity coefficients in Electrolyte Solutions. 2nd Edition*, 75-154, CRC Press. [7] Chretien, A., and R. Kohlmuller (1966), *Nouveau Traite de Chim. Min., Vol 2 (#1), Sodium and Lithium*, 344-354. [8] Pestova, O. N. et al. (2005), *Rus J. App Chem*, *78*, 409-413. [9] Dobrynina, T.A. et al. (1980), *Rus. J. Inorg. Chem.*, *25*, 1237-1239. [10] Hudson, T.L. et al. (2009), *LPS XL*, Abstract #1804.

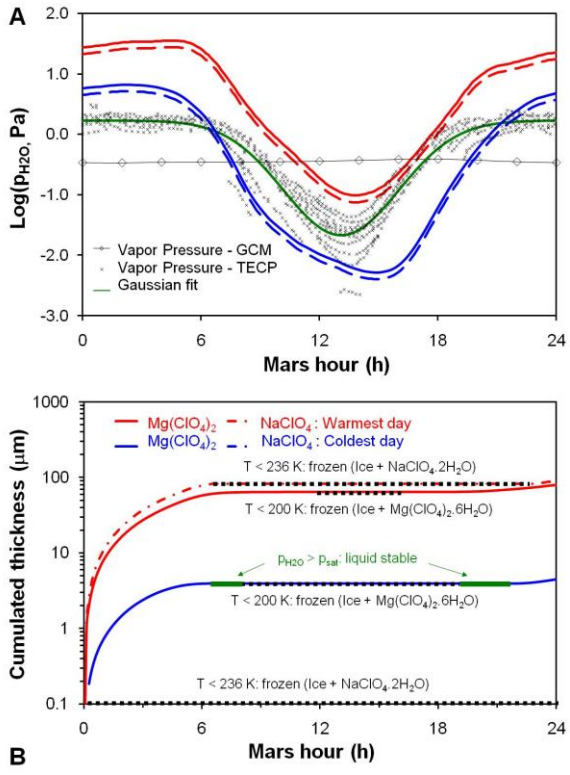

Figure 3. (A) Water vapor pressures. Blue and red curves are equilibrium pressure above eutectic solutions of $NaClO_4$ (dahed) and $Mg(ClO_4)_2$ (plain) for the coldest and warmest days, respectively. (B) Integrated evaporation curves over time after noon for $Mg(ClO_4)_2$ (plain lines) and $NaClO_4$ (dashed lines). Red is for the warmest day, blue for the coldest. Thick dotted black lines represent frozen periods. Green areas represent thermodynamically stable periods for liquid $Mg(ClO_4)_2$ eutectic solutions.

REGIONALLY COMPARTMENTED GROUNDWATER FLOW ON MARS. K. P. Harrison[1] and R. E. Grimm[1], [1]Southwest Research Institute, 1050 Walnut St, Ste 300, Boulder, CO 80302, harrison@boulder.swri.edu.

Introduction: Groundwater likely influenced the erosion or weathering of large Martian fluvial features, including outflow channels [1, 2] and valley networks [3, 4]. Groundwater may also have contributed to the formation of widespread sulfate and phyllosilicate deposits [5, 6], and a variety of bedrock outcrop features observed by the Mars Exploration Rover Opportunity [7]. The spatial distribution of these phenomena suggests that groundwater flow might once have been widespread on Mars. Groundwater simulations to date have assumed laterally uniform permeabilities capable of supporting global-scale flows [e.g., 8, 9]. It has been argued [10] that in terrestrial crust, the pervasive presence of fracturing prevents any large-scale geologic formation from being considered impermeable, implying (for both the earth and Mars) that lateral hydraulic connectivity is essentially unlimited.

Global-scale groundwater flows are not, however, observed terrestrially because high precipitation rates shape the water table to a subdued replica of the topography, limiting hydraulic gradients to small spatial scales. Arid climates allow at most regional-scale groundwater flows. If the terrestrial and Martian crusts are hydrologically similar, the globally arid nature of Mars may have allowed truly global flows. However, the wide distribution of Martian groundwater-related features does not explicitly require global-scale flow: it is possible that groundwater circulated in isolated local- to regional-scale aquifers.

We suggest a means of constraining the viability of global-scale flow on Mars using chaotic terrains (CT). CTs are groups of large (10s km) randomly arranged mesas resulting from the collapse of an ice-filled permafrost layer (cryosphere) due to high aquifer pore pressures exerted from below [1]. Cryosphere disruption allows pore pressures to be released through the discharge of large volumes of groundwater to the surface. CTs thus serve as markers for high pore pressures in the Martian aquifer. A groundwater simulation that responds to high pore pressures with a cryosphere disruption mechanism can thus be used to search for global-scale groundwater flow patterns consistent with observed chaotic terrain locations.

Model: We implement the above approach with a groundwater model that employs aquifer recharge as a means of generating high pore pressures [11]. Downward infiltration of recharged water locally raises the water table, producing lateral hydraulic gradients that drive groundwater radially outwards to other parts of the aquifer. Pore pressures rise regionally (and eventually globally) and, at some location determined by elevation and proximity to the recharge zone, groundwater "breakout" occurs, i.e. pressures reach a value high enough to open fractures in the cryosphere through which groundwater then issues. This breakout mechanism causes a local- to regional drop in pore pressures and so influences the location of subsequent breakouts.

Of particular importance to the spatial scale of groundwater flow is the lateral variation of permeability k. In lieu of observational constraints we adopt a stochastic approach. Depth-averaged $\log_{10}k$ (model depth is 19 km) is made to vary laterally about a mean value of -12.7 (with k in units of m^2) with a standard deviation of 0.5. We impose a lateral length scale of 15° (about 900 km, based on average geologic unit dimensions). We generate 100 stochastic realizations, each of which is implemented in an independent model. We also consider the following model variations: 1) south polar recharge (nominally, recharge is over Tharsis), 2) alternative topography reflecting the assumption that significant cryosphere disruption occurred just prior to large-scale collapse of CTs, incision of outflow channels, and the widening of the Valles Marineris canyons, 3) breakout when pore pressures reach hydrostatic values (nominally, lithostatic values are required), 4) k length scale is increased to 75° to introduce more chaos-to-channel variability, 5) standard deviation of $\log_{10}k$ is increased to 1.0. For each unique combination of the above variations, we ran 100 models, resulting in a total of 3200.

Results: Results from the first three model variations are shown in Fig. 1. Eight unique combinations arise, each with 100 models covering the same set of independent permeability realizations. For each combination, we plot on a single map the breakout locations from all 100 models. Circles indicate breakout sites, with circle diameter proportional to the number of models from the suite of 100 that produced a breakout at the circle center. Thus, for example, the single large circle over Hellas in Fig. 1a indicates that most models in the suite (97) produced a breakout at the same location. We omit breakouts that are initiated later than 1 Ga: we regard this as a suitable upper limit to the period of outflow channel initiation from approximately the end of the Noachian to the early Amazonian.

Results from model suites with the last two variations (permeability statistics) show a somewhat greater

number and spatial diversity of breakouts, but the general distribution seen in Fig. 1 is conserved.

Discussion: Our results indicate that cryosphere disruption is not widely predicted for the circum-Chryse and eastern Hellas CTs, the traditionally accepted sources of groundwater discharge for outflow channel flooding. Even in the model suite with the most favorable initial conditions (hydrostatic breakout pressure and long *k* path length), only 16% of models produce cryosphere disruption at the circum-Chryse CTs, and these were limited largely to Hydraotes Chaos, the deepest CT. Furthermore, many models produced cryosphere disruption in Amazonis and western Hellas Planitae where no evidence of disruption is observed. We conclude that global-scale groundwater flow, even when limited to tortuous flow paths connecting regional-scale high permeability zones, cannot produce a cryosphere disruption pattern commensurate with observations. It is thus likely that Martian groundwater flow was locally or regionally isolated. Isolation may be due to limited hydraulic connectivity imposed by geologic formations not included in our model, or by the limited distribution of groundwater.

A further conclusion is that cryosphere disruption in the Valles Marineris canyon system (driven by aquifer recharge over Tharsis) is highly probable, even if groundwater flow is assumed to be regional. The position of the canyon system upstream of chaotic terrains suggests that groundwater discharge through Valles Marineris faults may have been a significant, if not dominant, source of water for outflow channel flooding. This mechanism already constitutes the standard formation model of outflow channels elsewhere on Mars, including Athabasca and Mangala Valles. Our results therefore suggest that the role of CTs in circum-Chryse outflow channel formation must be carefully revisited and, if necessary, modified. If the formation of CTs can be shown to be unrelated to high aquifer pore pressures, then global-scale groundwater flow remains a possibility.

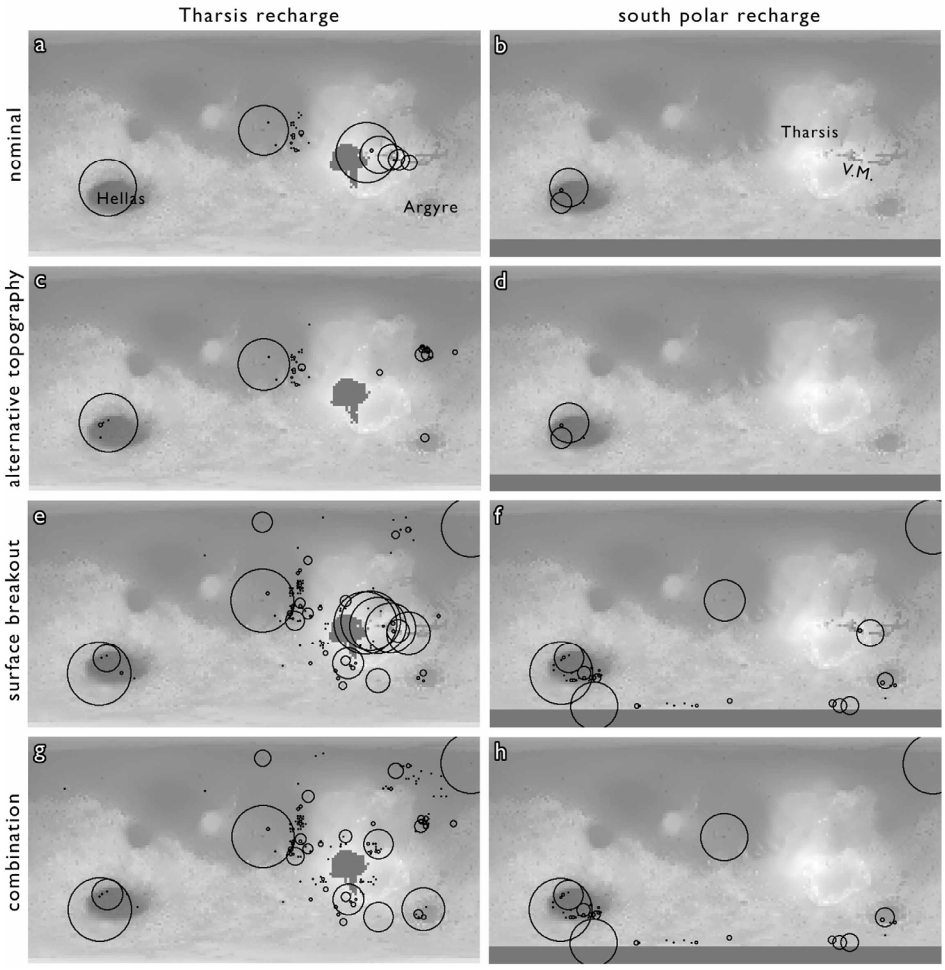

Figure 1. Compilation of breakout locations for nominal stochastic permeability models. Each frame superimposes breakouts from 100 independent simulations. Circle diameter is explained in the text. As indicated by uniformly grey areas, left column frames have Tharsis recharge, right column frames have south polar recharge. Each row indicates the affect of a model variation delineated in the text.

References: [1] Carr, M. H. (1979) *JGR*, *84*, 2995–3007. [2] Baker, V. R. (1982) *The Channels of Mars*, Univ. Tx. Press. [3] Craddock, R. A., Howard, A. D. (2002) *JGR*, *107*, doi: 10.1029/2001JE001505. [4] Luo, W., Howard, A. D. (2008) *JGR*, *113*, doi: 10.1029/2007JE002981. [5] Gendrin, A. N., *et al*. (2005) *Science*, *307*, 1587-1591. [6] Poulet, F., *et al*. (2005) *Nature*, *438*, 623-627. [7] Grotzinger J. P. *et al*. (2005) *Earth Plan. Sci. Lett.*, *240*, 11-72. [8] Harrison, K. P., Grimm, R. E. (2004) *GRL*, *31*, doi: 10.1029/2004GL020502. [9] Andrews-Hanna, J. C., Phillips, R. J. (2007) *JGR*, *112*, doi: 10.1029/2005JE002881. [10] Clifford, S. M. (1993) *JGR*, *98*, 10973-11016. [11] Harrison, K. P., Grimm, R. E. (2009) *JGR*, *114*, doi: 10.1029/2008JE003300.

EXPERIMENTAL SIMULATION OF THE EFFECT OF VISCOUS FLUIDS ON MARTIAN GULLY FORMS. Howe, K. L.[1], Rivera-Valentin, E. G.[1], Chevrier, V.F.[1], Dixon, J. C. [1, 2]; 1- Arkansas Center for Space and Planetary Sciences and [3]Department of Geosciences, University of Arkansas, Fayetteville AR 72701; 2-Department of Geology, 113 Ozark Hall, University of Arkansas, Fayetteville, Arkansas, 72701. khowe@uark.edu

Introduction: Many studies on martian gully formation processes [1,2,3,4] have been conducted since Malin and Edgett reported their discovery on Mars's surface [5]. The processes that form these features remain elusive despite these investigations. This may be partially due to the lack of experimental simulations of martian gullies; numerical modeling is more often invoked in order to attempt to explain their origin [6]. Gully simulation is important for experimentally validating formation hypotheses and numerical models. Both dry and wet flow processes have been proposed for the different types of gullies seen on Mars [1,2,3,4].

We have developed a set of flume simulation experiments to test gully formation processes at Earth surface conditions with the objective to produce gullies in the flume with morphometric parameters similar to those seen on Mars [7,8]. The objective of the study reported here is to simulate flows of higher viscosities to account for the potential role of brines [6] and/or debris flows [3] in gully formation.

Figure 1. 1.5 × 1 meter flume used in our experiments of gullies flow.

Methods: In order to vary the viscosity of the fluid in the simulations, Natrosol, a commercial natural cellulose ether, was added to the water. The viscosity of the solution is a direct function of the Natrosol concentration. Moisture content of the Natrosol powder was measured and taken into account during solution creation. Natrosol powder was slowly added to water with constant stirring. To date, the resulting viscosities range from 0.003 to 0.023 Pa.s (i.e. a range similar to values extrapolated from observations of gullies [3] and measurements on brines [6]). We also colored the solutions to increase contrast with sand and to experiment with superimposition of successive flows.

Experiments were conducted in a 1.5 × 1 m flume (Fig. 1) filled with medium grain size sand. The experiments were run over a slope angle of 20°, similar to the average slope of martian gullies [4]. A 500 mL Natrosol/water solution was poured into a funnel attached to a 5/8'' tube resting on the surface.

The flow was recorded using a digital video recorder and digital images were taken after the simulations were complete; this allowed for later image analysis and interpretation of morphometric features. Gully parameters were measured after photos were taken: alcove and apron lengths were recorded as well as the width of each gully section every 5 cm; when appropriate, levee height and length were measured. These dimensional parameters

Figure 2. Left: incised gullies from the inside of a southern near polar crater; White arrows denote North and down slope is toward the bottom of the image Right: low viscosity (0.005 Pa.s) flows simulated in a flume from the same point source.

were chosen for their relevance to observations of gullies from orbit.

Results: The 0.1 wt% and 0.3 wt% Natrosol solutions yielded viscosities of 0.003 and 0.005 Pa.s, similar to those of some brines [6]. These solutions formed gullies with distinct alcoves, channels and aprons as well as levees. Multiple simulations from the same point source yielded similar morphologies stacked on top of each other (Fig. 2).The second flow traveled down the same channel and formed a fan in a similar area and with similar properties.

Features produced with higher viscosity solutions (0.023 Pa.s) show channels that generally widen down slope with very little topography. Discrete levees can be seen on the edges of the flow, only 0.5-1.0mm high. Velocity of these solutions was about 1.0 cm/sec, much slower than the 50cm/sec velocities of the lower viscosity solutions. Channel lengths for the higher viscosity flows were 110 cm, about 30 cm longer than channels of low viscosity flows.

Discussion: The viscosity of the solution has a clear effect on the morphologies of the simulated gullies, as was expected. As seen in Fig. 2, the lower viscosity solutions (0.1% and 0.3% Natrosol) created

Figure 3. Left: Slope streaks from the inside of a southern near equator crater. White arrows denote North and down slope is toward the bottom of the image. Right: higher viscosity flows (0.023 Pa.s) simulated from a point source in a flume; change of shape at the bottom of flow due to the flow hitting the wall of the flume.

gullies with similar morphologies as those produced during water and water/ice slush experiments [, 7,8] and those described by Malin and Edgett [5]. These lower viscosity solutions may be analogous to gully formation by liquid brines [6]. Other analogues of the high velocity debris flows are gullies carved from debris flows. Multiple measurements taken from all three gully sections will be used for future modeling work to further constrain the data.

Higher viscosities generated low velocity flows in our simulations (about 1cm/sec). The resulting features were more linear with little to no topography (Fig. 3). We interpret this result as absence of infiltration in the sand of the fluid, due to its too high viscosity. These morphologies strongly resemble slope streaks, which are found in similar latitude regions as gullies. Slope streak formation processes are debated as to a wet or dry genesis [9]. Martian slope streaks have a wedge-shaped and branching to braided "fan" area that shows no deposition; there is little to no topography observed. Slope streaks appear to originate from a point source, as was used in our simulations. Our simulations are also consistent with observations of scarps at the edges of the slope streaks [9]. Therefore, slope streaks could eventually result from the flow of a viscous fluid on the surface, or more probably be linked to the relationship between viscosity and grain size. Further scale analysis will help solve this issue.

Conclusions: Depending on the viscosity of the fluid, our experiments may represent brine solutions, debris flows, and even slope streaks. The low viscosity flows produced gullies similar to those originally documented on Mars, whereas the higher viscosity solutions produced morphologies similar to slope streaks. This data can be used to constrain the formation of different gully types as well as be collected to validate numerical models. Further work will especially focus on the effect of the viscosity versus grain size relationship to explain the transitions between different morphologies. Such experiments with tightly controlled parameters will also be a useful tool for validation of numerical fluid flow modeling.

References: [1] Costard, F., et al. (2002) *Science*, *295*, 110-113. [2] Heldman, J. L., et al. (2007) *Icarus, 188,* 324-334. [3] Mangold, N., et al. (2003) *JGR, 108, E4,* 5027. [4] Dickson, J. L., et al. (2007) *Icarus, 188,* 315-323. [5] Malin, M.C., and Edgett, K. S. (2000) *Science, 288,* 2330-2335. [6] Chevrier et al. (2009) *JGR*, in press. [7] Coleman, K. A., et al. (2009) *Planetary & Space Sci.,* doi:10.1016/j.pss.2008.11.002. [8] Coleman, K. A., et al (2008) *LPSC XXXIX,* Abstract #2240. [9] Phillips, C. B., et al. (2007) *Geophysical Research Letters, 34.*

DELIVERY AND REDISTRIBUTION OF VOLATILES ON MARS DURING THE BASIN-FORMING EPOCH: AN OVERVIEW. D. A. Kring[1], [1]USRA Lunar and Planetary Institute, 3600 Bay Area Blvd., Houston, TX 77058 (kring@lpi.usra.edu).

Introduction: Samples collected during the Apollo era suggest impact bombardment of the lunar surface was particularly intense early in solar system history [1,2]. There are hints that the lunar cataclysm was actually an event that resurfaced planets throughout the inner solar system [3,4]: meteoritic fragments from the asteroid belt indicate objects between 2 and 5 AU were shock-metamorphosed between ~3.5 and 4.0 Ga; furthermore, our first sample from the ancient cratered highlands of Mars (meteorite ALH84001) was shock-metamorphosed 3.92 Ga [5]. Thus, the process first detected on the Moon may have greatly affected all inner solar system planets, including Mars.

Basin-forming Epoch on Early Mars: If the same bombardment that affected the Moon also affected Mars, then at least 6,000 impact craters with diameters in excess of 20 km were likely produced [4]. Many of these were basin-forming impact events and, although there is still discussion about the ages of the largest basins (Utopia, Chryse, Hellas, Argyre, Isidis), there is a possibility that all of them were produced in a short (<200 Ma) interval of time. The resurfacing of Mars may have been so severe that Noachian features may have been produced in a rather short period of time associated with the bombardment, rather than an extended period of time that stretched back to ~4.5 Ga.

Source of Impacting Objects: Rare geochemical fingerprints of impactors in the Apollo impact melts suggest the impacting objects were dominantly asteroids, rather than comets or Kuiper Belt objects [4]. In addition, the size distribution of impact craters on the Moon and Mars seems to require impactors with a size distribution similar to that seen in the asteroid belt [6]. The latter suggests that less than 15% of the impactors were comets, consistent with the current flux. The noble gas composition of Mars atmosphere also hints that the contribution from comets was small [7].

Implications for Mars: Calculations of the delivery of biogenic elements to Earth during a period of late heavy bombardment [4,8] serve as an initial proxy for conditions on Mars. These results indicate that substantial biogenic material, including water, was delivered to planetary surfaces. However, they also indicate that the bulk of these materials must have already been present because the flux, although substantial, cannot provide the inventory currently observed. Thus, most biogenic elements, including water, were likely part of the original complement of accreted material. A late heavy bombardment may have augmented abundances of biogenic elements in planetary surfaces and redistributed them, but it was not the primary source of those materials.

Redistribution of Water: Large impact events in water-bearing planetary crusts, like that on Mars, will generate vast subsurface hydrothermal systems [e.g., 9-12]. These systems may span the entire diameter of a crater and extend to depths of several kilometers. They can also be very long-lived on Mars [13,14] and, thus, may have chemically and mineralogically altered Mars' crust [15-17]. This may be a major source of the phyllosilicates and other alteration phases identified in Noachian terrains. Even if the water is frozen in Mars' crust prior to an impact, it can be liquefied and vented to the surface. Vented material might be added directly to the atmosphere and/or form a crater lake as part of a more complex hydrological cycle.

These same impact events will vaporize hydrous material during the compressional phase of the impact and eject it into the atmosphere during the excavation phase. Vapor-rich plumes may have altered short-term weather and potentially long-term climate on Mars. Substantial precipitation may have followed [18]. Both this process and that associated with impact-generated hydrothermal activity may be the source of, or a contributor to, aqueous surface flow that carved the Noachian surface of Mars.

References: [1] Turner G. et al. (1973) *Proc. 4th Lunar Sci. Conf.*, 1889-1914. [2] Tera F. et al. (1974) *Earth & Planet. Sci. Letters, 22*, 1-21. [3] Bogard D. D. (1995) *Meteoritics, 30*, 244-268. [4] Kring D.A. and Cohen B.A. (2002) *J. Geophys. Res., 107*, 4-1,4-6. [5] Turner G. et al. (1997) *Geochim. Cosmochim. Acta, 61*, 3835-3850. [6] Strom R. et al. (2005) *Science, 309*, 1847-1850. [7] Swindle T.D. and Kring D.A. (2001) *11th V.M. Goldschmidt Conference*, Abstract#3785. [8] Kring D.A. (2008) *NLSI Lunar Scienc Conference*, Abstract #2140. [9] Newsom H.E. (1980) *Icarus, 44*, 207-216. [10] Naumov M.V. (2002) in *Impacts in Precambrian Shields*, 117-171. [11] Zurcher L. and Kring D.A. (2004) *MAPS, 39*, 1199-1222. [12] Abramov O. and Kring D.A. (2007) *MAPS, 42*, 93-112. [13] Rathbun J.A. and Squyres S.W. (2002) *Icarus, 157*, 362-372. [14] Abramov O. and Kring D.A. (2004) *J. Geophys. Res., 109* (E10007), doi: 10.1029/2003JE002213. [15] Schwenzer, S. P. & Kring, D. A. (2008a) *LPSC*, **XXXIX**: #1817. [16] Schwenzer, S. P. & Kring, D. A. (2008b) *Workshop on the Early Solar System Bombardment*, Abstr. #3027. [17] Schwenzer, S. P. & Kring, D. A. (2008c) *Workshop on Martian Phyllosilicates: Recorders of Aqueous Processes?* Abstr. # 7014. [18] Segura T.L. et al. (2002) Science, 298, 1977-1980.

IRON SULFATE AND SULFIDE SPECTROSCOPY AT THERMAL INFRARED WAVELENGTHS. Melissa D. Lane[1], Janice L. Bishop[2], M. Darby Dyar[3], Penelope L. King[4], and Brendt C. Hyde[5], [1]Planetary Science Institute, Tucson, AZ (lane@psi.edu), [2]SETI Institute, Mountain View, CA, [3]Mount Holyoke College, South Hadley, MA, [4]Institute of Meteoritics, U. New Mexico, Albuquerque, NM, [5]U. Western Ontario, London, Ontario, Canada.

Introduction: Ferric *sulfate* minerals were identified in several light-toned subsurface soils in Gusev Crater, Mars, that were exposed by the Mars Exploration Rover (*Spirit*) wheels. Although the identified ferric sulfate minerals vary from site to site [1-3], several different sulfates have been identified, including ferricopiapite (dominating the Paso Robles bright track soils) [2], (para)coquimbite, fibroferrite, rhomboclase, and hydronium jarosite, and possibly minor (para)butlerite or metahohmanite. Recent work by the Mars Reconnaissance Orbiter (MRO) CRISM (visible-near infrared) team suggests that the polyhydrated sulfates such as ferricopiapite may be widely present on Mars, and that ferricopiapite may be found in a partially dehydrated state in inverted channels in Juventae Chasma and other nearby Chasma in the Valles Marineris region [4]. A growing laboratory suite of ferric sulfate minerals (including the minerals mentioned above as well as many other ferric sulfates, some of which were dehydrated intentionally) have been analyzed using a thermal emission (mid-infrared) spectroscopic technique to continue to provide well-defined and well-understood emissivity spectra of a large range of ferric sulfate minerals in order to aid and expedite the identification of these minerals and their dehydration products using TES and Mini-TES (mid-infrared) emission data from Mars.

This work also includes thermal emission studies of a variety of *sulfide* minerals for a similar purpose of identifying them on Mars. Sulfides occur in terrestrial volcanic terrains similar to igneous terrains on Mars. On Earth sulfides are abundant in hydrothermal areas on land and undersea "black smokers" as seen and sampled by the submersible, *Alvin*, at the East Pacific Rise. Sulfides also are found in Martian meteorites. Hence, sulfides are an important mineral class to understand because they also are possible precursor minerals [5] that can follow an oxidation pathway (with proper hydration and pH) to form ferric sulfate and other sulfate minerals [e.g., 2,3,6].

Objective: We will present thermal emissivity spectra of: 1. a suite of ferric sulfates, 2. dehydrated ferric sulfates (dehydration products), and 3. a suite of sulfide minerals. All of these minerals have an application to interpretating mid-infrared data from Mars.

Ferric Sulfates: Ferric sulfates are formed by a series of oxidation, dehydration, and neutralization reactions [2] and are formed in low pH environments such as acid-mine drainage sites on Earth. Ferric sulfates form in generally similar conditions; however, their crystallography and emissivity spectra are quite diverse as evidenced by their varied spectra (Figure 1).

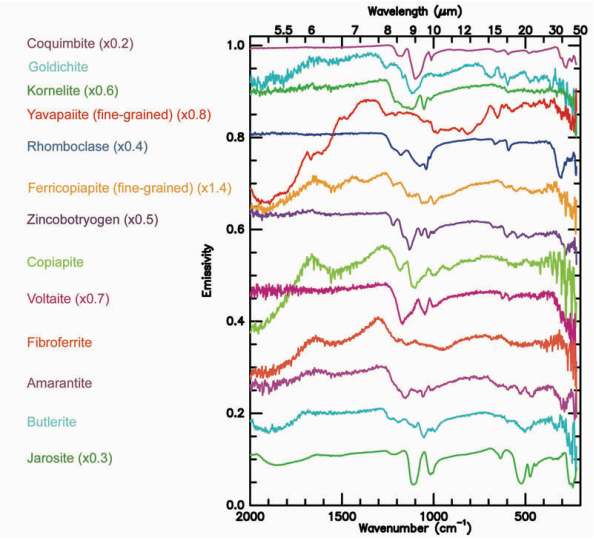

Figure 1. Thermal emissivity spectra of a suite of ferric sulfates. The spectra were acquired at the Mars Space Flight Facility at Arizona State University.

Dehydration of Ferric Sulfates: Two ferric sulfate samples were selected for dehydration measurements [4]. These samples included a synthetic kornelite (ML_S105) and a copiapite sample (JB787). The kornelite sample was measured when first synthesized, and later measured after natural (ambient) dehydration that caused the formation of rhomboclase and the sample color to change from light purple to yellow. The copiapite sample was measured in emissivity, then heated in a step-wise fashion to 100 ˚C, 200 ˚C, 250 ˚C, and finally 300 ˚C, holding the temperature for 30 minutes at each temperature increment. The final product was again measured to obtain the emissivity spectrum. These original sample spectra, as well as the dehydration product spectra are shown in Figure 2.

The dehydration experiments have direct application to understanding the surface of Mars and the potential for various sulfates to be formed and altered.

Recent studies of the CRISM team have found spectral evidence that significant amounts of ferricopiapite in a partially dehydrated state may occur on the surface of Mars in inverted channels in Juventae Chasma and other neaby Chasma in the Valles Marineris region.

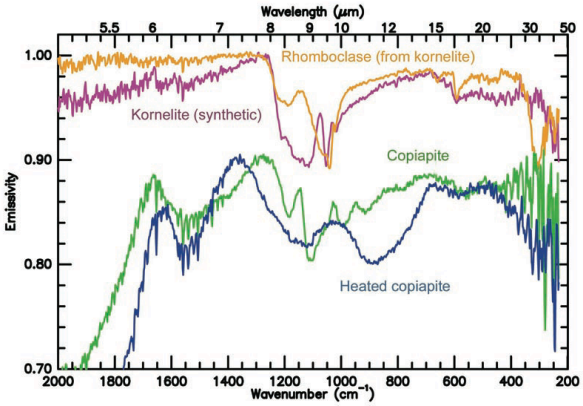

Figure 2. Thermal emissivity spectra of two samples that underwent change. The synthetic **kornelite** sample dehydrated under ambient conditions and altered to rhomboclase. The **copiapite** sample underwent stepwise heating to 300 °C.

Sulfides: Sulfide minerals are common in promitive Interplanetary Dust Particles [e.g., 7] and meteorites (and were detected in Comet Halley) [e.g., 8]. Sulfides likely occur throughout the solar system (e.g., Io, Europa, Ganymede [9], etc.), including being common in terrestrial volcanic terrains as well as in "black smokers" seen by the sub, *Alvin*, at the East Pacific Rise.

The thermal emissivity spectra of 11 sulfides are shown in Figure 3. Sulfides generally are spectrally flat (graybody) at the higher frequencies (higher wavenumbers) but exhibit spectral structure longward of ~450 cm^{-1}. The sulfide features dominate each spectrum from 450 to 200 cm^{-1} region [10].

Five samples collected from the East Pacific Rise black smokers have been analyzed in thermal emission. The spectra (not shown) show evidence for a variety of sulfate minerals (including gypsum and anhydrite) as well as spectral evidence for sulfides. Specifically, chalcopyrite and pyrite were identified on the basis of their thermal emissivity spectra alone.

Because Mars had extensive volcanic activity, sulfides ought to be present. Additionally, the bright ferric-sulfate bearing soils of Paso Robles (Mars) may have originated from the oxidation of precursor volcanogenic sulfide deposits [e.g., 2,3] as seen in terrestrial environments [e.g., 5]. Other sulfates on Mars, as well, may be derived from precursor sulfide minerals [e.g., 6].

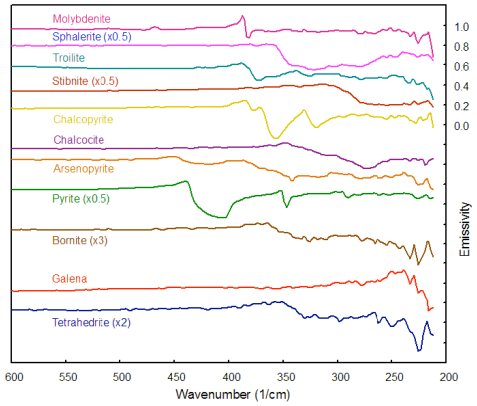

Figure 3: Thermal emissivity spectra of sulfide minerals over the 600 to 200 cm^{-1} region. Spectra are offset for clarity.

Conclusion: Sulfates and sulfides represent important minerals on the surface and in the interior of Mars (and are found in Martian meteorites). In order to identify these minerals in data sets returned from Mars, extensive laboratory analyses of well-characterized minerals must be conducted to produce high-quality thermal emission sample spectra for comparison. We will continue to study sulfate- and sulfide-suite minerals and apply our spectra to Martian data sets in order to better understand the environmental conditions on Mars, including oxidation, hydration, pH, etc. The sulfate and sulfide minerals studied here in the mid-infrared will be studied in a collaborative manner using visible-near infrared and Mössbauer techniques.

Acknowledgments: This work was supported by NASA's Mars Odyssey Participating Scientist and Mars Fundamental Research Programs. Thanks are extended to Phil Christensen for the use of his spectrometer lab.

References: [1] Johnson, J. R. et al. (2007) *GRL, 34,* L13202. [2] Lane, M. D. et al. (2008) *Am. Mineral., 90,* 728-739. [3] Yen, A. S. et al. (2008) *JGR, 113,* E06S10. [4] Bishop, J. L. et al. (2008) *AGU, 89(53),* P43B-1397. [5] Jambor, J. L. et al. (2000) *Rev. Mineral., 40,* 303-350. [6] Fernandez-Remolar, D. C. et al. (2007) *LPS XXXVIII,* Abst. 1580. [7] Rietmeijer, F. J. M. et al. (2002) *LPS XXXIII,* Abst. 1079. [8] Keller, L. P. et al. (2000) *LPS XXXI,* Abst. 1860. [9] Anderson, J. D. et al. (2003) *Phys. of the Earth and Planet. Inter., 136,* 201-213. [10] Gadsen, J. A. (1975) *Infrared Spectra of Minerals Related to Inor. Comp.,* Butterworths, Reading, MA, 277 pp.

THE IMPACT OF ASTRONOMICALLY INDUCED INSOLATION VARIATIONS ON THE EXTENT OF THE MARTIAN CRYOSPHERE

J. Lasue[1], S. Clifford[1].
1. Lunar and Planetary Institute, 3600 Bay Area Blvd, Houston, TX 77058 USA, lasue@lpi.usra.edu

Introduction: Estimates of the global inventory of water on Mars based on a determination of the amount of water required to erode the outflow channels suggest that a quantity equivalent to a global ocean 0.5 to 1 km deep may be stored in the planet's subsurface [1, 2]. As this inventory post dates the timing of the most efficient processes that may have lead to its removal, the majority of this water is expected to survive to the present day as subsurface ice and groundwater (e.g. [3, 4]).
In this work, we examine the impact of climatic insolation variations on the extent of the Martian cryosphere – with particular regard to the occurrence of thawing in both the deep- and near-subsurface that could promote hydrous alteration.
Recent calculations show that the globally averaged depth of the cryosphere of Mars may be twice as deep as previously estimated [5], although spatial heterogeneities in crustal heat flow, thermal conductivity, and freezing point depression may result in substantial local variations in cryosphere thickness about this mean.
Here we demonstrate that climatic variations in insolation may result in km-scale variations in cryosphere thickness at high latitudes over the past 20 million years. We also demonstrate that extensive thawing of the near-subsurface may occur at mid- to high-latitudes at time of high obliquity. Implications on the aqueous processes of the subsurface of Mars and on the presence of subpermafrost groundwater are examined.

Model description: the evolution of the Martian cryosphere with time is described by the refinement and extension of a one-dimensional finite difference thermal model [6]. Our recent revisions take into account the surface temperature variation due to astronomically induced variations in insolation, the temperature-dependent conductivity of rock and ice, the potential effect of the presence of methane hydrate, an exponential decline in porosity with depth and a potentially lower Martian geothermal heat flow.
The porosity of the subsurface of Mars is assumed to follow an exponential law as $\Phi(z) = \Phi(0)\exp\left(\frac{-z}{D}\right)$ where $\Phi(0)$ is the surface porosity, conservatively assumed to be 0.2, and D is the gravitationally scaled porosity decay constant of about 2.82 km for Mars [4]. The thermal conductivity of a mixture of porous basalt and ice is obtained with the geometric mixing rule. Finally, the numerical model has been adapted for the simulation of various layers of different thermal conductivity and porosity laws.

Surface insolation: Over the timescale considered, the diurnal variation of the insolation at a given latitude is not taken into account. A mean annual insolation value following the approximate function by Hoffert et al., [7] has been assumed.

$$S(l) \approx \left[\frac{S_0}{4\sqrt{1-e^2}}\right]\left(\frac{3}{2} - \frac{2\sin(i)}{\pi}\right) - \left(\frac{3}{2} - \frac{6\sin(i)}{\pi}\right)\sin^2(l)$$

with l the latitude considered for the calculations, S_0 the solar constant at the semi-major axis orbital distance, i, the obliquity of the planet, e, the eccentricity of the Martian orbit. The variations of the orbital parameters of Mars have been taken from the work of Laskar et al. [8]. The calculated insolation at the equator over the last 20 million years and for the next 10 million years is shown in Fig. 1. The polar caps are assumed to be stable over this time period with a mean albedo of 0.25 over the surface of Mars and an albedo of 0.65 where polar caps are present (latitude of about 70° or larger).

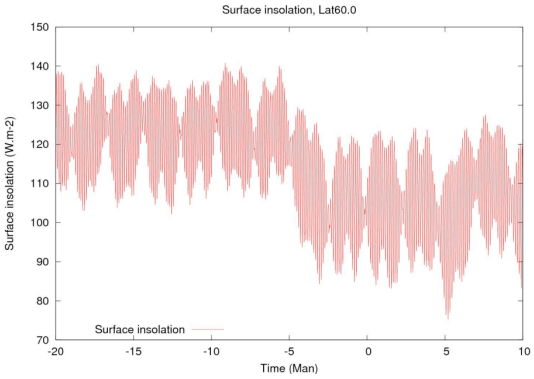

Figure 1: calculated insolation at the equator as a function of time over the last 20 million years and for the next 10 million years with the assumed obliquity and eccentricity variations of Laskar et al. [8].

Heat flow: The mean Martian crustal geothermal heat flow is assumed to vary between 15 and 45 mW.m^{-2} based on rheologic estimates of lithospheric thickness [9 – 11] with a higher probability for lower range of values (~8 – 25 mW.m^{-2}).
While these estimates are specific to regions like Tharsis [9 – 10] and the North polar plains [11], they suggest that the 'mean' global heat flow of Mars may have been overestimated by a factor of two – which, if true, would double the expected thickness of frozen ground.
Numerical simulations are presented here for a Martian crustal heat flow of 15 mW.m^{-2}.

Thermal conductivity: Except for the high latitude zones (above 40°) where there is evidence that water ice persists year-round at shallow depth (e.g. Boynton et al. [12]), the Martian subsurface is assumed to have a thermal structure consisting of several layers. Within the latitude range of ±40°, the diffusive instability of ground ice is expected to have led to the progressive desiccation of the regolith to a maximum equatorial depth that, for the purposes of this discussion, reaches a maximum of 180 m. The uppermost 5 m of this desiccated region is assumed to have a thermal conductivity of 0.05 W.m^{-1}.K^{-1} consistent with the thermal inertias measured by mini-TES [13] and characteristic of a high-porosity granular material. Underlying this initial surface layer is a second layer of basalt or cemented sedimentary rock that is assumed to have an ice-free thermal conductivity of 0.1 W.m^{-1}.K^{-1}. Where ice is stable in the subsurface (at latitudes >40°, and at depths below the sublimation front at latitudes <40°) the thermal conductivity of both ice and rock is

given by the temperature-dependent expression $K = \frac{488.19}{T} + 0.4685$ where K is the thermal conductivity and T the temperature [14]. Finally, the methane recently detected in the Martian atmosphere [15 - 17] could originate from the cryosphere where it would be a major component. In its pure state, the thermal conductivity of gas hydrate is about 0.5 $W.m^{-1}.K^{-1}$ [18].

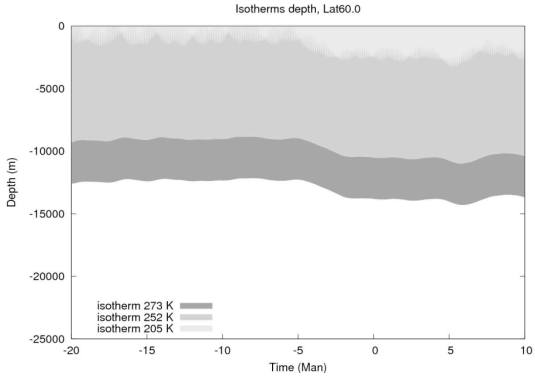

Figure 2: Evolution of the depths for the isotherms of 205 K, 252 K and 273 K over 30 million years for a heat flow of 15 mW.m-2.

Results: Fig. 2 shows that over millions of years, the astronomically induced variation of insolation can modify the position of the cryosphere base over more than 2 km. The depths of the isotherms at 205 K, 252 K and 273 K, corresponding respectively to the freezing-point boundaries of salt saturated ice (e.g. perchlorates seen by Phoenix), of chloride saturated ice (e.g. Na-Cl seen by Viking) and of pure water ice are presented. The mean depths of the isotherms over 30 Man as a function of the latitude is shown in Fig. 3.

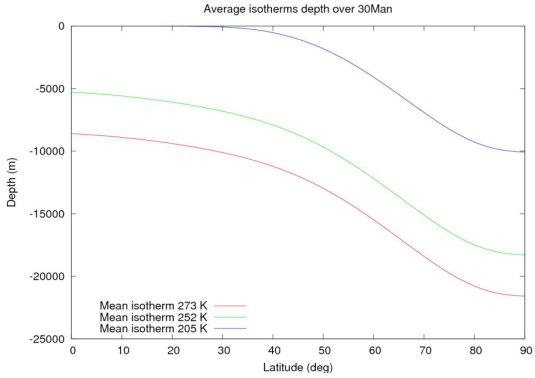

Figure 3: Mean depths for the isotherms of 205 K, 252 K and 273 K over the 30 million years for a heat flow of 15 mW.m-2 as a function of the latitude.

Simulations using gas hydrate instead of water ice as the main component of the cryosphere show that the expected depth of the cryosphere base is higher by more than 1.1 km due to its lower thermal conductivity as shown in Fig. 4.

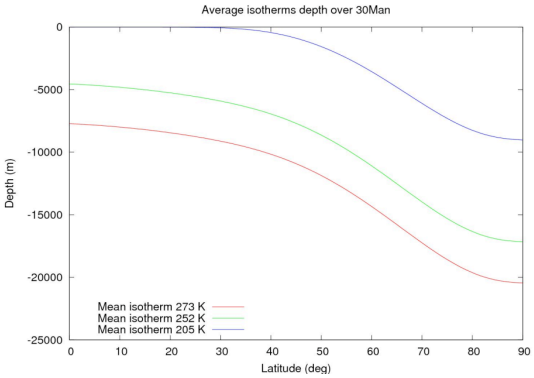

Figure 4: Mean depths for the isotherms of 205 K, 252 K and 273 K for the gas hydrates icy material over the 30 million years for a heat flow of 15 mW.m-2 as a function of the latitude.

Conclusions and Implications: Based on these revised estimates of heat flow, thermal conductivity, porosity and freezing-point depression isotherms, we have calculated that the effects of the astronomically induced variations in insolation are significant – resulting in km-scale variations in the depth of the cryosphere at high latitude. The presence of gas hydrates can reduce the thickness of the cryosphere by a similar amount. The most important parameter is the estimation of the Martian geothermal heat flow.

The averaged thickness of the cryosphere on Mars is likely to exceed 7 km at the equator and 20 km near the poles. However, variations in crustal heat flow, thermal conductivity and porosity may result in significant departures from these predicted values.

Moreover, the large variations in insolation over time can result in extensive thawing of the near-subsurface, for example above 60º latitude, promoting hydrous alterations of the near-surface.

Considerations of the evolution of the cryosphere over larger periods of time may have important implications for the occurrence of aqueous processes in both the near- and deep-subsurface – a potential that will be discussed in greater details at the meeting.

References: [1] Carr M. H. (1986) Icarus, 68, 187-216. [2] Carr M. H. (1996) Water on Mars, Oxford University Press. [3] Clifford S. M. (1993) JGR 98, 10973-11016. [4] Clifford S. M. and Parker T. J. (2001) Icarus, 154, 40-79. [5] Clifford S.M. et al. (2009) LPS XL, 2557. [6] Clifford S.M. and Bartels C.J. (1986) LPS XVII, 142. [7] Hoffert M.I. et al. (1981) Icarus, 47, 112-129. [8] Laskar J. et al. (2004) Icarus, 170, 343-364. [9] Solomon S. C. and Head J. W. (1990) JGR, 95, 11073-11083. [10] McGovern P. J. et al. (2004) JGR, 109, E07007. [11] Phillips R. J. et al. (2008) Science, doi: 10.1126/science.1157546. [12] Boynton W.V. et al. (2002) Science, 297, 81-85 [13] Fergason R.L. et al. (2006) JGR, 111, E02S21. [14] Hobbs P.V. (1974) Ice Physics, Oxford University Press. [15] Formisano V. et al. (2004) Science, 306, 1758-1761. [16] Krasnopolsky V. A. et al. (2004) Icarus, 172, 537-547. [17] Mumma M. J. et al. (2004) Bull. Am. Astron. Soc., 36, 1127. [18] Max M. D. and Clifford S. M. (2000) JGR, 105, 4165-4171.

A METEOROID "SUPER–VOLCANISM" ON THE EARTH AND MARS IN THE HADEAN EON. M.Lefort[1] and M.Maurette[2], [1]Institut Charles Sadron, BP 84047, 67034 Strasbourg, France, [1]CSNSM, Bat.108, 91405-Orsay, Campus, France. maurette@csnsm.in2p3.fr.

Introduction: Meteoroids with sizes ~100–200 µm represent the dominant mass fraction of the extraterrestrial material accreted by the Earth. Those that survive unmelted upon atmospheric entry can be recovered as micrometeorites in Antarctica ices and snows (AMMs). Their analysis show that ~99% of the meteoroids are related to the most volatile–rich meteorites, the hydrous carbonaceous chondrites, and dominantly to the CM chondrites. Upon atmospheric entry, each meteoroid produces a radar shooting star and a tiny "puff" of gases and smoke particles that feed a meteoroid "volcanism", rooted around the thermopause. The meteoroid origin of the Earth's atmosphere was already discussed [1, 2, 3]. In this abstract, we first outline the computation of the total amount of any meteoroid species accreted by the young Earth and Mars, since the merging of their last planetary embryo, at time, t_1. These computations are next exploited to decrypt the Hadean meteoroid sulfur cycle on both planets and its effects on their climates. In a companion abstract [4], we turn to Spirit and Opportunity to better constraint the origin of the thin contemporary Martian atmosphere**.**

A meteoroid accretion equation:

Earth: The self–erasing mega–impact by the last planetary embryo (about 10 lunar mass) did form the Moon at time, t_1, which corresponds to the formation age of the oldest lunar highland rocks (~4.44 Ga). It also simultaneously closed the formation time interval of the Earth and blew off its intractable pre-lunar atmosphere. Next, during the first ~100–200 Ma of the post-lunar period, meteoroids generated a new atmosphere. Their mass input rate was exponentially decaying with time, accordingly to the dimensionless relative lunar cratering rates, ***K(t)***, conjectured by Hartmann and subsequently improved by Neukum [5]. Indeed, one could expect that both the lunar impactors and the parent bodies of meteoroids were dominantly extracted from the same reservoirs of bodies. If the impactor number mass flux is ***K(t)***x higher than today, the meteoroid mass flux will be multiplied by the same factor (cf. Ref. 6, p. 273). In particular, the total amount, $\mathbf{M_A}$, of a given meteoroid species, **A**, delivered to the Earth scales as**:**

$$\mathbf{M_A} \sim [\mathbf{A}(\text{wt. \%}) \times 10^{-2}] \times \mathbf{\Phi_E}\,(t_1)\mathbf{.}$$

In this accretion formula, **A**(wt.%) and $\mathbf{\Phi_E}(t_1)$ are the wt. % concentration of a given species, **A**, measured in unmelted Antarctica micrometeorites, and the integrated mass flux of meteoroids since the formation of the Moon, at time, t_1 ~4.44 Ga, respectively. The major problem hiding in this simple formula is the value of $\mathbf{\Phi_E}(t_1)$, which was estimated with 3 totally independent methods [1, 2, 3]. The similarity (within a factor 2) of these 3 estimates validated using the "lunar" value, $\mathbf{\Phi_E}(t_1)$ ~5.6×10^{24} g, deduced from the integration of the ***K(t)*** curve**.**

Mars: The extrapolation to Mars required estimating the value of $\mathbf{\Phi_{Mars}}(t_1)$ ~10^{24}g, from $\mathbf{\Phi_E}(t_1)$, just considering**:** (**i**) the ratio of the gravitational focusing factors of the 2 planets with an updated meteoroid approach velocity, V_∞ ~20 km s^{-1}, corresponding to that expected for cometary debris (AMMs are very similar to the Wild 2 dust particles returned by Stardust)**;** (**ii**) the variation of the meteoroid flux between ~1 and 1.5 AU, which approximately scales inversely to the heliocentric distance (see Ref. 7, Fig. 42, from Eberhard Grün)**;** (**iii**) the timing of the first shot at t_1 ~4.44 Ga, like on Earth (see Introduction in Ref. 4)**.**

The meteoroid purity of the Earth's atmosphere: The accuracy of the meteoroid predictions is best constrained on the Earth. It can be characterized by a mass "misfit-ratio" (reported in bold–italics) between the predicted and observed amounts of a given species, **A**, in a selection of species that widely differ in both their chemical properties and concentrations in AMMs, and such as **:** Ne (***1.2***)**,** N_2 (***0.98***)**,** H_2O (***0.40***)**,** CO_2 (***1.55***)**,** S (***1.24***), Ir (***1.06***), Os (***0.89***) and Ru (***1.03***). The worst fit was observed for H_2O. One of the major finding was the impressive fits observed for S, Ir, Os and Ru, when the predicted amounts are compared to the corresponding total amounts hosted in the constituent sulfides of upper mantle rocks [2]. Therefore, the total mass of sulfur in the upper mantle would well corresponds to that released as SO_2 from meteoroid sulfide (troilite) upon atmospheric entry. We likely hold the initial (meteoroid troilite) and final (Fe_2S in the upper mantle) stages of the early meteoroid sulfur cycle on the Earth. We next try to identify its intermediate stages, and in Ref. 4, we question how the missing plate tectonics affected the sulfur cycle on Mars**.**

From H_2SO_4 vapor to droplets of acid–sulfate aerosols: Like in any classical basalt magma volcanic eruption, the oxidation of meteoroid sulfide into SO_2 can be attributed to a kind of in–situ oxidation, which is related to the oxygen fugacity of their assemblage of minerals that mostly depend on their anhydrous silicates and iron contents. About 30 years ago, Hofmann and Rosen [8] noted: *"The formation mechanism of stratospheric H_2SO_4 vapor, which is postulated to be a precursor of stratospheric aerosols, is not known. It has been conjectured to be formed in the stratosphere from the reaction of water and SO_3, the latter being derived from the oxidation of SO_2"***.** This concise statement is still valid, even though the formation and evolution of volcanic species in the early Earth atmosphere are now described with commercial softwares with up to 214 reactions (including about 40 S–rich species) in both chemistry and the complex microphysics of the condensation of H_2SO_4 vapor into dirty acid droplets [9]. We skipped this intimidating reaction network, just relying on experimental studies of these aerosols for 3 modern eruptions that ejected material into the stratosphere (Agung, El-Chichon and Pinatubo). Both instruments on space probes and analyses of the acid aerosol fallouts in polar snows, led to 3 important observations**:** (**i**) sulfate aerosols are formed in ~2–3 weeks after injection of SO_2 in the stratosphere**;** (**ii**) their lifetimes against gravitational settling on Earth is ~4–5 year**;** (**iii**) they reflect sunlight back to space and cool the Earth**.**

Heavy weathering of early sialic crusts: The enormous mass input rates of meteoroid SO_2, H_2O and CO_2 were about similar**,** during the first ~100 Ma of the post-lunar meteoroid. They reached values of ~4,000 Mt yr^{-1} and ~800

Mt yr^{-1} for the Earth and Mars, respectively. About 2/3 of the meteoroid water, as well as meteoroid "smoke" particles, were likely involved in the formation of sulfate aerosols. They did quickly rain on the Earth and Mars as dirty liquid droplets and/or hail stones, while being constantly generated by the exponentially decaying input rates of SO_2 and H_2O, during the first 100–200 Ma of the post-lunar period**.**

The next effect of this acrid rain (pH ~0), on both planets, was a very heavy acidic weathering of a thin sialic crust, which was a prerequisite to the formation of old (≥ 4.3 Ga) Australian zircons [10]. It also prevented the scavenging of CO_2 in carbonates. However, the fates of these initial loads of aerosols subsequently diverged on the two planets, as plate tectonics was "missing" on Mars. On the Earth, a fast "platelet" tectonics [11] was likely driving a massive attack of the oceanic crust by strongly acidic water. This generated a world wide hydrothermal system, where sulfates were likely transformed into iron sulfides and subducted to the upper mantle (see 3rd section). What were the implications of these earlier similar stages of the meteoroid sulfur cycle on both planets ?

A benign Hadean climate back to 4.3 Ga ago: Climatic models attempted to fabricate the mild climatic conditions required for the birth of life on Earth, around 4 Ga ago. These mild conditions have now been established from the oxygen isotopic composition, the lithium concentration and the U–Pb age of a few old Australian zircons with ages ~4.3 Ga [10]. These models rely on the reduced luminosity of the "faint" early Sun (by a factor ~30%), which would have frozen the oceans of both Mars and the Earth. With adjustable parameters any model can rightly counterbalance this cooling with greenhouse gases (CO_2 **,** H_2O, and CH_4) outgassed from the Earth. They ignored both the early roles of SO_2 and the Moon forming impact, which blew off the prelunar greenhouse gases at a time when the young Earth was almost fully degassed. This left a niche for a meteoroid "super–volcanism", which probably dominated the climatic effects of the faint residual volcanism expected from the strongly degassed upper mantle.

The problem worsened in 2002 with the high S contents (~5%) measured in AMMs [12]. The accretion equation predicts the formation of huge input rates of sulfate aerosols droplets at high elevation, on the Earth, Mars and Venus. They reflected sunlight back to space and cooled the Earth, thus *enhancing the cooling effect of the faint early Sun*! This effect is well established for the most explosive volcanic eruptions that inject material in the stratosphere, such as Pinatubo (1991), Tambora (1815) and the Toba super–eruption (74,000 yr ago), which outgassed ~1000–5000 Mt of SO_2 in about 2 weeks. It triggered a *"volcanic winter"* that likely decreased the global temperature by ~4–5°C for a few years [13]. This Toba aerosol burden is rather similar to the corresponding expected meteoroid value (~4000 Mt yr^{-1}) on Earth, which was effective for ~100 Ma.

How did the Earth and Mars manage to avoid a ~200 Ma long volcanic winter that runs against the mild climate encrypted in the old Australian zircons, which requires the existence of liquid water and continents back to ~4.3 Ga ago? Indeed, the Toba aerosols alone would have attenuated solar light by ~10^5x ! Some processes had to heat up the kind of giant cocoon of "smoke" particles, aerosols and gases generated by the meteoroid volcanism. They possibly included**:** (**i**) the frictional heating of air molecules against the leading edge of meteoroids upon atmospheric entry that released about 130-6400 erg cm^{-2} s^{-1} (see Ref. 7, p. 270)**;** (**ii**) the latent heat of condensation of hot water vapor (released by shooting stars) into ice (≥ 2800 joules g^{-1})**;** (**iii**) the formation of strongly acidic oceans that prevented the scavenging of CO_2 into carbonate. The resulting increase of the CO_2 partial pressure could trigger a strong greenhouse effect on both the Earth and Mars.

But on the Earth this effect was limited, as the total burden of meteoroid CO_2 was found to be fully stored as carbonates in the crust. This is likely related to plate tectonics that shielded sulfur at great depths in the Earth's upper mantle (see 3rd section). The pH of ocean water could increase up to the critical value (~6) where CO_2 starts precipitating as carbonates. Simultaneously, the meteoroid delivery of SO_2 and CO_2 was sharply decaying by a factor ~100x during the first 200 Ma of the post-lunar period. However, on Mars, the missing plate tectonics could just allow a massive impregnation of the porous megaregolith with low pH waters [4], which permanently prevented the scavenging of CO_2 into carbonates. Therefore, CO_2 accumulated in the Martian "air", ready to be blown off at t_2 , like Ne and N_2**.** Then, a frozen and red planet was born**.**

Summary: The complementary works described in our two companion abstracts involve a classical scenario of planetary evolution, which is rooted in the pioneering work of George Wetherill in the 1970's. The first "*shot*" blew off, at about the same time, the intractable early atmosphere of Earth and Mars. Both planets were then immersed in the debris disk of the Sun, where the dominant debris were hydrous carbonaceous meteoroids similar to contemporary AMMs. Early Earth's processes had to be finely tuned in time, as to deliver the right amounts of such vastly different species as Ne, H_2O and Ir (e.g., the concentration of Ne is about 10^8x smaller than that of H_2O). They had also to fully recycle meteoroid sulfur into the Earth's upper mantle. In our companion abstract [4], we further extend the Martian part of this investigation, with the help of Spirit and Opportunity, as to get clues about the effects of missing plate tectonics on the early atmosphere of the terrestrial planets.

Acknowledgments: One of us (M.M) thanks IN2P3 for constant support.

References: [1] Maurette M. (2006) In *Comets and the Origin and Evolution of Life*, eds P.J.Thomas et al (Springer-Verlag), 69. [2] Maurette M. (2009) *ASP Conf. Series*, in press. [3] Maurette M. et al. (2006) *Adv. Space Res,. 38*, 701. [4] Maurette M. & Lefort M. (2009) This issue. [5] Hartmann W.K. (2003) *Meteorit. & Planet Sci., 338*, 579; [6] Maurette M. (2000) *ASP Conf. Series, 213*, 262. [7] Maurette M. (2006) *Micrometeorites and the mysteries of our origins* (Springer-Berlin), p. 1-330. [8] Hofmann D.J. & Rosen J.M. (1980) *J. Atmos. Scien., 38*, 168. [9] Martin R.S. et al. (2007) *Geochim. Cosmochim. Acta, 71*, 3673**.** [10] Ushikubo, T. et al. (2008) *EPSL, 272*, 666. [11] Ernst W.G. (2008) Gondwana Res., in press. [12] Duprat, J. et al. (2007) *Adv. Space Res., 39*, 605. [13] Rampino M.R. & Self S. (1992) *Nature, 359*, 50.

FREZCHEM: A GEOCHEMICAL MODEL FOR COLD AQUEOUS SOLUTIONS. Giles M. Marion[1]. [1]Desert Research Institute, 2215 Raggio Parkway, Reno, NV 89512, giles.marion@dri.edu.

Introduction: FREZCHEM is an equilibrium chemical thermodynamic model parameterized for concentrated electrolyte solutions (to ionic strengths > 20 m) using the Pitzer approach [1-2] for the temperature range from <–70 to 25°C, and the pressure range from 1 to 1000 bars [3]. The current version of the model is parameterized for the Na-K-Mg-Ca-Fe(II)-Fe(III)-Al-H-Cl-ClO_4-Br-SO_4-NO_3-OH-HCO_3-CO_3-CO_2-O_2-CH_4-Si-H_2O system and includes 100 solid phases including ice, chlorides, perchlorates, sulfates, carbonates, solid-phase acids, nitrates, acid-salts, iron oxides and hydroxides, aluminum hydroxides, silicon minerals, gas hydrates, and bromide sinks. The objectives of this presentation are to: (1) describe the Pitzer approach, (2) discuss model limitations, (3) describe user access to the FREZCHEM computer code, and (4) describe Mars applications.

Pitzer Approach: In the Pitzer approach [1-2], the activity coefficients (γ) as a function of temperature at 1.01 bar pressure for cations (M), anions (X), and neutral aqueous species (N), such as CO_2(aq) or CH_4(aq), are given by

$$\ln(\gamma_M) = z_M^2 F + \sum m_a(2B_{Ma} + ZC_{Ma}) + \sum m_c(2\Phi_{Mc} + \sum m_a \Psi_{Mca}) + \sum\sum m_a m_{a'} \Psi_{Maa'} + z_M \sum\sum m_c m_a C_{ca} + 2\sum m_n \lambda_{nM} + \sum\sum m_n m_a \zeta_{nMa}$$

$$\ln(\gamma_X) = z_X^2 F + \sum m_c(2B_{cX} + ZC_{cX}) + \sum m_a(2\Phi_{Xa} + \sum m_c \Psi_{cXa}) + \sum\sum m_c m_{c'} \Psi_{cc'X} + |z_X| \sum\sum m_c m_a C_{ca} + 2\sum m_n \lambda_{nX} + \sum\sum m_n m_c \zeta_{ncX}$$

$$\ln(\gamma_N) = \sum m_c(2\lambda_{Nc}) + \sum m_a(2\lambda_{Na}) + \sum\sum m_c m_a \zeta_{Nca}$$

where B, C, Φ, Ψ, λ and ζ are Pitzer-equation interaction parameters, m_i is the molal concentration, and F and Z are equation functions. In these equations, the Pitzer interaction parameters and the F function are temperature dependent. The subscripts c, a, and n refer to cations, anions, and neutral species, respectively. The activity of water (a_w) at 1.01 bar pressure is given by

$$a_w = \exp\left(\frac{-\phi \sum m_i}{55.50844}\right)$$

where ϕ is the osmotic coefficient, which is given by

$$(\phi - 1) = \frac{2}{\sum m_i}\left\{\frac{-A_\phi I^{3/2}}{1 + bI^{1/2}} + \sum\sum m_c m_a \left(B^{\phi}_{ca} + ZC_{ca}\right) + \sum\sum m_c m_{c'} \left(\Phi^{\phi}_{cc'} + \sum m_n \Psi_{nc'a}\right) + \sum\sum m_a m_{a'} \left(\Phi^{\phi}_{aa'} + \sum m_c \Psi_{caa'}\right) + \sum\sum m_n m_c \lambda_{nc} + \sum\sum m_n m_a \lambda_{na} + \sum\sum\sum m_n m_c m_a \zeta_{n,c,a}\right\}$$

FREZCHEM specifies the pressure dependence of equilibrium constants (K), activity coefficients (γ), and the activity of water (a_w). See [3-5] for a complete description of these temperature-pressure equations.

Parameterization of these Pitzer equations require experimental data. Figure 1 accurately depicts parameterized model calculations of equilibrium for magnesium perchlorate from 25°C to the eutectic at -68.6°C.

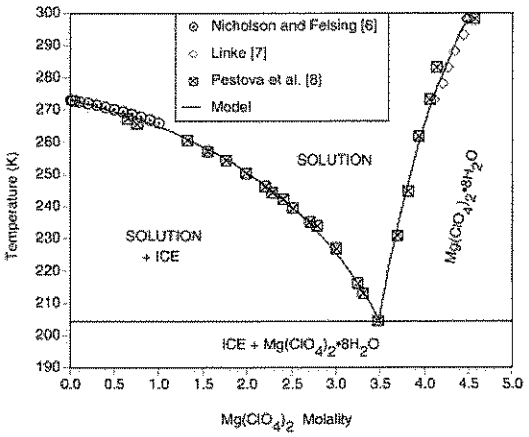

Figure 1. Equilibria for $Mg(ClO_4)_2$ solutions from 25°C to the eutectic.

Model Limitations: Limitations of FREZCHEM can be broadly grouped under Pitzer-equation parameterization, modeling (mathematics, convergence, and FORTRAN coding), and applications. One of the major limitations is the lack of key parameters and equilibrium relationships at subzero temperatures. This necessitates using surrogates as a replacement for the needed parameters. For example, the "ice" equilibrium line (Fig. 1) for $Fe_2(SO_4)_3$ in [5] used $Al_2(SO_4)_3$ data as a surrogate. Many solution phase equilibrium constants such as Henry's law constants for CO_2 and CH_4, first and second dissociation constants for carbonic acid, and the dissociation constant for water are all extrapolated to subzero temperatures [3]. There are two different mathematical algorithms based on a "sequential" approach that considers one reaction at a time (Marion algorithm) or a "Gibbs energy" approach that considers all chemical processes simultaneously (Mironenko algorithm) (Table 1). FREZCHEM assumes equilibrium(cannot cope with kinetics), despite numerous examples in natural environments of mineral supersaturation (e.g., calcite in seawater) and other disequilibria [5]. For a definitive review of model limitations, see [3].

Model Access: Table 1 summarizes the development from FREZCHEM1 in 1994 with 16 solid phases to FREZCHEM13(in preparation) with 100 solid phases. A listing of all existing chemistries will be handed out at the Workshop, which is important for potential users. Most of the components in Table 1 are self-explanatory except for "Other Factors." The Marion and Mironenko algorithms are mathematical approaches used in the model (see above). "Pressure" is when pressure beyond 1 atm was added to the

model, and later "gas hydrates" and the "INTERNET" version were created. Versions 5 to 12 have accessible listings of the FORTRAN computer code with instructions on how to use FREZCHEM, and an INTERNET version at the site: http://frezchem.dri.edu. For initial users, the INTERNET version is a good place to start because the convergence problems are minimized (Mironenko algorithm, Table 1), and that version is easy to use. Both this abstract and the presentation at the Workshop will only provide a brief overview of FREZCHEM. For a detailed description of all facets of FREZCHEM through Version 9, see the book on "Cold Aqueous Planetary Geochemistry with FRECHEM: From Modeling to the Search for Life at the Limits" [3].

Mars Applications: We applied FREZCHEM to simulate a hypothetical perchlorate-dominated chemistry from the Phoenix mission site [20]. Figure 2 shows how these chemistries would evolve during an evaporation. The first carbonate mineral to precipitate was hydromagnesite [$3MgCO_3 \cdot Mg(OH)_2 \cdot 3H_2O$] (Fig. 2). Later in the evaporation, gypsum ($CaSO_4 \cdot 2H_2O$) and the insoluble $KClO_4$ began to precipitate. pH began at 8.30, rose to 8.51, where hydromagnesite started to precipitate, and then slowly dropped to 7.78. At around 1 g of residual water, the hydrated magnesium sulfate salts ($\cdot 7H_2O$ = epsomite, $\cdot 6H_2O$ = hexahydrite, and $\cdot H_2O$ = kieserite) began precipitating, which caused a precipitous drop in SO_4 concentrations (Fig. 2). The next solid phase to precipitate was $Mg(ClO_4)_2 \cdot 8H_2O$ (Fig. 2), which led to a rapid decrease in Mg concentration. At the end of this evaporation simulation with only ≈ 0.1 g of water remaining, the aqueous system was dominated by Na, Cl, and ClO_4 (Fig. 2) that would eventually lead to precipitation of NaCl and $NaClO_4 \cdot H_2O$.

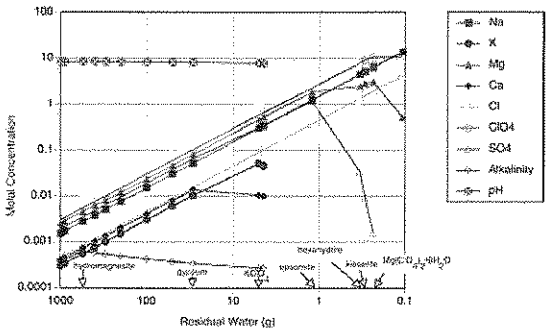

Figure 2. The molal concentrations of a Phoenix martian brine during evaporation at 25°C. Arrows indicate where solid phases start to precipitate.

Acknowledgments: We thank Lisa Wable for help preparing this abstract. Funding was provided by a series of NASA PG&G, MFR, and EPSCoR projects.

References: [1] Pitzer K.S. (1991) *Activity Coefficients in Electrolyte Solutions,* CRC Press. [2] Pitzer K.S. (1995) *Thermodynamics,* McGraw-Hill. [3] Marion G.M. and Kargel J.S. (2008) *Cold Aqueous Planetary Geochemistry with FREZCHEM,* Springer. [4] Marion G.M. et al. (2005) *Geochim. Cosmochim. Acta.* 69, 259-274. [5] Marion G.M. et al. (2008) *Geochim. Cosmochim. Acta.* 72, 242-266. [6] Nicholson D.E. and Felsing W.A. (1950) *J. Am. Chem. Soc.* 72, 4469-4471. [7] Linke W.F. (1965) *Inorganic and Metal Organic Compounds, Vol II,* Am. Chem. Soc. [8]Pestova O.N. et al. (2005) *Russ. J. Appl. Chem.* 78, 409-413. [9] Marion G.M. and Grant S.A. (1994) CRREL Spec. Rept. 94-18, USACRREL, Hanover, NH. [10] Mironenko M.V. et al. (1997) CRREL Spec. Rept. 97-5, USACRREL, Hanover, NH. [11] Marion G.M. and Farren R.E. (1999) *Geochim. Cosmochim. Acta.* 63, 1305-1318. [12] Marion G.M. (2001) *Geochim. Cosmochim. Acta.* 65, 1883-1896. [13] Marion G.M. (2002) *Geochim. Cosmochim. Acta.* 66, 2499-2516. [14] Marion G.M. et al. (2003) *Geochim. Cosmochim. Acta.* 67, 4251-4266. [15] Marion G.M. et al. (2006) *CALPHAD.* 30, 248-259. [16] Marion G.M. et al. (in resubmission) *Computers & Geosciences.* [17] Marion G.M. et al. (in press) *Geochim. Cosmochim. Acta.* [18] Marion G.M. (2009) *Icarus* 200, 4362-445. [19] Marion G.M. et al. (in preparation) *Icarus.* [20] Marion G.M. et al. (2009) LPSC XL, Abstract #1959.

Table 1. An overview of various versions of the FREZCHEM model.

Version	Cations	Anions	Other Factors	Solid Phases	References
1	Na-K-Mg-Ca	Cl-SO_4	Marion algorithm	16	Marion and Grant, 1994[9]
2	Na-K-Mg-Ca	Cl-SO_4	Mironenko algorithm	16	Mironenko et al., 1997[10]
3-4	Na-K-Mg-Ca	Cl-SO_4-HCO_3	Marion algorithm	21	Marion and Farren, 1999[11]
5	Na-K-Mg-Ca	Cl-SO_4-HCO_3	Marion algorithm	35	Marion, 2001[12]
6	Na-K-Mg-Ca-H	Cl-SO_4-HCO_3 -NO_3	Marion algorithm	50	Marion, 2002[13]
7	Na-K-Mg-Ca-H -Fe(II)	Cl-SO_4-HCO_3 -NO_3	Marion algorithm	56	Marion et al., 2003[14]
8	Na-K-Mg-Ca-H -Fe(II)	Cl-SO_4-HCO_3 -NO_3	Marion algorithm, Pressure	56	Marion et al., 2005[4]
9	Na-K-Mg-Ca-H -Fe(II)	Cl-SO_4-HCO_3 -NO_3	Marion algorithm, Pressure, Gas hydrates	58	Marion et al., 2006[15]
10	Na-K-Mg-Ca-H -Fe(II)	Cl-SO_4-HCO_3 -NO_3	Mironenko algorithm, Pressure, Gas hydrates, INTERNET	58	Marion et al., in resubmis. [16] http://frezchem.dri.edu
11	Na-K-Mg-Ca-H -Fe(II)-Fe(III)	Cl-SO_4-HCO_3 -NO_3	Marion algorithm, Pressure, Gas hydrates	81	Marion et al., 2008[5]
12	Na-K-Mg-Ca-H -Fe(II)-Fe(III)-Al	Cl-SO_4-HCO_3 NO_3-Si-Br	Marion algorithm, Pressure, Gas hydrates	95	Marion et al., in press[17] Marion et al., 2009 [18]
13	Na-K-Mg-Ca-H -Fe(II)-Fe(III)-Al	Cl-SO_4-HCO_3 -NO_3-Si-Br-ClO_4	Marion algorithm, Pressure, Gas hydrates	100	Marion et al., in prep.[19]

FORMATION AND IMPACT "MATURATION" OF THE EARLY ACRID METEOROID ATMOSPHERE OF MARS. M.Maurette[1] and M.Lefort[2], [1]CSNSM, Bâtiment 104, 91406 Orsay-Campus, France, [2]Institut Charles Sadron, BP 84047, 67034 Strasbourg, France. maurette@csnsm.in2p3.fr.

Introduction: In a previous paper on the formation of the Martian atmosphere [1], we already extrapolated to Mars the meteoroid accretion scenario proposed for the Earth, and which is outlined in a companion abstract [2]. It involves a first "shot", i.e., the mega–impact of the last planetary embryo to merge the terrestrial planets at about the same time, t_1 [3]. Therefore, it can be approximated by the age of the oldest lunar rocks (~4.44 Ga) that date the formation of the Moon. It blew off the complex intractable "pre-first-shot" Martian atmosphere. Then, meteoroid volatiles that got released upon atmospheric entry could accumulate until a second mega–impact, at time t_2 ~4.1 Ga, blew them off again. This allowed the accretion of the thin contemporary Martian atmosphere. The recent discovery of hidden mega–impact basins on Mars [4] might support this "2–shots" scenario.

2004: Two "shots" in the Hadean Eon: The composition of a pure meteoroid atmosphere can be expressed in terms of the mass mixing ratio of a given species, **A,** relatively to that of N_2, and such as Ne, H_2O, and C and S that generate CO_2 and SO_2 upon atmospheric entry [2]. It scales as the corresponding concentration ratio measured in unmelted micrometeorites collected in central Antarctica, i.e., Ne/N_2 ~2 x 10^{-5} and H_2O/N_2 ~CO_2/N_2 ~SO_2/N_2 ~130–140. The measured CO_2/N_2 ratios in the atmospheres of the Earth, Mars and Venus are similar to the meteoroid ratio within a factor 2 (Table 1.1, in Ref.5). This suggests a meteoroid origin of their atmospheres.

The total amount, $\mathbf{M_A}(t_1)$, of a meteoroid species, **A**, delivered to Mars since t_1, scales as the product of the concentration of **A** in AMMs, by the integrated meteoroid mass flux accreted by Mars since t_1 , $\mathbf{\Phi_M}(t_1)$ ~10^{24} g [2]. Meteoroids delivered ~99% of the Martian atmosphere during the first 200 Ma of the "post-first-shot" period, respectively, when the partial pressures of N_2, H_2O, CO_2 and SO_2 did reach about *0.3*, *70*, *26* and *19* bars, respectively (i.e., assuming no loss of species). A second shot blew off this thick atmosphere at t_2 ~4.1 Ga, when the amplification of the meteoroid mass flux, relatively to the present day flux, dropped to ~800x, as to build up the contemporary partial pressure of CO_2 of about 7–8 mbar (this amplification is discussed in Ref. 2). In 2004, at the time of submission of this paper, there was no visible remnant of these shots!

June 2008: the combination of altimetry and gravimetry reveals the hidden shots: The situation quickly changed in June 2008 [4], when the combination of altimetry (with the MOLA instrument) and gravity revealed the contour of a ~10,000 km wide buried mega-impact basin (Borealis), which covers about ¼ of the Martian surface. Impact models suggested that the impactor was a Pluto sized body (~2300 km wide). At least, the first shot became visible! The discovery of this buried basin reactivated the interest for previous works on giant impacts, which already showed that some large smooth Martian plains turned to be buried impact basins, such as Utopia and Ares (about (~3400 km and 3300 km wide, respectively). But their parent impactors could hardly blow off the Martian atmosphere.

However, about 4 Ga ago, a round of 5 successive giant impacts, likely resulted from the tidal disruption of a ~1000 km size asteroid that was approaching Mars in the ecliptic plane [6]. The corresponding giant impact basins include: (**i**) Hellas and Argire (about 2100 km and 1800 km wide, respectively), both visible in the Southern hemisphere; (**ii**) Isidis, Utopia and Thaumassia (about 1500 km, 3000 km and 600 km wide, respectively), which are still buried under sediments. Each one of these impacts could not blow off the thick Martian atmosphere. However, Genda and Abee [7] showed that the existence of an ocean greatly eases gravitational escape during impact. Firing quickly 4 other successive shots in the already vaporized Martian oceans might have acted as a decisive second shot. But the young age (~3.6 Ga) of the Isiris basin still poses problem.

Extrapolation of the Earth sulfur cycle to Mars: The two first stages of the meteoroid S–cycle were similar on the Earth and Mars (cf. Ref. 2). The hydrous silicates and iron sulfides of meteoroids were likely "geochemically engineered" upon atmospheric entry as follow: (**i**) The giant meteoroid burdens of SO_2 and H_2O (about 800 Mt/yr during 100 Ma on Mars) led to the formation of droplets of acid–sulfate aerosols, which contributed to further cool both planets during the period of faint early Sun; (**ii**) After gravitationally settling they formed highly acidic oceans, which prevented the scavenging of CO_2 as carbonates, and thus enhanced its greenhouse effect.

On the Earth sulfur was gradually scavenged though subduction to the upper mantle (cf. 3rd section in Ref. 2). The pH of the residual water could increase up to the critical value of ~6, beyond which CO_2 started to react to form carbonates and gradually controlled a benign climate. However, on Mars, subduction was "missing" as to shield sulfur at great depths, and the S-cycle was confined within the megaregolith. Hopefully, the Martian Rovers and instruments on board of several space missions might yield new clues about this megaregolith stage specific to the Martian S–cycle.

Constraints from Spirit and Opportunity:

Spirit: At Gusev crater [8], Spirit measured elemental enrichments and/or depletions of 16 elements in the Martian soils, relatively to local rocks (RATs) that were abraded with the "Rock Abrasion Tool". Any meteoroid contribution should be hopefully spotted among the 9 elements (Na, Si, P, S, Cl, K, Ti, Ni, Zn) showing an enrichment in the soils, and not a depletion (Mg, Al, Ca, Cr, Mn, Fe, Br). Sulfur showed the greatest enrichment in all soils. This gave a strong hint about a meteoroid chondritic contamination, as sulfur is about 3 times more abundant in micrometeorites (~5 wt.%) than in the set of 5 abraded Martian rocks from the Gusev crater (~1.6 wt.%). The expected meteoroid sulfur concentration was estimated with the accretion equation (cf. Ref. 2). The missing plate tectonics probably led to the "reactive" storage of the initial meteoroid sulfate aerosols in the porosity of the Martian megaregolith. This acrid regolith also prevented the formation of carbonates, thus forcing CO_2 to accumulate in the "air", getting ready for a second blow-off.

This porosity is characterized by a depth decay constant (e-folding depth), **τ** ~2.8 km [9]. Let us assume a ~100 % retention of these trapped sulfate aerosols during the second shot, up to a depth ~2**τ**, while all volatiles still in the "air" (noble gases, N_2, CO_2 and probably a minor fraction of water not bound to sulfate aerosols), were fully blew off at t_2 ~4.1 Ga. The total burden of meteoroid sulfur delivered after the first shot, yields a bulk sulfur concentration of the megaregolith of ~4.3–2.3 wt.%, for a regolith density of about 1–3 gm cm^{-3}, respectively. This value, which drops to ~2.6–1.5 wt.% for a regolith retentive depth of ~3**τ**, well fit the average S–excess (~1.9 wt.%) found in the soils. This would imply that ~40% of the Gusev soils are made of a CM-type chondritic component. However, they contain too much Al, Cl, K, Ca, Ti, and not enough Mg, Fe and Ni.

C.Engrand and collaborators showed that the elemental composition of micrometeorites collected in Central Antarctica, and defined with 13 elements (Na, Mg, Al, Si, P, S, K, Ca, Ti, Cr, Mn, Fe and Ni), closely matches that of the CM-type chondrites (see Fig. 47, in Ref. 10). For the 3 additional elements detected in the Martian soils (Cl, Br and Zn) we thus used the CM concentrations in the computations. For each element, we estimated a meteoroid "misfit–ratio" (MMR), next reported in bold *italics*, just rationing the predicted meteoroid concentration in the bulk megaregolith to the excess concentration measured in the soils, on the surface of Gusev crater (i.e., the difference between the average concentrations measured in the soils and RATs, respectively). For a ratio of 1 the measured value exactly matches the meteoroid contribution. A dominant meteoroid contribution is observed for Na (***1.3***), P (***1.1***), S (***1.9***), and Zn (***1.1***). Indeed, a misfit-ratio ≤ ***2*** corresponds to a "good" accuracy when moving so far back in time, with elements that differ so much in chemical properties and concentrations. However, large misfits are observed for Cl (***0.1***), K (***0.16***), and Ti (***0.34***), whereas Ni (***38***) shows the highest MMR**.**

Opportunity: At Meridiani Planum [11], excess concentrations are observed for Na (***1.0***), Al (***0.72***), Si (***3.62***), Cl (***0.58***), Ca (***1.04***), Ti (***0.33***), Cr (***1.95***) and Fe (***5***). However, S, P and Zn, which gave the right excess concentrations at Gusev Crater, as well as Ni (***38***), are now depleted at MP! This probably reflects the higher concentrations of these elements in the local RATs. It is thus quite puzzling to note that the bulk average sulfur content of the MP–soils even better fit the meteoroid prediction (MMR= ***1.50***). Sodium is the only winner, yet, in this confrontation to get the best MMR at both Gusev Crater and Meridiani Planum. The erratic soil elemental depletions and/or excesses observed at the two sites still masquerade the chondritic component**.**

Previous scenarios: The Martian atmosphere would mostly result from a classical basalt magma volcanism. In a consensual scenario [12, 13], about 1 bar of SO_2, altogether with "abundant" water and CO_2, were released in ~100 Ma, about 4 Ga ago, during the formation of the giant volcanoes of the Tharsis bulge (assimilated to Hawaiian volcanoes). As SO_2 had a long lifetime in the presence of CO_2, it was the dominant greenhouse gas to warm the Martian atmosphere. Like on Earth, SO_2 generated sulfate aerosols that gravitationally settled to the Martian surface, thus inhibiting the formation of carbonates. This both explains the puzzle of the missing carbonates and offers the strong CO_2 greenhouse effect required to generate at least a few bars of running water. The meteoroid volcanism is much different from the TBV with regard to**:** (**i**) stressing the role of the early heavy bombardment**;** (**ii**) "erupting" from the initial short-lived hot volumes of ~10 km-long shooting stars clustering around the mesopause, and not from basalt magmas**;** (**iii**) its much earlier occurrence**;** (**iv**) a ~30x larger burden of volatiles species delivered during the first 100 Ma of the post-first-shot period, which is required to get *"at least 30–40 bars of water"* [14] to carve the fluviatile features**.**

Summary: The presumed role of the TBV sulfur cycle on Mars climate [12, 13] was enthusiastically commented by Maria Zuber in MIT news (12/27/2008)**.** She concluded**:** "*It is fascinating to think about whether this process may have played a role in the evolution of the early Earth*"**.** Both the meteoroid and basalt magma volcanisms are much better constrained on the Earth than on Mars. Meteoroid volcanism did well work on Earth [1, 2, 10]**.** Moreover, its extrapolation to Mars with the 2–shots scenario did rightly predict both**:** (**i**) the partial pressures of N_2 and CO_2 **;** (**ii**) the concentrations of Na, P, S and Zn observed in the excess concentrations found in Gusev crater soils**;** (**iii**) the missing carbonates**;** (**iv**) the right amount of water to carve fluviatile features**.**

The odd survival through Mars history of the predicted meteoroid burdens of some elements at Gusev crater adds to the fascinating mysteries of the red planet**.** Martian Rovers might help analyzing other sites looking at both Na, S and Ni. Another prospect is to predict the concentration of meteoroid elements that accumulated in the thin regolith (lunar mare type), that formed by impact gardening on top of the megaregolith, since the 2nd shot. During this period, the large amount of water that was stored in the megaregolith since t_1 got probably frozen due to the loss of the CO_2 greenhouse effect during the second shot. The new meteoroid species possibly got only distributed in the top layer of the thin regolith that was penetrated by the solar thermal wave.

Acknowledgments: One of us (M.M.) thanks IN2P3 for constant support**.**

References: [1] Maurette M. et al. (2006) *Adv. Space Res. 38*, 70**.** [2] Lefort M. & Maurette M. (2009) this meeting**.** [3] Canup R. and Agnor, C.B. (2000). In *Origin of the Moon and Earth*, Univ. Arizona Press, Tucson, 113**.** [4] Nimmo, F. et al. (2008) *Nature, 453*, 1220**.** [5] Owen T. (1999) In *The Molecular Origin of life*, Cambridge Univ. Press, Cambridge, 13**.** [6] Akamari-Hamed J. (2005) *JGR, 110*, E040**.** [7] Genda H. and Abee Y. (2005) *Nature, 453*, 842**.** [8] Gellert R. et al (2004) *Science, 305*, 829**.** [9] Squires S.W. et al. (1992) In, *Mars*, Univ. Arizona Press, Tucson, 523. [10] Maurette M. (2006) *Micrometeorites and the mysteries of our origins*, Springer-Verlag, Berlin, p. 1-330**.** [11] Rieder R. et al (2004) *Science, 306*, 1746. [12] Levine J.S. and Summers M.E. (2008) *Mars atmosphere: modelling and observations*, Abstract #9016. [13] Halevy I. et al. (2007) *Science, 318*, 1903**.** [14] Baker V.R. et al. (1992) In, *Mars*, Univ. Arizona Press, Tucson, 517**.**

EFFECT OF TEMPERATURE ON SILICA FORMATION DURING ACID-BASALT ALTERATION: CHEMICAL EQUILIBRIUM CONSTRAINTS. A. C. McAdam[1], M. Yu. Zolotov[2], M. V. Mironenko[3], and T. G. Sharp[2], [1]Atmospheric Experiments Laboratory, Code 699, Goddard Space Flight Center, Greenbelt, MD 20771, Amy.McAdam-1@nasa.gov, [2]School of Earth & Space Exploration, Arizona State University, Tempe, AZ 85287-1404, Amy.McAdam-1@nasa.gov, [3]Vernadsky Institute of Geochemistry & Analytical Chemistry, Russian Academy of Sciences, 19 Kosygin Str., Moscow 119991, Russia.

Introduction: The presence of silica and/or silica-rich minerals on Mars is consistent with in-situ data [e.g., 1, 2] and with orbital thermal infrared [e.g., 3, 4] and near infrared [e.g., 5] spectral observations of surface regions. Recently, the Spirit rover investigated silica-rich outcrops and soil (up to ~98 wt % SiO_2) at the Columbia Hills in Gusev crater [6]. These samples commonly have significant Ti abundances (up to 1.5 wt %) [6] and are probably opaline silica [7]. Although the silica is likely a result of aqueous processes [6-8], the conditions of rock alteration and silica deposition remain to be constrained. In [8], we show that the silica-rich deposits could form through low-temperature (*T*) alteration of martian rocks. The deposits have also been interpreted to have formed under hydrothermal conditions [e.g., 6, 7]. Here, we used thermochemical equilibrium calculations to investigate the conditions under which silica-dominated deposits may have formed at higher *T*. Potential additional constraints afforded by the presence of significant Ti in the deposits was also studied.

Approach: We used the GEOCHEQ code [9] to explore the effects of solution pH, solution/rock ratio (expressed as water/rock ratio, *W/R*) and *T* on equilibrium secondary mineralogy and solution chemistry of systems during water-rock interactions. A series of H_2SO_4-HCl solutions with pH<~7 were chosen because of chemical and mineralogical signs of low-pH alteration of martian rocks [e.g., 10, 11] and preferential deposition of silica from low-pH solutions [12, 13]. Temperatures between 0 and 200ºC were used; an upper limit of 200ºC was chosen because of the inability of metastable amorphous silica to form in higher *T* solution-rock systems [13]. A simplified chemical composition of the Adirondack-type olivine basalt from Gusev crater was used as the input composition [14]. Systems were calculated open with respect to current martian atmospheric O_2 and CO_2. Some models were open with respect to solution pH; this modeled continuous input of acid. Other modeled systems were closed, allowing pH to change from an initial system pH with rock alteration.

Effect of pH: Equilibrium calculations open with respect to acid solution show that silica-dominated assemblages can form at T<~25ºC, high W/Rs (~10^2-10^4), and pHs<~2-3 (Fig. 1). Ti-oxide phases, represented by rutile and titanite in the model, form under all conditions in which amorphous silica forms. Significant amounts of silica can form over a greater range of W/R ratios and at higher temperatures (T<~150ºC) at pH<~2-3. In these equilibrium assemblages, the other minerals consist mainly of iron oxides/oxyhydroxides (hematite or goethite), Al-phyllosilicates and Ti-oxide minerals (rutile or titanite) (Fig. 1 and 2).

Equilibrium calculations in systems closed with respect to the acid solution show similar trends to those discussed above. For example, systems with initial pH=1 and $W/R=10^3$ produced the mineral assemblages shown in Fig. 3 as functions of *T*. In this case, a silica-only assemblage occurs at *T*~<30ºC. At higher *T*, assemblages consisting of silica and iron oxides/oxyhydroxides form up to *T*~100ºC.

For a given *W/R* and *T*, the volume of silica in a secondary assemblage will increase with a decrease of the solution pH. At pH>~3, some silica may form in some systems, but secondary assemblages also consist of phyllosilicates, iron oxides, zeolites, and/or carbonates.

Silica deposition from cooling fluids: If equilibrium cooling of high-*T* solutions is modeled, for example from 200ºC to 0ºC, secondary mineral assemblages dominated by silica can form over a wide range of pH at 0ºC. When systems equilibrate at high *T*, only some silica (more at lower initial pH) and many other minerals (e.g., phyllosilicates) form. The solution remaining at high *T* will have been neutralized in the process of water-rock interaction, in some cases to relatively high pH (as high as ~10). If the remaining solution is then cooled, silica that was still in solution precipitates. Our models show that if this cooled solution is removed from the minerals precipitated at the higher *T*, such as by flow of the solution as it was cooling, this can result in a new secondary assemblage dominated by silica. These silica-dominated assemblages would have greater volumes of silica if cooled from higher *T* (Fig. 4), if the system is higher *W/R* (not shown), or lower pH (Fig. 4). These silica-dominated deposits do not generally have Ti-oxide phases present, as Ti minerals tend to precipitate at higher *T*.

Summary and Implications: Without fluid cooling, silica-dominated assemblages only formed at low *T*, low pH, and high *W/R* ratios. Ti-bearing phases occur with the silica, consistent with observations in

Gusev crater [6]. High *W/R* conditions may imply fluid flow (e.g., spring discharge). Without flow of solutions, which is required to transport and remove elements, silica would be a small component of surface deposits formed through cooling or evaporation/freezing in place.

In the case of cooling of hydrothermal fluids, silica-dominated assemblages can form over a much larger range of pH values, initial temperatures, and *W/R* values. However, these assemblages generally do not have significant Ti-bearing phases.

Overall, these results suggest that the Gusev deposits, and other silica deposits on Mars, could form from high or low *T*, but low pH (<~2-3), flowing solutions, for example in spring settings. However, for the Gusev materials, if Ti-materials are not part of a lag deposit and instead result from dissolution and precipitation, the low-*T* setting may be more likely to produce those silica deposits that are also TiO_2 rich.

References: [1] McLennan S.M. (2003) *Geology*, *31(4),* 315. [2] Glotch T.D., et al. (2006) *JGR*, *111*, E12S03. [3] Kraft M.D., et al. (2007) *7th Int. Conf. on Mars*, abst. 3396. [4] Bandfield, J.L. (2008) *GRL, 35*, L12205. [5] Milliken, R.E., et al. (2008) *Geology, 36*, 847. [6] Squyres, S.W., et al. (2008) *Science, 320*, 1063. [7] Ruff S.W. et al. (2007) *Eos Trans. AGU*, 88(52), Fall Meet. Suppl., Abst. P23A-1097. [8] McAdam, A.C., et al. (2008) *JGR, 113*, E08003. [9] Mironenko, M. V., et al. (2008) *Herald DGGGMS RAS*. [10] Ming D.W. et al. (2006) *JGR*, *111*, E02S12. [11] Hurowitz, J.A., et al. (2006) *JGR, 111*, E02S19. [12] Dove P.M. (1995) In Chem. Weath. Rates Silicate Min., MSA, Washington, D.C.. [13] Dove P.M. and Rimstidt J.D. (1994) In Silica: Phys. Behavior, Geochem., and Mat. Apps., MSA, Washington, D.C. [14] McSween, H.Y. et al. (2006) *JGR, 111*, E02S10.

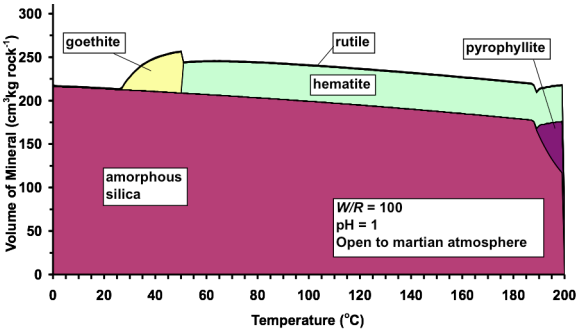

Figure 1. Equilibrium mineral assemblage with temperature, from a fixed pH 1, *W/R*=100 run.

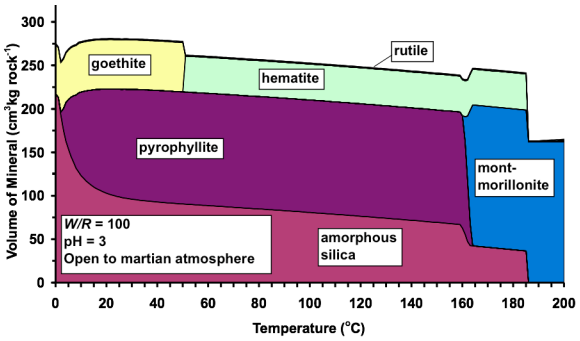

Figure 2. Equilibrium mineral assemblage with temperature, from a fixed pH 3, *W/R*=100 run.

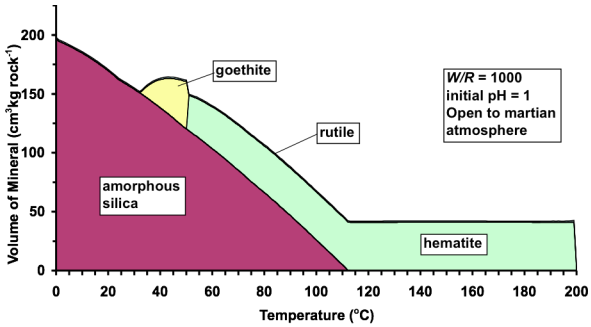

Figure 3. Equlibrium mineral assemblages with temperature in an initial pH = 1 and *W/R* = 1000 system.

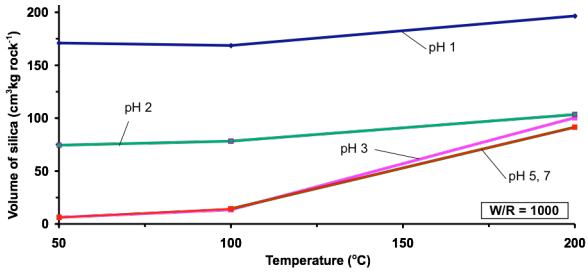

Figure 4. Volume of silica formed after solution flow and cooling from several temperatures (200°C, 100 °C and 50°C) to 0°C, in *W/R* = 1000 systems of several initial pHs. The pH 5 and 7 lines overlap.

LARGE-SCALE STRUCTURAL MANIFESTATIONS OF PHYLLOSILICATE GENERATION AND DEPOSITION IN EARLY MARTIAN HISTORY. P. J. McGovern[1] and J. K. Morgan[2], [1]Lunar and Planetary Institute, USRA, 3600 Bay Area Blvd., Houston TX 77058, USA (mcgovern@lpi.usra.edu), [2]Department of Earth Science, Rice University, Houston, TX 77005, USA (morganj@rice.edu),

Introduction: Recent detections of phyllosilicate (clay) minerals in ancient terrains [1-3] have revolutionized our understanding of early hydrothermal activity on Mars. The spectral signatures of phyllosilicates are seen exclusively in Noachian-aged outcrops and not in Hesperian or Amazonian materials [1-3]. Phyllosilicates are inferred to have been widely emplaced during a period of time (termed the "Phyllosian" in [2]), that overlaps with, but ends before the end of, the Noachian. Afterward, conditions (such as pH) changed such that phyllosilicate formation was inhibited; instead, materials such as sulfates were favored. The potential existence of extensive phyllosilicate deposits low in the stratigraphic column has enormous implications for the structural evolution of materials emplaced higher in the column. Clay layers are often zones of low strength, enabling enhanced deformation and slip in terrestrial settings, such as fault zones, accretionary wedges, and basal decollements beneath volcanoes [4-8]. The low hydraulic diffusivity of clays also makes lateral transport of pore water difficult, thus facilitating the buildup of high pore pressures in a decollement [9-11].

Here we develop the idea that ancient phyllosilicate deposits, generated by vigorous hydrothermal activity early in Martian history [e.g., 12] and concentrated by sedimentary processes, may constitute decollement zones that facilitate movement and deformation of younger superposed structures, such as large volcanic edifices, wrinkle ridge provinces, and thrust belts.

Flank Movements at Large Volcanic Edifices: The 23 km tall, 600 km wide Olympus Mons edifice exhibits several characteristics of volcanic spreading, including concave-upward lower flank topography, faulting (both extensional and compressional), and a large basal scarp, sectors of which constitute the headscarps of giant landslides (the Olympus Mons aureoles) [13-15]. These features have been attributed to motion along a basal decollement rooted in a thick basal clay layer [15]. The asymmetric distribution of topography and tectonics seen at the Olympus Mons edifice, scarp, and aureole described are best explained by a gradient in basal friction beneath the edifice, increasing toward the southwest (e.g, with proximity to the Tharsis rise) [15]. Such a gradient is consistent with a decrease in sediment thickness with increasing elevation, as would be expected if sediments are transported from sources (highlands) to sinks (lowlands and basins).

If Noachian sediments were distributed preferentially in lowlands, then volcanoes at low basal elevations elsewhere on Mars are the most likely to have basal detachments. Large volcanoes in the lowlands are generally lacking, but Apollinaris Patera (AP), like Olympus Mons, is located at the highland-lowland transition. AP has several features consistent with Olympus Mons-style basal spreading: concave-up flank slopes and a partial basal escarpment with distributed broken-up terrain beneath and surrounding it (a potential aureole analog). AP is near the mouth of Ma'adim Valles, which may have yielded a large supply of sediments from the highlands to the base of AP. The Tharsis Tholus edifice northeast of Tharsis exhibits throughgoing faulting that has been attributed to deformation of a ductile basal layer [16]. The current basal elevation is ~+2 km, higher than that of our other examples, but estimates of 0.5-3.5 km of flank burial by voluminous lavas from higher on the Tharsis rise [16-17] imply a somewhat lower original base for Tharsis Tholus, consistent with a sediment-covered lowlands base and resulting decollement.

Conversely, the bases of the Tharsis Montes are at very high elevations on the Tharsis Rise, and therefore unlikely to exhibit significant thicknesses of phyllosilicate sediment. This inference is consistent with the absence of spreading-related structures (scarps, aureoles); the abundant extensional features on these edifices are likely to be related to intrusion [e.g., 18-19] rather than spreading. Similarly, highland paterae and shields are based at relatively high elevations, rendering them unlikely locations for large accumulations of sediment. The older ages of these structures relative to the Tharsis volcanoes also suggests that construction of edifices may have started well before the end of phyllosilicate production.

Wrinkle Ridge Formation in Solis and Lunae Plana: Narrow crenulated ridges with sinuous planforms, called wrinkle ridges, deform volcanic plains units in many regions of Mars, but are particularly well expressed in the Solis Planum and Lunae Planum regions east of Tharsis. While wrinkle ridges are uniformly recognized as manifestations of compression, the subsurface fault depth and geometry that produces the observed surface structures are controversial; both thick-skinned [e.g., 20] and thin-skinned [e.g., 21]

models have been proposed. In particular, a thin-skinned model for Solis and Lunae Plana [21] postulates a decollement at shallow depth (~4.5 km) that focuses deformation and produces the characteristic arches and wrinkles. We propose that overpressurized clay layers could provide such a decollement beneath volcanic plains regions like Solis and Lunae Plana.

Thrust Belt Orogeny in Thaumasia: The Thaumasia Region comprises a ring of elevated terrain of Hesperian and Noachian age to the south and east of central Tharsis. Scenarios for producing the elevated terrain include broad-scale thrusting and volcanism [e.g., 22]. The thrust belt scenarios require some sort of mechanically weak basement material. One scenario [23] invokes ductile deformation of evaporites (sulfate and other salts), consistent with potential salt tectonic features in Valles Marineris [24]. Under this scenario, proposed sulfate evaporites outcropping from layers in the walls of Valles Marineris are the local expression of massive and widespread evaporites underlying the whole of Solis Planum and the Thaumasia rises [23], allowing generation of the wrinkle ridges and fringing mountain belts in those regions, respectively.

We argue that a clay-based overpressurized decollement is a more likely scenario for mobilizing compressional features within Thaumasia. The mountainous rim of Thaumasia is among the oldest terrain associated with the margins of Tharsis, with ages spanning the Noachian and Early Hesperian [22]. The highest, oldest terrain dates from the mid-Noachian; thus, material beneath it must be comparably old or older. Our current understanding of hydrothermal systems on Mars [1-3] indicates that conditions favored phyllosilicate formation and prevented formation of sulfates during the required time (mid-Noachian or earlier). Thus, it is unlikely that sulfate evaporites are driving the formation of the margins of Thaumasia, and, similarly, hydrothermally altered materials at depths 5-15 km beneath the surface of Solis Planum are more likely to be materials produced during the early to mid-Noachian (clays) than later (sulfate-containing evaporites). Futhermore, salt beds are buoyant with respect to dense volcanic rocks; in tectonically active systems, salt tends to ascend via diapiric instabilities and exploitation of faults as conduits [25-26], leading to an expectation of exposure of such materials at the surface above a pervasive and laterally extensive deposit. No such evidence is seen at the surface in Solis Planum or Thaumasia.

Several objections to decollement-based deformation have been raised on the grounds of the purportedly unrealistic pore pressure magnitudes required for gravity to move a wedge with such a low surface slope [23, 27]. However, a number of accretionary wedges with high basal pore fluid pressures in sealed decollements (approaching lithostatic, or pore pressure/lithostatic pressure ratio $\lambda_f \sim 1$) occur on Earth, [e.g., 5]. Such a system accommodates gravitationally driven spreading along passive margins in the Niger Delta [e.g., 25, 28]. Furthermore, a pressurized decollement provides a natural source of water for formation of channels observed on the outer margins of Thaumasia [29].

Discussion: Vigorous hydrothermal circulation early in Martian history [12] likely accounts for the widespread evidence of phyllosilicates in Noachian terrains [1-3]. The implied abundance of water also suggests that erosional transport and deposition of phyllosilicates was vigorous in this epoch. Given that the Tharsis rise has been elevated since the early Noachian [30], erosion should favor collection of Tharsis-derived, clay-dominated sediments in the lower regions surrounding the rise. Thus, it is no surprise that a number of tectonic manifestations of stratigraphically low sediment-based decollements should occur in the regions surrounding Tharsis. Clay sediments may play an important role in controlling the geologic and tectonic history of the circum-Tharsis region, and other regions where topographic gradients favor accumulation of sediments, such as the dichotomy boundary under Apollinaris Patera.

References: [1] F. Poulet et al., *Nature, 438*, 623, 2005; [2] J.-P. Bibring et al., *Science, 312*, 400, 2006; [3] J. F. Mustard et al., *Nature, 454*, 309, 2008; [4] J. D. Byerlee, *Pure Appl. Geophys., 116*, 615, 1978; [5] D. Davis et al., JGR, 89, 10,187, 1984; [6] P. Vrolijk, *Geology, 18*, 703, 1990; [7] D. S. Cowan et al., *GSA Bull., 115,* 1230, 2003; [8] R. P. Denlinger and P. Okubo, *JGR, 100*, 24,499, 1995; [9] J. Arch and A. Maltman, *JGR, 95*, 9035, 1990; [10] R. M. Iverson, *JVGR, 66*, 295, 1995; [11] G. C. Rawling et al., *Geology, 29*, 43, 2001. [12] S. P. Schwenzer and D. A. Kring, *Workshop on Modeling Martian Hydrous Environments* (this volume), abstract 4015, 2009; [13] A. Borgia et al., *JGR, 95*, 14,357, 1990; [14] P. J. McGovern et al., *JGR, 109*, doi10.1029/ 2004JE002258, 2004; [15] P. J. McGovern and J. K. Morgan, *Geology, 37*, 139, 2009. [16] J. B. Plescia, *Icarus, 165*, 223, 2003; [17] M. Robinson, Dissertation, University of Hawaii, 1993; [18] L. G. J. Montesi, *GSA Spec. Pap. 352*, 165, 2001; [19] P. J. McGovern et al., *JGR, 106*, 23,769. 2001; [20] L. G. J. Montesi and M. T. Zuber, *JGR, 108*, doi: 10.1029 /2002JE001974, 2003; [21] T. R. Watters, *Icarus, 171*, 284, 2004; [22] J. M. Dohm and K. L. Tanaka, *Planet. Space Sci., 47*, 411, 1999; [23] D. R. Montgomery et al., *GSA Bull., 121*, 117, 2009; [24] D. R. Mongomery and A. Gillespie, Geology, 33, 625, 2005; [25] M. G. Rowan, et al., in *K.R. McClay, ed., Thurst Tectonics and hydrocarbon systems: AAPG Memoir 82*, 157, 2004; [26] M. R. Hudec and M. P. A. Jackson, 2007, *Earth Science Reviews, 82*, 1, 2007; [27] A. L. Nahm and R. A. Schultz, *LPSC XL*, abstract 1069, 2009; [28] P. R. Cobbold, et al., *Petroleum Geoscience, 15*, 3; DOI: 10.1144/1354-079309-784, 2009; [29] K. L. Tanaka et al., *JGR, 103*, 31,407, 1998; [30] R. J. Phillips *et al., Science, 291*, 2587, 2001.

LIQUID INTERFACIAL AND MELT-WATER IN THE UPPER SUB-SURFACE OF MARS.

D. T. F. Möhlmann, DLR Institut für Planetenforschung, D-12489, Berlin, Germany, dirk.moehlmann@dlr.de

Abstract: Conditions for the, at least temporary, presence of nano- to micrometer sized layers of liquid interfacial water and melt-water in the upper martian surface are described. Interfacial water can evolve there, as on Earth, in "sub-zero temperaturel" soils in course of "premelting of ice" and due to attractive van der Waals interactions at ice-mineral interfaces [1]. The physical background, related models and possible also macroscopic physical and possibly also biological consequences are described.

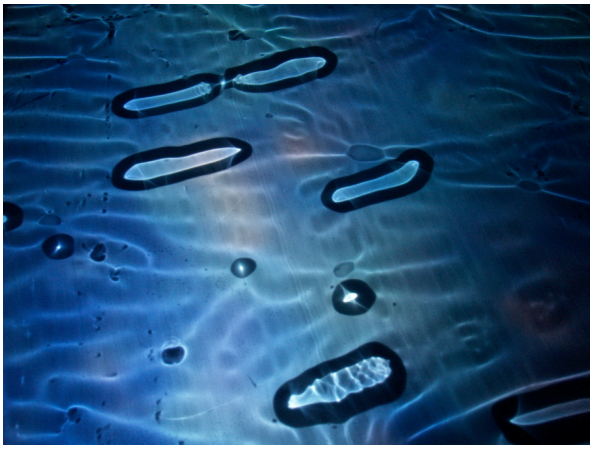

Image credit: Helmut Eigenmann
Illustration of liquid water-film covered particles in ice (no photo !).

Furthermore, as in cool regions on Earth, the solid-state greenhouse effect, can in course of diurnally and seasonally varying insolation (flow-in of solar energy [W m^{-2}]), give conditions in favor of temporary melting processes in upper sub-surface parts of snow/ice-packs on Mars at subzero sub-surface temperatures. The conditions for this possibly temporary melting are with different sub-surface energy absorption models quantitatively described for model parameters, which are typical for the thermo-physical conditions at snow/ice sites on the surface of present Mars. It is demonstrated by numerical modeling that conditions can result, which are in favor of a (possibly also repetitive) evolution towards cm- to dm-sized layers of liquid water in upper sub-surfaces of snow/ice-packs on Mars [2]. This liquid water can form in sufficient amounts to be relevant for macroscopic physical (rheology, erosion), chemical, and eventually also for biological processes. The conditions for the necessary preceding presence of snow/ice covered surfaces, and thus also for a temporary existence of liquid sub-surface water, are on present Mars "paradoxically" more favorable at sites in higher latitudes, since present deposits of snow/ice can mainly be found there. Possible rheologic and related erosion consequences of the appearance of liquid sub-surface water in martian snow/ice-packs are discussed in view of current observations of recent rheologic processes.
Seepages [3], gully-like rheologic phenomena, "white collars", e.g. are among the candidates to be modeled in trems of springtime sub-surface melting and related active processes on present Mars.

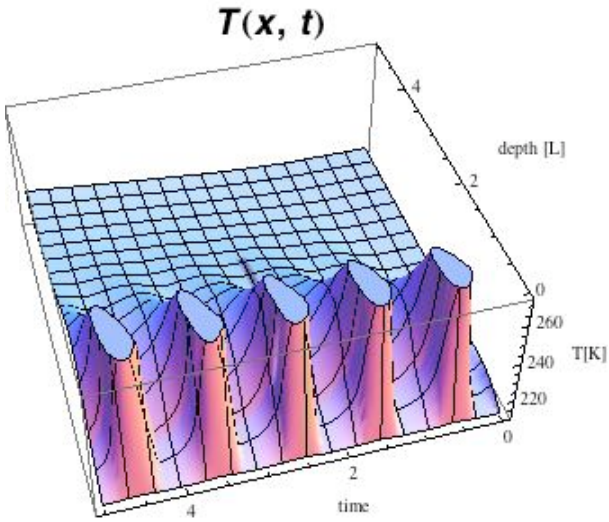

Example of a temperature field T(x,t), describing that the melting temperature (plateaus) can within a few sols be reached in the sub-surface of optically translucent ice at about 10 cm below the surface Depths are given in units of L = 11.4 cm. Time is given in sols. Heating can happen at a surface depth of and around 6.3 cm depth.

References:

[1] Möhlmann, D.T.F. (2009) *Cryobiology,* doi:10.1016/j.cryobiol.2009.01.004. [2] Möhlmann, D.T.F, (2009) *Icarus (submitted)* - Temporary liquid water in upper snow/ice sub-surfaces on Mars?. [3] Kereszturi, A. et al. (2009), Icarus, doi:10.1016/j.icarus.2009.01.014

CHEMICAL AND MINERALOGICAL CONSTRAINTS FOR MODELING HYDROUS ENVIRONMENTS ON MARS FROM THE MARS EXPLORATION ROVERS. R. V. Morris[1] and D. W. Ming[2], [1]Code KR, ARES NASA Johnson Space Center, Houston TX 77058 (richard.v.morris@nasa.gov), [2]Code KX, ARES NASA Johnson Space Center, Houston TX 77058 (douglas.w.ming@nasa.gov).

Introduction: The twin Mars Exploration Rovers (MER) Spirit and Opportunity have explored the Martian surface at Gusev Crater (GC) and Meridiani Planum (MP) for more that 1840 sols (more than 5 Earth years). Their science payload [1] includes instruments for mineralogical (Mössbauer (MB), Mini-TES, and Pancam) and chemical (APXS) analysis and a tool (RAT) for brushing and grinding rock surfaces. Rover wheels are used to expose subsurface soil. We will focus here primarily on results from the MB (Fe mineralogy) and APXS instruments and the constraints they provide for modeling hydrous environments.

Fe-bearing phases: The concentration and mineralogical speciation of Fe constrain the nature and progress of alteration processes by the extent of its mobility in hydrous environments, by its distribution between oxidation states (Fe^{2+} and Fe^{3+}), and by its mineralogical speciation.

Fourteen Fe-bearing phases have been identified by MB [2-4]: 5 primary igneous silicate/oxide phases (olivine, pyroxene, ilmenite, magnetite, and chromite (one occurrence)), 7 secondary phases (nanophase ferric oxide (npOx), hematite, goethite, jarosite, pyrite/marcasite (one occurrence), ferric sulfate, and an unidentified Fe^{3+} phase referred to as Fe3D3), and 2 meteorite phases (metallic-Fe and troilite). NpOx is ubiquitous and associated in various proportions with basaltic soils and many basaltic rocks, and it is interpreted to be the primary Fe-bearing component in martian dust. Goethite, along with hematite, is found in highly altered rocks in the GC Columbia Hills at West Spur and Husband Hill. Jarosite, hematite and Fe3D3 are components of the S-rich outcrop at MP. In addition, hematite-rich spherules (a.k.a. blueberries) are imbedded in the outcrop and are present as a lag on the surface. Ferric sulfate is found subsurface in GC on Husband Hill and at several locations near Home Plate. The occurrence of the sulfide pyrite/marcasite is a float rock on Home Plate.

Goethite and jarosite both contain OH in their structure and therefore formed in the presence of H_2O. Ferric sulfate also reasonably requires H_2O for its formation.

Constraints on chemistry, mineralogy, formation pathways: We next combine the Fe-mineralogy discussed above and APXS chemical data [5-8] that together provide ground-truth for modeling hydrous environments on Mars. We will not consider numerical models, but we will point to styles of alteration that are indicated by the Fe-mineralogy and chemistry.

Meridiani Planum. The bulk chemical and mineralogical composition of the S-rich outcrop over Opportunities ~10 km traverse is nearly constant [8] (Table 1). The Fe mineralogy is subequal proportions of Fe from jarosite, hematite (not spherule hematite), and Fe3D3 (Fe^{3+}/Fe_{Total} ~ 0.85) [3]. The bulk chemical composition, calculated to a Cl- and SO_3-free basis, is basaltic, implying isochemical alteration of precursor basaltic materials is a reasonable working hypothesis (i.e., low water-to-rock ratios with only the additions of Cl, SO_3, and H_2O). (Note: Chemical data from APXS are calculated to a H_2O/OH-free basis because the instrument does not detect H, although estimates of H_2O contents are being made from proton scatter peaks in APXS spectra [9]). Low-pH, acid-sulfate formation conditions are implied by the presence of jarosite and the high SO_3 concentrations. The MP spherules are evidence for hydrothermal conditions as a working hypothesis, because similar spherules were formed under hydrothermal conditions on Mauna Kea volcano and in the laboratory from hydronium jarosite precursors [10,11]. An important unknown is the mineralogical and chemical composition of the aluminosilicate alteration product.

Gusev Crater. Several different hydrous environments were encountered by Spirit in the Columbia Hills. High-SiO_2 soils (~90% in the soil Kenosha Comets) are present in Eastern Valley adjacent to Home Plate [12], which is in the Inner Basin and interpreted as a volcanic complex [13]. A high-SiO_2 float rock with pyrite/marcasite (Fuzzy Smith) was analyzed on Home Plate, and Mini-TES measurements of the high-SiO_2 soils (Fuzzy Smith was not analyzed) show that high-SiO_2 phase is amorphous as opposed to quartz [12]. Because these high-SiO_2 materials are also enriched in TiO_2 relative to local precursor basaltic compositions, acid sulfate leaching is a proposed interpretation of the chemical data [4,12]. All elements detected by APXS are leached (high water to rock ratios) except for SiO_2 and TiO_2 whose concentrations are passively enriched because they precipitate as insoluble phases (possibly anatase and opal-A). Palagonitic tephra (aqueous alteration at low water to rock ratios) is also interpreted to be present at Home Plate (Barnhill Class rock) [4].

Independence Class outcrop rocks on the NW slope of Husband Hill have low total Fe contents (2-5%), slightly enriched SiO_2 concentrations (50-55%), and high Al/Si ratios that are interpreted to result from leaching and alteration in a hydrous environment (high water to rock ratios) (Table 1) [7,14]. The significant difference in bulk chemical composition between the Independence Class rocks and the high-SiO_2 rocks at Home Plate is evidence for leaching of the former under more neutral pH conditions [7]. The elemental composition of Independence Class rocks suggest an smectite or smectite-like component, but the mineralogical presence of smectite is not supported by Mini-TES measurements [14].

Ferric sulfate was identified by MB in subsurface soils that have high SO_3 (22-36%) and H_2O (6-19%) concentrations at three locations in Gusev Crater (NE Husband Hill, between Husband Hill and Home Plate, and at Tyrone SE of Home Plate) [9,15,16]. These soils (Paso Robles Class) are interpreted to have formed under oxidizing, acid-sulfate conditions as hydrothermal condensates [16].

Isochemical alteration (hydrous alteration at low water to rock ratios) is indicated for the Watchtower Class rocks on Husband Hill (Table 2). The rocks have a nearly constant chemical composition and a mineralogical composition that ranges from ~63% of Fe_{Total} from olivine, pyroxene, ilmenite, and magnetite and Fe^{3+}/Fe_{Total} ~0.43 (Keystone) to ~13% of Fe_{Total} from those phases and Fe^{3+}/Fe_{Total} ~0.88 (Pequod) [4,7]

Clovis class rocks on West Spur of the Columbia Hills have compositions similar to basaltic soils, excepting higher Mg, Cl, and Br and lower Ca and Zn. The presence of goethite and secondary aluminosilicates (inferred from chemical data) point to alteration in hydrous environments [4,6].

References: [1] Squyres et al. (2003) *JGR*, *108*, 8062, doi:10.1029/2003JE002121. [2] Morris et al. (2006) *JGR*. *111*, E02S13, doi:10.1029/2005JE002584. [3] Morris et al. (2006) *JGR*, *111*, E12S15, doi:10.1029/2006JE002791. [4] Morris et al. (2008) *JGR*, *113*, E12S42, doi:10.1029/2008JE003201. [5] Gellert et al. (2006) *JGR*, *111*, E02S05, doi:10.1029/2005JE002555. [6] Ming et al. (2006) *JGR*, *111*, E02S12, doi:10.1029/2005JE002560. [7] Ming et al. (2008) *JGR*, *113*, E12S39, doi:10.1029/2008JE003195. [8] Gellert, manuscript in preparation. [9] Campbell et al. (2008) *JGR*, *113*, E06S11, doi:10.1029/2007JE002959. [10] Morris et al. (2005) *EPSL*, *240*, 168. [11] Golden et al. (2008) *Amer. Mineral.*, *93*, 1201. [12] Squyres et al. (2008) *Science*, *320*, 1063. [13] Squyres et al. (2007) *Science*, *316*, 738. [14] Clark et al. (2007) *JGR*, *112*, E06S01, doi:10.1029/2006JE002756. [15] Arvidson et al. (2008) *JGR*, *113*, E12S33, doi:10.1029/2008JE003183. [16] Yen et al. (2008) *JGR*, *113*, E06S10, doi:10.1029/2007JE002978.

Table 1. APXS and MB data for Average MP Outcrop and Calculated Basaltic Precursor

	MP Outcrop[a]	MP Precursor[a]	GC Kenosha Comets[b]	GC Independence Penn[b]
SiO_2 wt%	36.47	48.19	90.5	54.9
TiO_2	0.76	1.01	1.21	1.88
Al_2O_3	6.09	8.06	1.7	18.7
Cr_2O_3	0.19	0.25	0.33	0.04
Fe_2O_3	14.61	5.08	0.4	1.1
FeO	2.24	15.67	0.4	2.9
MnO	0.32	0.43	1.0	0.08
MgO	7.71	10.40	2.3	3.4
CaO	4.79	6.46	0.7	7.3
Na_2O	1.59	2.19	0.3	3.2
K_2O	0.58	0.75	0.00	0.52
P_2O_5	1.03	1.37	0.03	3.48
SO_3	22.26	0.00	1.00	2.2
Cl	1.06	0.00	0.1	0.3
Total	99.87	99.87	99.88	99.90
Br µg/g	80	107	151	24
Ni	602	798	278	444
Zn	427	554	17	667
Fe^{3+}/Fe_T	0.85	0.23	0.36	0.35

[a]After [3]. Outcrop chemical data from [ref] for surfaces exposed by RAT grinding. Precursor calculated assuming Fe^{3+}/Fe_{Total} = 0.23 and SO_3 = Cl = 0.0. [b][7,14]

Table 2. APXS and MB data for GC rocks Methusela_Keystone and Pequod_Ahab. Pie diagramsshow the proportion of total Fe associated with Fe-bearing phases.

	Methuselah Keystone[a]	Pequod Ahab[b]	MB Fe Mineralogy[c]
SiO_2 wt%	47.0	46.0	
TiO_2	2.21	1.92	
Al_2O_3	12.44	13.1	
Cr_2O_3	0.11	0.05	
Fe_2O_3	5.00	10.74	
FeO	5.96	1.32	
MnO	0.31	0.20	
MgO	8.38	8.4	
CaO	5.75	7.1	
Na_2O	3.3	3.5	
K_2O	0.51	0.38	
P_2O_5	1.23	2.83	
SO_3	4.95	4.3	
Cl	0.92	1.0	
Total	99.91	99.88	
Br µg/g	232	250	
Ni	155	94	
Zn	117	80	
Fe^{3+}/Fe_T	0.43	0.88	

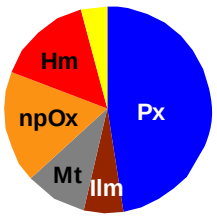

Keystone

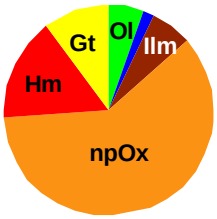

Pequod

[a][5]. [b][6]. [c][4].

Hydrous Environments on Mars from Visible-Infrared Orbital Data J. F. Mustard[1], S. L. Murchie[2], J-P. Bibring[3], J. L. Bishop[4], B. L. Ehlmann[1], N. McKeown, R. E. Milliken[5], F. Poulet[3], and L. E. Roach[1] [1]Brown University, Providence, USA, [2] The Johns Hopkins University Applied Physics Laboratory, Laurel, MD, [3]IAS, Université Paris-Sud, 91405 Orsay, France, [4]SETI Institute, Mountain View, CA, John_Mustard@brown.edu

Introduction: Data acquired over the past 5 years from the Mars Express OMEGA (Observatoire pour la Mineralogie, L'Eau, les Glaces et l'Activitié) [1] and Mars Reconnaissance Orbiter CRISM (Compact Reconnaissance Imaging Spectrometer for Mars) [2] show a wide diversity hydrated mineral phases distributed across Mars [1, 3, 4, 5, 6, 7]. The increased spatial resolution of CRISM (18 m/p) has lead to the identification of additional mineral phases as well as to refinements in the understanding of the geologic setting in which they exist.

Numerous analyses of the specific geologic settings in which the aqueous minerals are identified have recently been summarized [8] where a systematic assessment identifies at least ten distinct hydrous environments: Deep phyllosilicates, layered phyllosilicates, phyllosilicates in intra-crater fans, plains sediment, intra-crater clay-sulfate deposits, carbonate-bearing deposits, Meridiani-type layered deposits, Valles-type layered deposits, hydrated silica-bearing deposits, and surrounding the North Polar Cap gypsum plains. The listing of deposits follows the approximate age of the units that host the deposits, from oldest to youngest. We will discuss a few of these deposits classes here.

The apparent distinction between Noachian-aged terrains enriched in phyllosilicate minerals and Hesperian-aged terrains enriched in sulfate minerals was a fundamental result from the OMEGA experiment [1]. Bibring et al [1] proposed a model where the transition between these distinct mineralogic eras was a consequence of a fundamental re-organization of the martian global system. While the detailed obseravations of CRISM have supported the apparent distinction between older phyllosilicate terrains and younger sulfate terrains [5], it has also provided additional data on the specific geologic environments and identified several distinct envionrments not previously identified [8].

The largest class of aqueous deposit is the deep phyllosilicates. This is found thoroughout the southern highlands, deep exposures in Valles Marineris as well as large impact craters in the northern plains that penetrate beneath the cover of Hesperian-aged ridge plains and Vastitas Borealis formation. In the southern highlands the phyllosilicates are commonly observed associated with rims, ejecta, walls and central peaks of impact craters. The broad distribtion among all elements of impact craters implies that the target rocks were altered prior to crater formation. A survey of mineral classes associated with impact craters shows that there is no relationship between mineral type and craters size, and that Fe/Mg smectite and chlorite phyllosilicates dominate [9]. Furthermore high resolution imaging of well exposed ancient basement rocks show that it is estensively brecciated [10, 11]. Whatever process or processes resulted in the formation of deep phyllosilicates, they needed to be extensive to creat a global signature and of moderate temperature and pressure to leave a predominance of Fe/Mg smectite clays.

Clear evidence for hydrothermal assemblages are rare. Some indicator minerals are associated with impact craters where the mineral prehnite is observed, as well as chlorite, zeolite, opal/hydrated silica and muscovite/illite [7]. Serpentine has recently been identified on Mars in a few isolated regions [12], one in association with olivine-rich terrains in Nili Fossae. While hydrothermal systems in association with impact craters is widely expected on Mars [e.g. 13] the evidence for a common occurrence is equivocal.

Layered phyllosilicates are best observed in the region surrounding Mawrth Valles [14, 15]. They are regional, compositionally layered, and form discrete, polygonally fractured layers having a distinctive stratified composition. At Mawrth Vallis the layers are >150 m and form a sequence of (a) a lower layer Fe/Mg-rich clay, typically nontronite, (b) a middle layer of Al-rich smectite, possibly montmorillonite, and sometimes (c) a thin upper layer containing an Al-phyllosilicate of the kaolinite group and probably hydrated silica. The lower beds contain a strong signature of alteration to ferric phases, but ferrous phases are present both above and below the contact of the Fe/Mg- and Al-rich clays suggesting at least transient reducing conditions. In the Nili Fossae region a distinct thin unit rich in kaolinite is observed a the top of Noachian-aged sediment filling craters, possilbly the remnants of a pedogenic horizon [16]. Proposed origins of layered phyllosilicates include marine sedimentation of sorted, transported clays, alteration of volcanic ash, hydrothermal alteration by cap rock deposited as an overlying impact melt sheet, or pedogenesis of basaltic regolith.

A thin, regionally placed carbonate-bearing bedrock deposited is mostly observed in olivine-rich regions surrounding the Isidis basin, especially in the Nili Fossae region [17]. The carbonate-bearing layer is about 20 m thick, and stratigraphically it lies above

local occurrences of layered phyllosilicates in association with a regional-scale olivine-rich layer [18, 19]. These deposits are thought to be hydrothermal alteration of the olivine by an overlying cap rock deposited as impact melt, or chemical sedimentation in surface waters.

Many of the intracrater fans identified by MOC imagery have been observed by CRISM and shown to contain hydrated mineral phases, dominantely phyllosilicates [e.g. 5, 6, 20, 8]. Typically the lower portions of the fans exhibit horizontal bedding and an enhanced content of phyllosilicate and the phyllosilicate signatures are consistent with that elsewhere in the drainage basins. The phyllosilicate-bearing stratified beds were apparently deposited in persistent standing water. It is not clear if the phyllosilicate was transported to the deposit or formed authigenically.

Plains sediments are an assemblage of chlorides and phyllosilicates that occurs in relatively flat areas of crater floors and intercrater plains, yet is not part of obvious depositional fans. These are largely recognized in THEMIS data as "glowing terrain" [21]. The geologically most reasonable phase with this property is chloride though no definitive spectral features are observed.

Sulfates are found in the Meridiani-type and Valles-type deposits. They are typically mono- or poly-hydrated and have a variety of possible depositional mechanisms. Like plains sediments, these represent evaporite salts formed in near surface or surface environments.

Hydrated silica deposits are thin, light-toned layered deposits superposed on Hesperian plains within about 200 km of Valles Marineris, southwest of Melas Chasma, south of Ius Chasma, south of western Candor Chasma, west of Ganges Chasma, and west of Juventae Chasma [22, 23]. These interesting and young deposits are characterized by beds about 10 m thick, polygonal fractures several meters in diameter, and are differentially eroded, presenting a morphology distinct from layered deposits within the chasmata. Stratigraphically, they appear to be above the Terra Meridiani layered deposits and comparable in age to the Valles Marineris layered deposits. Hydrated silica-rich deposits occur in some layers of the deposits where the spectral data indicate a variety of forms including altered glass, opal, and chalcedony. Other layers exhibit a suite of absorptions consistent with jarosite, indicating alteration under acidic conditions [22]. The relationship of the hydrated silica to high-Si deposits found by MER/Spirit [24] is unknown.

Proposed models for the origin of the hydrated silica overlap include acid weathering of volcanic ash or lava flows, precipitation from hydrothermal discharge, a mixture of chemical precipitation and detrital sedimentation in a fluvial or lacustrine environment [22, 23].

The diversity of deposits suggest a range of past aqueous environments. High resolution spectral and spatial imaging reveals many details of the stratigraphy that should constrain models for their formation. However, many of the details are still being investigated. Regardless the range of deposits that lend themselves to modeling hydrous environments provides a rich record.

References: [1] Bibring, J-P. et al. (2006) *Science, 312, 400-404.* [2] Murchie S.M. et al. (2007). *JGR, 112.* [3] Poulet, F. et al (2005) *Nature, 438, 623-627.* [4] Gendrin et al., Science, 307,1587-1591, 2005. [5] Mustard, J. F. et al., Nature 454, 305-309 doi:10.1038/nature07097, (2008). [6] Ehlmann, B.L., et al., Nature Geosciences, 1, 355-358, (2008). [7] Ehlmann, B. L. et al., (2009) JGR (submitted). [8] Murchie S.M. et al. A synthesis of Martian aqueous mineralogy after one Mars year of observations from the Mars Reconnaissance Orbiter (2009). *JGR, (submitted).* [9] Fraeman, et al., *LPSC XXXX (2009), Abstract #2320*. [10] McEwen, A. et al., Eos Trans. AGU, 89(53), Fall Meet. Suppl., P43D-03 (2008). [11] Mustard, J. F., et al., *LPSC XXXX (2009), Abstract #2115.* [12] Ehlmann, B. L., et al., *LPSC XXXX (2009), Abstract #1787*. [13] Newsom, H., Icarus, v. 44, 207-216 (1980). [14] Loizeau et al., 112, E08S08, doi:10.1029/2006JE002877 (2007). [15] Bishop, J. L., et al., Science, 321, 830-833, (2008). [16] Mustard, J. F., et al., (2009) JGR (*submitted*). [17] Ehlmann, B. L. et al. Science, 322, DOI: 10.1126/science.1164759, 1828-1832, 2008 [18] Hamilton, V. E. and P. R. Christensen, *Geology* 33, 433 (2005). [19] Mustard, J. F. et al., *JGR* 112 doi: 10.1029/2006JE002834 (2007). [20] Milliken, R.E. et al., *LPSC XXXX,* 2009. [21]Osterloo, M. M., et al., Science, 319, 1651-1654, 2007 [22] Milliken, R., Geology, 36, 847-850, (2008). [23] Weitz, C. M. et al., submitted to Icarus, 2009. [24] Squyres S. W., et al.Science, 320, 1063-1067, 2008.

CONSTRAINTS FOR MODELING CHEMICAL TRANSPORT DURING HYDROTHERMAL ALTERATION IN LARGE AND SMALL IMPACT CRATERS. H. E. Newsom, Univ. of New Mexico, Institute of Meteoritics, Dept. of Earth & Planetary Sci., Albuquerque, NM 87131, USA newsom@unm.edu.

Introduction: Modeling of hydrothermal alteration has progressed greatly in recent years. One of the next challenges for modeling is to explain the observations of elemental transport observed in terrestrial impact craters. We present data from our work that illustrates some of the evidence for impact craters of different sizes. For the large, 180-200 km diameter, Chicxulub impact crater, data from the Yaxcopoil 1 drill core suggests that some chemical transport has occurred, especially for Li, B, and Be. In contrast, for the small 1.8 km diameter Lonar crater, very little evidence for chemical mobility has been found. Extrapolation models to other planetary bodies, such as Mars, will require an appreciation of the differences in fluid composition.

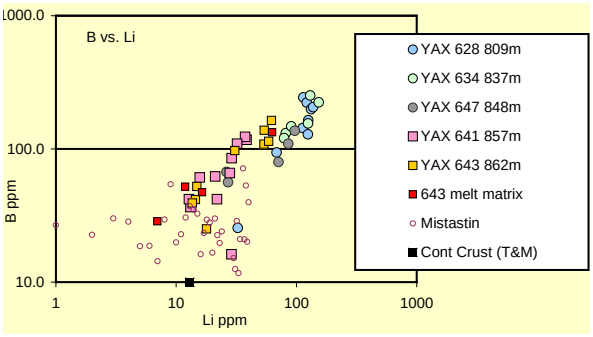

Fig. 1. Boron and lithium abundances in Chicxulub Yaxcopoil matrix clays. The correlation is consistent with fluid mobile behavior of these elements.

Yaxcopoil 1 drill core: The Yaxcopoil-1 (YAX) drill hole is located in the annular trough, about 70 km southwest of the crater center. The Yaxcopoil samples are from an interval less than 50 m thick within the ~ 100 m thick impact melt bearing layers. Matrix clays in thin sections from crater drill cores were analyzed for major elements using a JEOL 8200 EMP, and trace elements Li, B, Be, and Ba were measured with the Cameca IMS 4f ion probe [1]. The concentrations of the elements Li, B, and Be in the alteration material from the matrix of the impactite are enriched upward in the impactite sequence from Unit 5 to Unit 2, as represented by samples from 862 m to 809 m depth, by factors of 3.5 (Li), 2.2 (B) and 1.5 (Be). The correlation between B and Li is consistent with transport of these fluid-mobile elements (**Fig. 1**). The mobile elements Cs, Au, Rb, and Zn are enriched upward in the bulk analyses of Tuchscherer et al. [2]. Barium is depleted upwards in the section, but the formation of barite in the impact breccias probably depleted the Ba concentrations in the fluids and therefore in the altered matrix materials in the upper units.

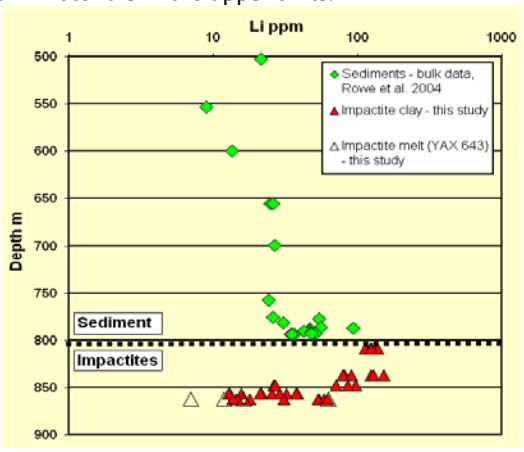

Fig. 2. Lithium as a function of depth in samples analyzed by Newsom et al., [1] and in sediment samples analyzed by ICP-AES [3].

The possibility that vertical transport of mobile elements in the YAX-1 core is due to a post-impact hydrothermal system is supported by the upward enrichments observed in the impactite section, and is consistent with the observed enrichments of mobile elements including Li and Be (**Fig. 2**) in the sediments immediately above the impact breccias analyzed by Rowe et al. [3]. Quantitative consideration of the mass of the mobile elements in the impact melt, the impact breccias and in the overlying sediments suggests that only a small fraction of the mobile elements from the impactites were deposited in the sediments directly above the impact breccias. However, the mobile elements in the sediments do not have to originate in the underlying impactites, but could have been supplied from a different nearby location, including the melt sheet at the center of the crater.

The limited fractionation of Li and B in the altered materials (**Fig. 1**) provides information on the temperature of the fluids involved in the formation of the late-stage altered matrix materials. Based on experimental data from the literature, the similar fractionation of Li and B in the impactites is consistent with a relatively low temperature hydrothermal system during the formation of the altered matrix materials (< 150 ^{o}C). The thin melt sheet at the Yax-1 location, and low temperature of the fluids implied by the trace element data may imply that only limited transport of mobile elements has occurred at this location away from the primary melt sheet within the transient cavity.

Lonar crater floor drill core samples: There is no strong evidence for vertical transport of Li, Be, B, and Ba, in samples from beneath the floor of the small Lonar crater, in spite of the evidence for the presence of post-impact hydrothermal alteration (Newsom et al.,[5]). However, the large scatter in the data, with for example, both B and Li varying by two orders of magnitude may be a result of local transport of these elements by hydrothermal fluids. This lack of evidence for vertical transport stands in strong contrast to our data from the Chicxulub drill core.

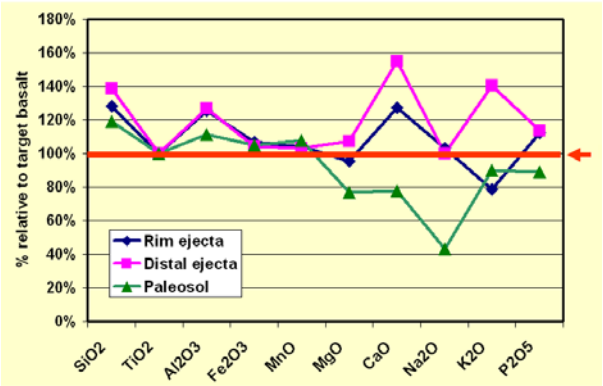

Fig. 3, Major element chemical composition of Lonar materials, compared to target rock basalt (arrow). The materials analyzed by XRF include ejecta from the rim of the crater (n=30), distal ejecta (n=9), and paleosol samples (n=8), normalized to unaltered target basalts (n=18).

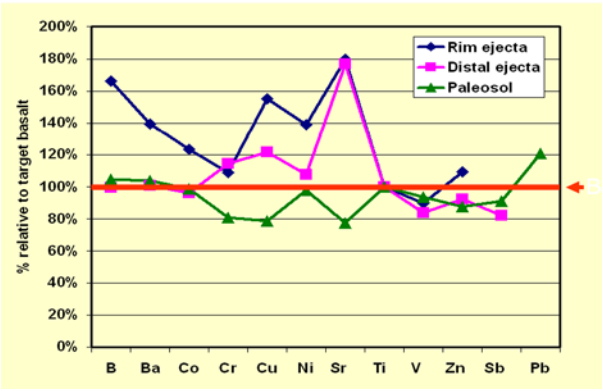

Fig. 4, Minor and trace element composition of Lonar materials obtained by ICP, compared to target rocks and impact melts. The materials analyzed include ejecta from the rim of the crater (n=8), distal ejecta (n=3), and paleosol samples (n=6), normalized to unaltered target basalts (n=6).

Lonar eject blanket studies - The ejecta blanket at Lonar extends beyond 1350 m from the rim with discontinuous patches as far as 3000 m. The large number of accumulating analyses of ejecta blanket materials is being used to address the nature of the alteration and chemical transport in different portions of the ejecta blanket. Samples have been analyzed by XRD and ICP at the University of New Mexico and in India [5]. The geochemical data for the basaltic samples in this study have been normalized to the relatively immobile element titanium. There are interesting differences between the four types of materials compared here (**Figs. 4, 5**). The ejecta samples and paleosol samples are not identical to the target basalts, with the largest difference being a depletion of Na. In contrast, the ejecta samples are not depleted in Na, but are enriched in some elements. Both groups of ejecta are enriched in Si, Ca, K, and Sr, while the proximal rim ejecta is also enriched in B, Ba, Cu and Ni.

Interpretation: The paleosol samples from several areas around the crater represent a much more advanced state of chemical evolution than the ejecta samples, which are probably much younger. The contrasting chemistry of the ejecta suggests a much less advanced state of alteration, but still representing a substantial difference from the target rocks. The physical process of creating the large volume of fine-grained matrix material present in the ejecta may be the most important aspect of promoting chemical alteration by aqueous processes. The presence of caliche, a carbonate-rich material at the base of the impact deposits, supports the role of leaching and chemical transport. Clearly some alteration and transport under ambient conditions has occurred. In terms of possible hydrothermal effects, the enrichments of B, Ba, and Cu in the proximal rim ejecta and not in the distal is intriguing.

Conclusions: Our studies suggests that the Chicxulub impactites away from the central melt sheet experienced low-temperature hydrothermal processing, and limited transport of some elements, including Li, Be and B. At Lonar crater, there is little evidence for any chemical transport, although some modification of the ejecta by enrichment of Si, Ca, K, and Sr may have occurred. This type of information provides constraints on future modeling of the nature of aqueous and hydrothermal processes for craters of different sizes.

References [1] H.E. Newsom et al., (2006) *MAPS 41*, 1921-1949. [2] M.G. Tuchscherer et al. (2004), *MAPS 39*, 899-930. [3] Rowe et al., *MAPS 39*, 1223-1231. [4] H.E. Newsom et al. (2005) *Lunar Planet Sci. XXXVI*, #1143. [5] S. Misra et al. (2006) *LPSC 37th*, # 2123. Supported by NASA P.G.&G. NNX 08AL74G.

FLUID-EVAPORATION RECORDS PRESERVED IN MERIDIANI ROCKS. M. N. Rao[1] , L. E. Nyquist[2] and S. R. Sutton[3], [1]ESCG-Jacobs, Johnson Space Center, Houston. TX. 77058; [2]ARES, Johnson Space Center, Houston. TX. 77058; [3]Department of Geological Sciences and CARS, University of Chicago, Chicago. IL. 60637.

Introduction: We have shown earlier that the high SO_3 / Cl ratios found in secondary mineral assemblages in shergottite GRIM glasses (Gas-Rich Impact-Melt) likely resulted from interactions of regolith materials with sulfate-rich (and Cl-poor) solutions [1,2]. The low SO_3/Cl ratios determined in secondary salts in nakhlite fracture-fillings presumably formed by rock interactions with chloride-rich (and SO_4-poor) solutions near Mars surface [1,2]. The SO_3 and Cl abundances determined by APXS in abraded rocks (RAT) from Endurance, Fram and Eagle craters indicate that these salt assemblages likely formed by evaporative concentration of brine fluids at Meridiani [3,4]. The SO_3/Cl ratios in the abraded rocks are examined here, instead of their absolute abundances, because the abundance ratios might provide better guide-lines for tracking the evolution of evaporating fluids at Meridiani. The SO_3/Cl ratios in these samples, in turn, might provide clues for the mobile element ratios of the altering fluids that infiltrated into the Meridiani rocks.

The absolute SO_3 and Cl abundances in these rock samples depend on the modal abundances of the mobile element-bearing phases such as sulfate and chloride and mobile element poor phases such as silica and hematite in a given rock volume analysed by APXS. Differential occurrence/mixing of accessory mineral phases (phase-mixing) in one sample relative to another in the rock could lead sometimes to random variations in elemental concentrations of the salts. Furthermore, unknown geometry effects during sample measurements by APXS could lead to apparent variations in the real salt content of a given sample.

Here, we study the inter-relationships between the major anions (SO_4, Cl and Br) and cations (FeO, CaO and MgO), using elemental abundances determined by APXS, in abraded rocks at Endurance, Fram and Eagle craters with a view to characterize the composition and behavior of the fluids that infiltrated into these rocks.

Experimental: Mobile element abundances in salt assemblages in abraded Meridiani rocks (RAT) as determined by APXS are taken from [3-6].

Results and Discussion: ***Sulfate-Chloride system***. SO_3 and Cl abundances determined on abraded Meridiani rocks [3-6] are plotted as SO_3/Cl versus Cl in Fig.1.

The concentrations of conservative ions in the evaporating solutions increase in such a way that their ratios remain constant as water is removed from the system. Further, their relative abundances vary along a staright line prior to the onset of insoluble salt precipitation. That is, in the case of conservative elements such as S, Cl and Br, when we plot Cl along the ordinate and the SO_3/Cl ratios along the abscissa, the data points might yield a smooth curve (slope convex downward) (Fig.1), suggesting a possible hyperbolic distribution [7,8]. Data points for 20 rocks and outcrops (RAT) from Eagle, Fram and Endurance craters at Meridiani are ploted in Fig.1. The data points are fitted by a hyperbolic function of the type, $(SO_3/Cl)_m = p / Cl + q$, using the Sigma Plot TM Software. Here, the x-variable is is (Cl)m and the y-varaible is $(SO_3/Cl)_m$. The property of this relationship is that it allows a transformation into a staright line by plotting the x-coordinate as inverse of Cl-abundance, i.e. $1/(Cl)_m$, shown in Fig.2. The goodness of fit for the plotted data points in Fig. 2 provides a test for the validity of the assumption that SO_3 and Cl behave conservatively in acidic solutions on Mars. The SO_3/Cl and Cl data plotted in Fig.2 fit to a straight line ($r^2 = 0.97$). This data-fit indicates that the sequence of evaporative concentration in solutions bearing sulfates and chlorides at Endurance, Fram and Eagle had taken place in an orderly progression (not random precipitation of salts with these anions).

Chloride-Bromide system. Cl and Br behave as conservative tracers in Martian fluids [1,2]. This inference is based on the results obtained by comparing Cl and Br abundances in salt assemblages in nakhlites with those obtained from abraded rocks (RAT) at Meridiani [1-4]. Martian meteorites revealed that the salt assemblages in Nakhla yield high Br (~250 ppm) and low Cl/Br ratios (~10-15) suggesting that salt formation took place from relatively concentrated fluids belonging to advanced satges of evaporation on Mars. On the other hand, Lafayette iddingsite [1, 2] yielded low Br (~11 ppm) and high Cl/Br ratios (~250-300) indicating salt formation from relatively dilute solutions related to early evaporation stages. Furthermore, the halogen ratios in these Martian meteorites are consistent with the petrographic evidence recording the sequential deposition of secondary mineral phases, i.e. carbonate-sulfate-halite, preserved in nakhlite veins during evaporative concentration of brine fluids on Mars [1,2].

As in the case of Figs. 1 and 2, we plot the Cl/Br vs Br (figure not shown) and Cl/Br vs 1/Br (Fig.3) for the same set of rocks (only above the Whatanga contact) at Meridiani. The nomenclature used for these rocks in Figs. 2 and 3 are same as in the case of [3,4]..

The data points of Cl/Br plotted against Br (figure not shown) for Meridiani abraded rocks above the Whatanga contact yield a hyperbolic distribution which is transformed into a staright line (r^2=0.94) on plotting Cl/Br versus 1/ Br in Fig.3. This result reaffirms that the chloride and bromide in the fluids that gave rise to these evaporite salts in Meridiani rocks behaved conservatively. This behavior is similar to that of the sulfate-chloride system in these rocks. Such closely-coupled chemical behavior between these three anions could perhaps be achieved only in fluids that are fairly acidic in character.

FeO/CaO/MgO – SO_3/Cl system: The abundance profiles of CaO/MgO and FeO/MgO ratios with respect to SO_3/Cl in the abraded Meridiani rocks (Fig.4) are quite similar to one another suggesting that divalent Fe likely precipitated as sulfate similar to Ca (figure not shown) from the infiltrating fluids on the Meridiani rocks. These results further suggest that the Fe^{2+} might have later oxidized to Fe^{3+} at Meridiani. Furthermore, application of the "geochemical divide" principle [9,10] to the results obtained here suggests that the Fe^{2+} / SO_4 > 1 in these fluids before the onset of progressive evaporation.

References: [1] Rao M. N. et al. (2005) *JGR, 110*, E12SO6, doi: 10.1029/2005JE002470. [2] Rao M.N.etal.(2008)JGR,113, doi: 10.1029/2007JE002958. [3] Clark B. C. et al. (2005) *Earth Planet. Sci. Lett., 240*, 73-94. [4] McLennan S. M. et al., (2005) Earth Planet. Sci. Lett., 240, 95-121. [5] Gellert R. et al. (2006) *JGR, 111*, doi: 10.1029/2006JE002555. [6] Reider R. et al. (2004) *Science, 306*, 1746-17949. [7] Langmuir C. H. et al. (1978) *Earth Planet. Sci. Lett., 37*, 380-392. [8] Faure G. (1998) Principles and Applications of Geochemistry, Prentice-Hall, 600pp. [11]. [9] Hardie L. A. and Eugster H.P. (1970) *Mineral. Soc. Am. Spec. paper*, *3*, 273-290. [10] Eugster H. P. and Jones B. F. (1979) Am. J. Sci. 279, 609-631.

Figures and Captions :

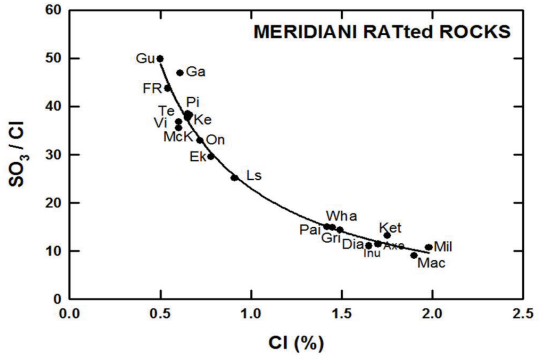

Fig. 1. SO_3/Cl vs Cl on abraded rocks (RAT) from Meridiani (Endurance, Eagle and Fram craters).

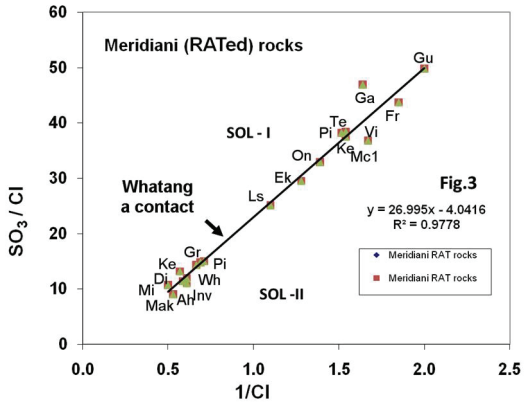

Fig.2. SO_3/Cl vs 1/Cl plot for Meridiani (RAT) rocks

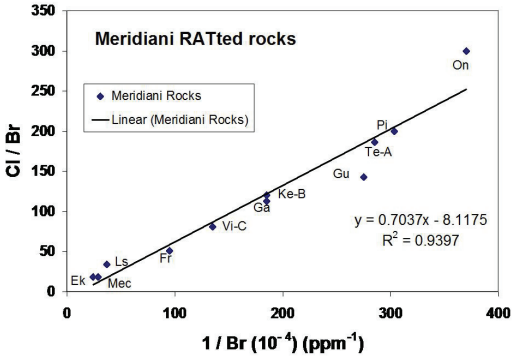

Fig.3. Cl/Br vs 1/Br plot for Meridiani (RAT) rocks

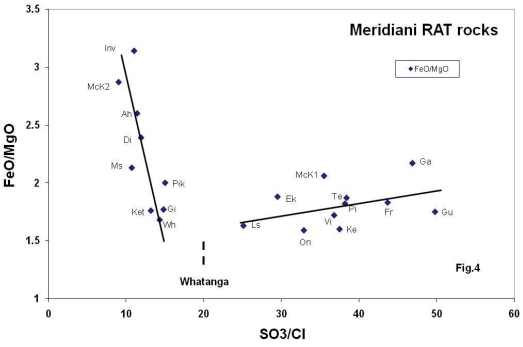

Fig.4. FeO / MgO vs SO3 / Cl plot for Meridiani (RAT) rocks

GEOCHEMICAL MODELS OF REACTIONS OF SEAWATER AND METEORIC WATER WITH BASALT AND PERIDOTITE. Mark H. Reed, and James Palandri, Department of Geological Sciences, University of Oregon, Eugene, Oregon 97403-1272, mhreed@uoregon.edu, palandri@uoregon.edu.

Introduction: Reaction of seawater with basalt produces the most common hydrothermal fluid on Earth–a fluid that is characteristic of hot springs along the entire mid-ocean ridge system and in most submarine springs of island arc volcanoes. Such reaction dramatically changes the original seawater and strictly controls fluid composition, providing an excellent example of the critical role of rock reaction in fixing fluid composition, most notably pH and redox state. Seawater-basalt-derived fluids transport large quantities of copper, zinc and iron to sulfide mound and chimney deposits on the sea floor and to scales that clog geothermal power plant pipes with chalcopyrite, bornite, covellite, sphalerite and pyrite as in Kyushu [1] and Iceland [2].

Reaction of seawater with submarine peridotite produces fluids that are quite alkaline [3] relative to those from basalt reaction, and which provide an instructive comparison to basalt-derived fluids. Reactions of basalt and peridotite with meteoric waters in subaerial geothermal systems yield fluids that are quite distinct in pH and redox conditions from those originating from seawater.

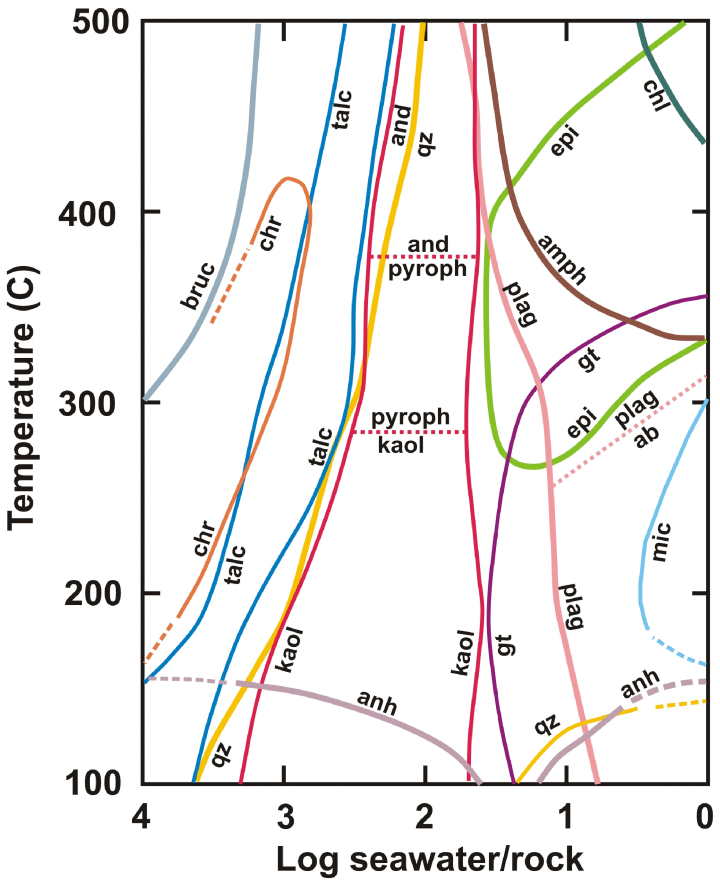

Figure 1. Mineral distribution from reaction of seawater with an Icelandic basalt. Each curve shows a boundary wherein the mineral is present on the side of the curve where the mineral name is given, but absent on the other side. Mineral abbreviations are given in the text. The graph summarizes separate model runs at nine temperatures, each of which was run at w/r ranging from $>10^4$ to 1. The phase boundary geometries are approximate where curves for several phases with components in common intersect in a small area.

Using calculations of multiphase equilibria with program CHILLER [4] or its new offspring CHIM-XPT, we explore basalt and peridotite reactions from moderate temperature to little-explored temperatures up to 500°C as a basis for understanding hydrothermal fluids from deep ocean hot springs and subaerial volcanic settings where meteoric waters dominate. For both the seawater and meteoric water reactions, a focus on temperatures exceeding 350°C is of direct value in modeling the likely fluids to be encountered in the ongoing Icelandic Deep Drilling Project, where one goal is the examination of *in situ* supercritical fluids and their rock environment.

Seawater and fresh water reaction with basalt: We computed seawater-basalt reaction at nine temperatures between 100°C and 500°C and a range of water/rock ratios (w/r) from $>10^4$ to 1. In seawater-basalt reaction, the dominant effect at T≥400°C, as at lower T, is the production of acid (H^+) by precipitation of chlorite, driven by reaction of seawater Mg^{2+} with Al and Si from the basalt, yielding minimum pH's of 3.8 at 400° and 500°C. As at lower T, the acidic conditions enable dissolution and transport of Fe, Cu and Zn, but the higher temperatures enable more than an order of magnitude larger concentrations of the metals than at T≤300°. At every temperature, aqueous Cu and Zn concentrations are limited by precipitation of sulfides, which form from sulfide produced by reduction of seawater sulfate as ferric

iron minerals precipitate. Although a modest amount of H_2 forms, H_2S is the dominant reduced aqueous species at low w/r, in contrast to other systems described below. With decreasing w/r, the pH increases to the neutral range after Mg^{2+}-based buffers fail causing feldspars, epidote and amphiboles join the mineral assemblage. The reaction produces the characteristic mineral assemblages known from meta-basalts and meta-andesites world wide, including combinations of chlorite, epidote, quartz, albite, calcite, garnet, actinolite and clinopyroxene, among others, e.g. [5]. The computed mineral assemblages are depicted in Figure 1, which is a summary of results from the nine individual model runs. The general pattern of brucite and Mg-silicates (chl, chr, talc), at high w/r yielding to Ca-silicates with decreasing w/r reflects the pH trend from acidic to neutral as described above.

In meteoric water reaction with basalt at T≥300°C, the small initial concentration of Mg^{2+} precludes the acidic pH's of the seawater reaction and pH climbs from 5.5 to 7.5 with decreasing w/r. Metal concentrations remain relatively small, but substantial H_2 forms, although much less H_2 than in peridotite reaction.

Seawater and fresh water reaction with peridotite: In contrast to the seawater-basalt reaction, seawater-peridotite reaction yields no acidic pH's at any temperature explored up to 500°C (e.g. pH ranges from 5.2 to 8.1 at 500°C and 5.2 to 7.8 at 300°C) because brucite and Mg-silicates buffer pH at neutral values at the elevated Mg^{2+} concentrations of seawater. Reduction of seawater sulfate yields sulfide which precipitates Cu and Co in sulfide minerals, holding aqueous metal concentrations very small at the alkaline pH's of the system. At every T, coupled reduction of H_2O and oxidation of ferrous iron where magnetite precipitates yields abundant H_2 – two orders of magnitude more than in seawater-basalt reaction at 500°C, and far more H_2 than H_2S.

Fresh water-peridotite reaction yields a typical serpentinite assemblage, as for the seawater reaction, but pH is much higher, ranging up to pH 11 (300°C). H_2 concentration is similar to that in the seawater reaction.

Boiling and cooling: Hydrothermal fluids cool or boil as they rise to the surface, resulting in pH changes as shown in Figure 2. In general, pH decreases with decreasing temperature in the seawater systems, but remains relatively constant and about 4 units higher in the fresh water systems.

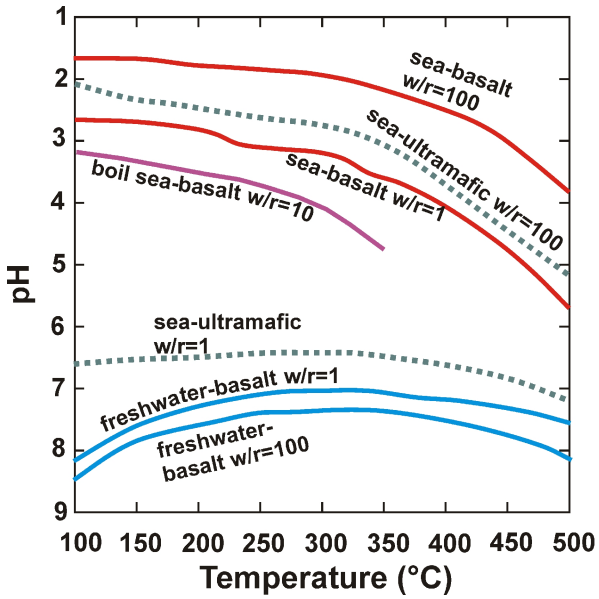

Figure 2. pH *vs* temperature for cooling of fluids derived from reactions of basalt and peridotite. Boiling of a seawater-basalt-derived fluid is also shown. The pH path for boiling of a freshwater basalt fluid at w/r=10 is quite close to the curve shown above for simple cooling of the w/r=100 freshwater-basalt fluid.

Mineral Abbreviations: ab, albite; amph, amphibole (actinolite, riebeckite); and, andalusite; anh, anhydrite; bruc, brucite; chl, chlorite (Fe-Mg solid solution); chr, chrysotile; epi, epidote; gt, garnet (grossular, andradite); kaol, kaolinite; mic, microcline; mt, magnetite; plag, An(30); pyroph, pyrophyllite; qz, quartz.

Acknowledgements: We thank Megan Smith for assistance with computing acknowledge funding from NSF EAR-0507181.

References:

[1] Akaku, K., Reed, M.H., Yagi, M., Kai, K. and Yasuda, Y., 1991, Geochemical Journal, 25, 315-334. [2] Hardardóttir V., 2004, in Wanty, R.B. and Seal, R.R., II eds., Proceedings of the 11th Symposium on Water-Rock Interaction: Leiden, Netherlands, A.A. Balkema, p. 1521-1525. [3]Kelley D. S., Karson J. A., Blackman D. K., Früh-Green G. L., Butterfield D. A., Lilley M. D., Olson E. J., Schrenk M. O., Roe K. K., Lebon G. T., Rivizzigno P. A., and Party A.-S. (2001), Nature 412, 145-149. [4] Reed, M.H., 1998, Chapter 5, in J. Richards, and P. Larson, eds., Techniques in Hydrothermal Ore Deposits Geology, Reviews in Economic Geology, Volume 10, p. 109-124. [5] Schiffman, P., and Smith, B., Journal of geophysical research, 93, 4612-4624.

TIME DEPENDENT MODEL FOR HEAT TRANSFER AND WATER VAPOR DIFFUSION/ ADSORPTION AT THE PHOENIX LANDING SITE. E. G. Rivera-Valentin[1], V. F. Chevrier[1], and R. Ulrich[2], [1]Arkansas Center for Space and Planetary Sciences (eriverav@uark.edu), [2]Dept. of Chemical Engineering, University of Arkansas Fayetteville

Introduction: The recent Phoenix mission has given us many insights into the Martian polar climate and the dynamics of the water cycle. This new set of data can now be used to further constrain models of various processes affecting these dynamics and to find the limitations of previous models.

As seen in Fig. 1, diurnal vapor pressure recorded by the Thermal and Electrical Conductivity Probe (TECP) shows systematic variations by about 2 orders of magnitude [1]. The GCM (Global Circulation Model) does not predict such fluctuations in humidity, but rather a nearly constant pressure [2]. Since the GCM model does not take into account atmospheric interactions with the regolith, we may infer that the shortcomings of this model in this polar region implies that such interactions are significant [1,3].

Possible processes that may account for such a coupling include adsorption onto regolith grains as well as hydration of perchlorate salts [1,3] or equilibrium with liquid [4].

In a first step, we investigate the effect of adsorption as a potential sink for water vapor [5,6]. We are creating an integrated numerical model that accounts for both heat and mass transfer of water vapor in the regolith, including the effect of adsorption [5]. Using this model, we can simulate the effect of adsorption on humidity and attempt to relate this to Phoenix observations.

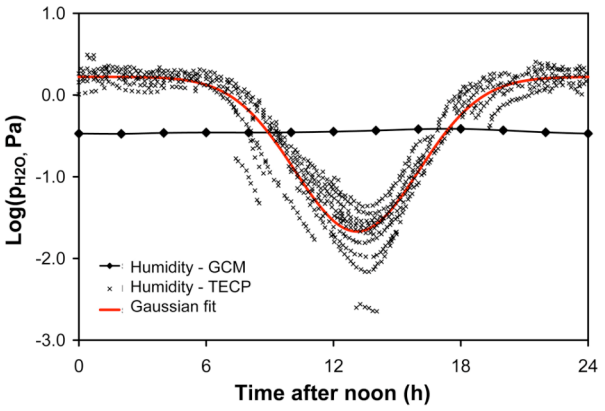

Fig. 1: Water vapor pressure at the Phoenix landing site [1], compared to the results from the GCM model. The red curve is a Gaussian fit of the data.

Methods: To model heat transfer, water vapor diffusion, and adsorption in the regolith, we use COMSOL Multiphysics, which is a program allowing for the simultaneous solution and simulation of multiple differential equations describing various physical processes. The diffusion/adsorption and heat transfer models were created separately then merged into a transient temperature dependent diffusion/adsorption model. We especially focus on the kinetics of the various processes and their variations with temperature. Most other models focus on longer timescales where adsorption can be averaged [7]. This though is based on the cyclicity of the adsorption process and the assumption that the process occurs instantaneously. However, recent studies have shown that slow adsorption kinetics can strongly affect the diffusion of water vapor [5]. Thus, the study of water behavior at short timescales (days or weeks) requires the inclusion of the adsorption kinetics and the detailed study of the transient effects.

Heat Flux Model: We primarily use the equation set proposed by multiple authors to model the heat flux incident on the Martian surface to reproduce diurnal temperature changes [8,9,10]. We take into account the diffusion of the direct solar beam, the indirect solar illumination due to scattering, and thermal emission of the atmosphere as follows:

$$Q_{DB} = I_{sun}(1-A)\cos(z)T(z,\tau) \quad (1)$$

$$Q_{scat} = \left(I_{sun}\left(1 - e^{-\frac{\tau}{\cos(z)}}\right) - I_{ab} \right)(1-A)f_{scat} \quad (2)$$

$$Q_{atm} = I_{sun}\,\varepsilon\, f_{atm}\cos(\delta - \varphi) \quad (3)$$

where I_{sun} is the solar flux received at any given position in Mars' orbit, I_{ab} is the amount of solar flux absorbed by the atmosphere, A is the surface albedo, z is the zenith angle, τ is the opacity of the atmosphere, $T(z,\tau)$ is the transmission coefficient derived from Pollack (1990) and shown by Rapp [11], f_{scat} and f_{atm} are fractions of flux provided by Schmidt *et al.* [8], ε is thermal emissivity of the atmosphere, δ is the solar declination, and φ is the latitude. We also include geothermal heat flux from below assigned as 30×10^{-3} W/m^2 [10].

We construct a geometry representative of a layer of regolith 1 m in width and z meters in depth. Ulrich *et al.* suggest a regolith density of 2000 kg/m^3 [10]. Considering the unconsolidated nature of the regolith found at the Phoenix landing site, we use a lower rego-

lith density of 1200 kg/m^3. For the preliminary model, we use the heat capacity and thermal conductivity stated by Ulrich *et al.* of 800 J kg^{-1} K^{-1} and 0.1 W m^{-1} K^{-1} [10]. Since the TECP collected data on both the heat capacity and thermal conductivity of the Phoenix landing site and Zent *et al.* found that there exists a linear relationship between these properties and temperature [12], we will include these data in the later model to better simulate the Phoenix landing site.

Mass Transfer Model: We use the adsorption and diffusion equations provided by Chevrier *et al.* with minor updates [5]. As stated by Chevrier *et al.*, the differential equation for the transport of water vapor allowing for simultaneous diffusion and adsorption in the Martian regolith is:

$$\frac{\partial p}{\partial t}\left[1+\Psi\frac{\partial \theta}{\partial p}\right]=\frac{\partial D}{\partial z}\frac{\partial p}{\partial z}+D\frac{\partial^2 p}{\partial z^2} \quad (4)$$

where p is the partial pressure of water vapor, Ψ is a constant that corresponds to the thermodynamic part of the adsorption process and is defined as:

$$\Psi=\frac{RT_s\rho_{H20}\rho_{reg}A_s l}{M_{H2O}} \quad (5)$$

where R is the ideal gas constant, T_s is the temperature of the surface, ρ_{H20} is the density of water, ρ_{reg} is the density of the regolith, A_s is the specific surface area of the regolith, l is the thickness of the adsorbed water monolayer, and M_{H2O} is the molecular weight of water. The diffusion coefficient, D, is calculated as follows:

$$D=1.387\times10^{-5}\left(\frac{T}{273.15}\right)^{\frac{3}{2}}\left(\frac{1.013\times10^5}{P_{tot}}\right)\left(\frac{\phi}{q}\right) \quad (6)$$

where T is the temperature, P_{tot} is the total pressure, ϕ is the regolith porosity, and q is the tortuosity. The model will be tested with and without an ice table to precisely study the contribution of sublimating ice. We will scale z to observed values of ice table depth (i.e. 6 to 16 cm [13]).

Results: At this moment, we have fully developed the heat flux model. We show in Fig. 2 our model predicted temperature at the surface of the regolith versus the observed diurnal temperature change at the Phoenix site. Our model maximum temperature is ~ 244 K and minimum temperature is ~ 198 K compared to the maximum and minimum temperatures recorded at the Phoenix site of 253 K and 181 K respectively [12].

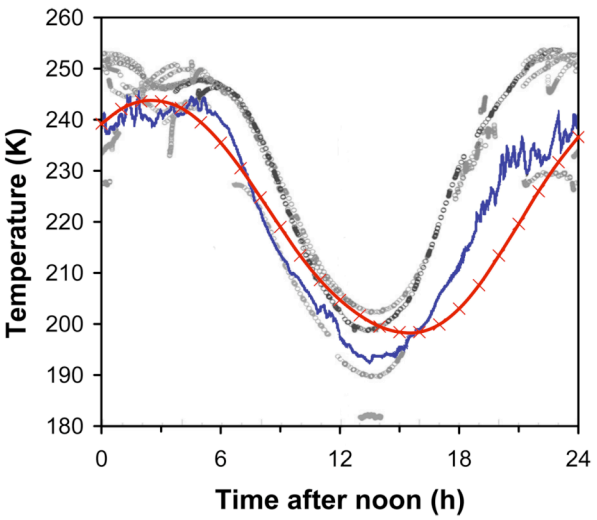

Fig. 2: Numerical model of temperature evolution at the Phoenix landing site (red), compared to data from the MET instrument 2 meters above the surface (blue, [1]) and data from the TECP in the soil (grey and black circles [12]).

Overall, our model provides a relatively good estimate of the temperature. The only significant difference is that our model predicts a temperature about 10 K lower during the evening. Further refinement of the parameters in the model should take care of this issue. As of this article, preliminary results for the mass transfer model are not available.

Conclusion: As can be seen from Fig. 2, our predicted temperatures correlate well with Phoenix observations. Our deviation from observations in general is ~ 13 K. Our predicted temperature profile at a given regolith depth in our geometry also matches well with Ulrich *et al.* [4].

By simulating the mass transfer process at the Phoenix landing site, our model will help in understanding the observed vapor pressure variations. In addition, we will make a versatile model that will also include phase change and thus help determining if liquid water can form under present-day conditions.

References: [1] Hudson, T. L. et al. (2009) *LPS XL*, Abstract #1804. [2] Forget, F. et al. (1999) *JGR, 104,* 24155-24175. [3] Hecht, M. H. et al. (2009) *LPS XL*, Abstract #2420. [4] Hanley et al. (2009) *LPS XL*, Abstract #1380. [5] Chevrier, V. F et al. (2008) *Icarus, 196*, 459-476. [6] Zent, A. P. (2001) *JGR, 106,* 14667-14674. [7] Schorghofer, N. et al. (2005) *JGR, 110,* E05003. [8] Schmidt, F. et al. (2009) *Icarus,* doi:10.1016. [9] Applebaum, J. et al. (1993) NASA Technical Memorandum 106321. [10] Ulrich, R. et al. (submitted) *Astrobiology*. [11] Rapp, D. **Human Missions to Mars Reality or Fantasy**, Vol. 2**.** [12] Zent, A. P. et al. (2009) *LPS XL*, Abstract #1125. [13] Mellon, M. T. et al. (2009) *LPS XL*, Abstract #1904.

GUSEV-STYLE ALTERATION: UNIQUE OR UBIQUITOUS ON MARS? Steven W. Ruff[1], [1]School of Earth and Space Exploration, Arizona State University, Tempe, AZ 85287-6305, steve.ruff@asu.edu.

Introduction: Evidence for hydrous alteration on Mars has in recent years become unequivocal. The identification by a combination of orbital and landed instruments of water-derived hematite, sulfates, phyllosilicates, Fe-oxides, and hydrated silica is robust. Even carbonates are now recognized [1, 2]. In some cases, it is possible to ascertain an environmental context for the alteration.

Gusev Crater, which is still being explored by the *Spirit* rover more than five years after its arrival, displays a range of altered materials and secondary phases. Sulfates, Fe-oxides, phosphates, and hydrated silica have been identified using a combination of measurements from the Alpha Particle X-ray Spectrometer (APXS), Mössbauer spectrometer (MB), and Miniature Thermal Emission Spectrometer (Mini-TES). No phyllosilicates have been identified definitively. Most enigmatic is a phase or phases that resemble an amorphous silicate of basaltic composition [3]. No terrestrial analog has been identified for this material.

Despite a powerful payload and a capable rover platform, the environmental conditions that have produced the range of alteration present in Gusev Crater are not well understood. From this lack of understanding comes an opportunity for modeling. Investigating the conditions that could produce the style of alteration observed in Gusev will lead to a better understanding of the range of hydrous environments across Mars.

Alteration on the Plains: The rocks encountered by *Spirit* on the traverse across the plains to the Columbia Hills are only lightly altered in most cases. The Adirondack-class basalts are the dominant rock type. Their primary mineralogy is that of a picritic basalt, with olivine (Fo_{50-60}) clearly evident in the spectra from Mini-TES and MB [e.g., 4, 5].

Sulfur enrichment identified by the APXS that decreases with depth in the rocks [e.g., 6] recently has been characterized using Mini-TES spectra as a sulfate phase that most resembles kieserite [7]. This sulfate phase is a persistent spectral component among all Adirondack-class basalts observed with Mini-TES across the plains. Twenty-seven examples of these rocks have been identified as "exotics" in the Columbia Hills, likely lofted there by meteorite impacts onto the plains. The exotics also display the same sulfate phase. Combined with the observation that many Adirondack-class rocks have a ventifact morphology indicative of aeolian abrasion, the presence of sulfate at the surface of these rocks may represent an active alteration process that outpaces erosion.

The only unequivocal rock coating on Mars is found on a large (~1 m long) Adirondack-class rock called Mazatzal. A smooth, dark-toned coating is present underneath a layer of loose airfall dust [e.g., 8] (Fig. 1). The coating is spectrally thick to Mini-TES, completely obscuring the substrate. Its spectral features resemble no known terrestrial rock coating [e.g., 9] (Fig. 2). Spectral deconvolution indicates a dominant phase that most resembles basaltic glass [7], i.e., an amorphous silicate of basaltic composition. Remarkably, this unusual coating is formed on a surface clearly "fluted" by aeolian abrasion, an indication that it formed well after the Adirondack basalts were emplaced, broken up, and eroded.

Alteration in the Columbia Hills: Massive and layered outcrops known as Clovis class display clear evidence of alteration. Enrichments in S, Cl, and Br relative to the Adirondack basalts observed by the APXS along with highly oxidized iron (avg. $Fe^{3+}/Fe_T \cong 0.8$) and the presence of goethite identified by the MB [e.g., 10] represent an alteration style unique among the measured Gusev rocks. Mini-TES identified no unambiguous alteration phases. Instead, like the Mazatzal coating, the spectra of these rocks are dominated by an amorphous phase(s) of basaltic composition that departs from recognized basaltic alteration (Fig. 3).

On the north flank of Husband Hill, a large (~5 m long) outcrop spectrally matches the adjacent float rock called Watchtower, which displays an enrichment of P, Al, and Ti relative to Adirondack class and also is highly oxidized and contains goethite [e.g., 10]. Mini-TES spectra again are dominated by an amorphous basaltic phase(s).

In contrast to the Mazatzal coating and altered Columbia Hills rocks is the opaline silica phase identified with Mini-TES and APXS data in many eroded outcrop and soil exposures surrounding the Home Plate feature [11]. This is a readily recognized alteration phase consistent with several terrestrial analog environments.

Summary: Except for the opaline silica occurrences adjacent to Home Plate, the alteration of various rocks and outcrops along *Spirit's* traverse appears to have no recognized terrestrial analog. Mini-TES spectra reveal a dominant phase that most resembles an amorphous silicate of basaltic composition. Perhaps very low water-to-rock alteration over geologic times-

cales is responsible. It is noteworthy that the spectral characteristics of this alteration have not been recognized in global mapping using the Mars Global Surveyor Thermal Emission Spectrometer. But without a dedicated search, it is premature to conclude that such alteration is limited to Gusev Crater.

References: [1] Bandfield, J.L., et al., (2003) *Science, 301* 1084-1086. [2] Ehlmann, B.L., et al., (2008) *Science, 322* 1828-1832. [3] Ruff, S.W., et al., (2006) *J. Geophys. Res., 111*(E12S18) doi: 10.1029/2006JE002747. [4] Morris, R.V., et al., (2004) *Science, 305* 833-836. [5] McSween, H.Y., Jr., et al., (2006) *J. Geophys. Res., 111*(E02S10) doi:10.1029/2005JE002477. [6] Gellert, R., et al., (2004) *Science, 305* 829-832. [7] Hamilton, V.E. and S.W. Ruff, (2009) *Lunar Planet. Sci., XL*([CD-ROM]) abstract #1418. [8] Haskin, L.A., et al., (2005) *Nature, 436* 66-69. [9] Hamilton, V.E., et al., (2008) *J. Geophys. Res., 113*(E12S43) doi:10.1029/2007JE003049. [10] Ming, D.W., et al., (2006) *J. Geophys. Res., 111*(E02S12) doi:10.1029/2005JE002560. [11] Squyres, S.W., et al., (2008) *Science, 320* 1063-1067.

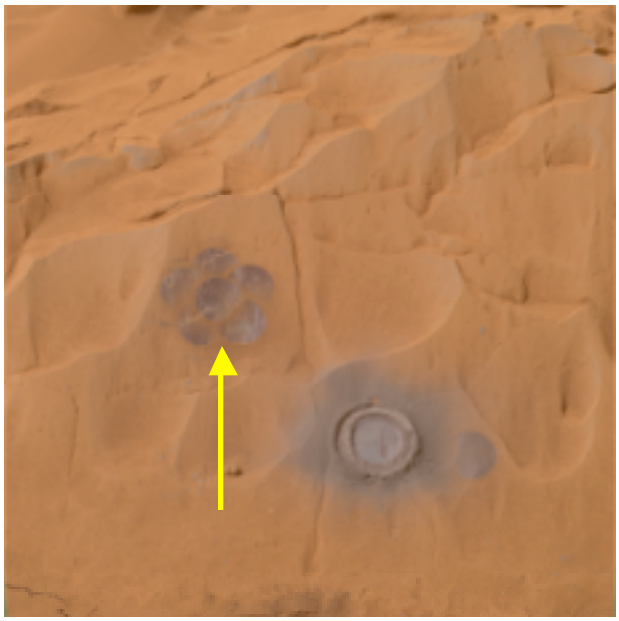

Figure 1. The dark-toned coating on the brushed surface of the rock Mazatzal is the only unequivocal example of a rock coating on Mars.

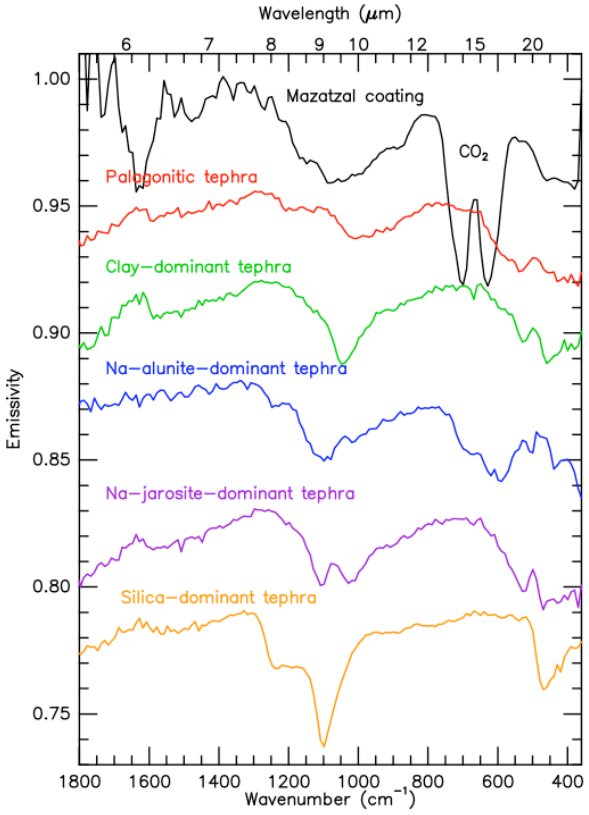

Figure 2. The Mini-TES spectrum of the Mazatzal coating does not match alteration typical of basaltic materials.

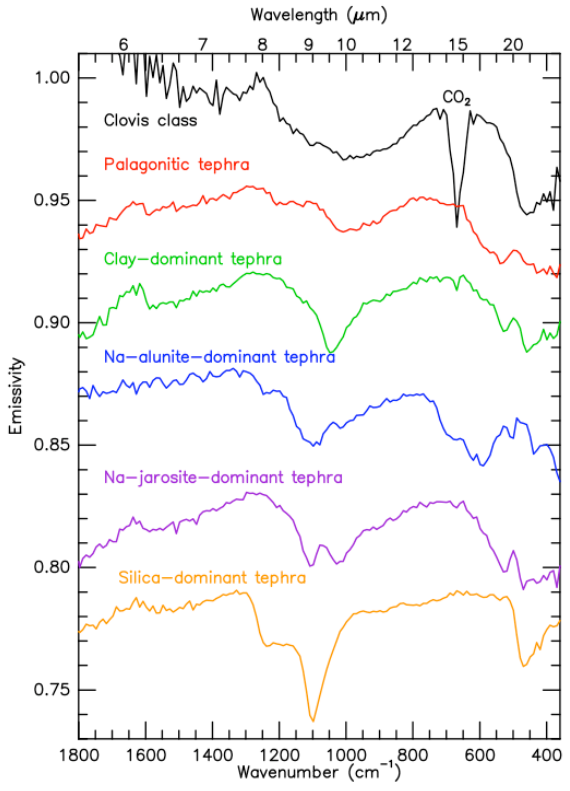

Figure 3. The Mini-TES spectrum of Clovis class rocks does not match alteration typical of basaltic materials.

IMPACT-GENERATED HYDROTHERMAL SYSTEMS IN MAFIC TO ULTRAMAFIC NOACHIAN CRUST ON MARS. S. P. Schwenzer[1] and D. A. Kring[1], [1]Lunar and Planetary Institute, USRA, 3600 Bay Area Blvd., Houston, TX 77058, USA; schwenzer@lpi.usra.edu; kring@lpi.usra.edu.

Introduction: Frequent impacts [e.g., 1-3] reworked the crust of Mars during the Noachian [4]. The energy of those impacts created thousands of prominent heat sources that supported long-lived, deep-reaching hydrothermal systems [5,6]. In this paper, we investigate how those systems altered the chemistry and mineralogy of Noachian crust.

Previous work and motivation for this study: We previously examined secondary minerals formed by the alteration of the plutonic lherzolithic shergottite LEW 88516 [8-9]. As the Martian crust contains diverse lithologies, we extended our calculations to compositions of more feldspathic shergottites (Dhofar 378) and olivine-rich dunites (Chassigny) [10]. Here we present the missing piece: pyroxenitic compositions that are represented by Nakhla, whose chemistry is taken from [11] with FeO/Fe_2O_3 partitioning as suggested by [12]. The initial fluid composition is a Ca-Mg-Fe-brine that is in equilibrium with Nakhla. We also considered a brine with sufficient K^+ to charge balance SO_4^{2-} at a water/rock (W/R) value of unity. Furthermore, we considered a brine with ~5 times this amount of K^+ (and SO_4^{2-}) to evaluate its affect on alteration assemblages. We calculated results for five temperatures: 13 °C (which is the minimum temperature at 1 km depth according to the geothermal gradient of Mars after [13]) and 50 °C for the low temperature part of the system, i.e., the radially most-distant parts of the system beneath the crater at any time and also the last stage of the system before it returns to ambient thermal conditions. The high-T steps are 150, 200, and 300 °C. Figure 1 displays the 150 °C results.

Results: From the pyroxene-rich Nakhla protolith, pyroxene and/or amphibole (re-)precipitates at the lowest W/R values and from all fluid compositions. Nontronite is an abundant product at intermediate W/R values (Fig. 1).

Nakhla alteration vs. that of other protoliths. Alteration at 150 °C (110 bar) and W/R of 1 creates secondary pyroxene ($Dio_{31.9}Hed_{68.1}$) and amphibole ($Rie_{20.4}Trem_{32.7}Act_{46.9}$) accompanied by serpentine, chlorite, and garnet (andradite). At an intermediate W/R of 1000 the dominating phases are hematite and clay (Mg-nontronite), which are accompanied by quartz and pyrite. If the W/R is very high (100000), hematite dominates the precipitate with pyrite and traces of diaspore.

This pyroxene-rich alteration is unlike that produced from other mafic and ultramafic protoliths (Fig. 1). At W/R of unity, 28 wt.-% of the alteration assemblage is iron-dominated pyroxene. At this W/R the olivine-rich Martian rock compositions (LEW 88516, Chassigny) form serpentine as the dominating phase, while a more feldspar- (i.e., Al-) rich composition (Dhofar 378) forms chlorite as the dominating phase. Also, the pyroxene in the Dhofar 378 alteration assemblage is more Ca-rich ($Dio_{41.8}Hed_{58.2}$) than that produced by alteration of Nakhla.

At intermediate W/R, hematite is a major phase produced from Nakhla, similar to that from Chassigny. The pyroxene cumulate, however, also forms abundant clay (Mg-nontronite). These abundances (33 wt.-%) are significant, but less than those formed from LEW 88516 (46 wt.-%) and Dhofar 378 (48 wt.-%).

At W/R = 100000 the system is dominated by two factors: the fluid composition and solubility of the least soluble and/or most dominant elements. With all iron-rich protoliths, these assemblages are dominated by hematite and pyrite. If the protolith has sufficient Al, diaspore forms.

Potassium-enriched starting fluid. At W/R = 1 and 150 °C, pyroxene and/or amphibole dominate the alteration assemblage produced from Nakhla (Fig. 2). The pyroxene composition changes from $Dio_{31.9}Hed_{68.1}$ to $Dio_{32.4}Hed_{67.6}$ and $Dio_{35}Hed_{65}$ with increasing K^+ concentration. The amphibole's tremolite content increases, also, while the actinolite content decreases: $Rie_{20.4}Trem_{32.9}Act_{46.9}$ for a K-free brine, and $Rie_{20.5}Trem_{33.0}Act_{46.4}$ and $Rie_{19.3}Trem_{35.8}Act_{44.9}$ for the K^+-enriched brines, respectively. Serpentine is formed at higher temperatures and mica (Fe-celadonite) takes up K at 150 °C.

At W/R = 1000 and T=13 °C the only difference between the K-free and K-bearing solutions is the nontronite that is formed: Mg-nontronite for the K-free brine and K-nontronite for the K-containing brines. At 150 °C (Fig. 2), Mg-nontronite is the product for all starting fluids and anhydrite precipitates from the brines with the highest K^+ (thus SO_4^{2-}). At 300 °C all three brines form anhydrite, with the amount depending on the SO_4^{2-} content of the solution. All three systems also form hematite as a dominating phase, with the hematite decreasing with increasing K^+ and SO_4^{2-} content (80, 62, and 36 wt.-%, respectively). Serpentine shows the opposite behaviour and increases with increasing K^+ and SO_4^{2-}content (~8 in the first two runs, and 35 wt.-% in the most K^+-rich run).

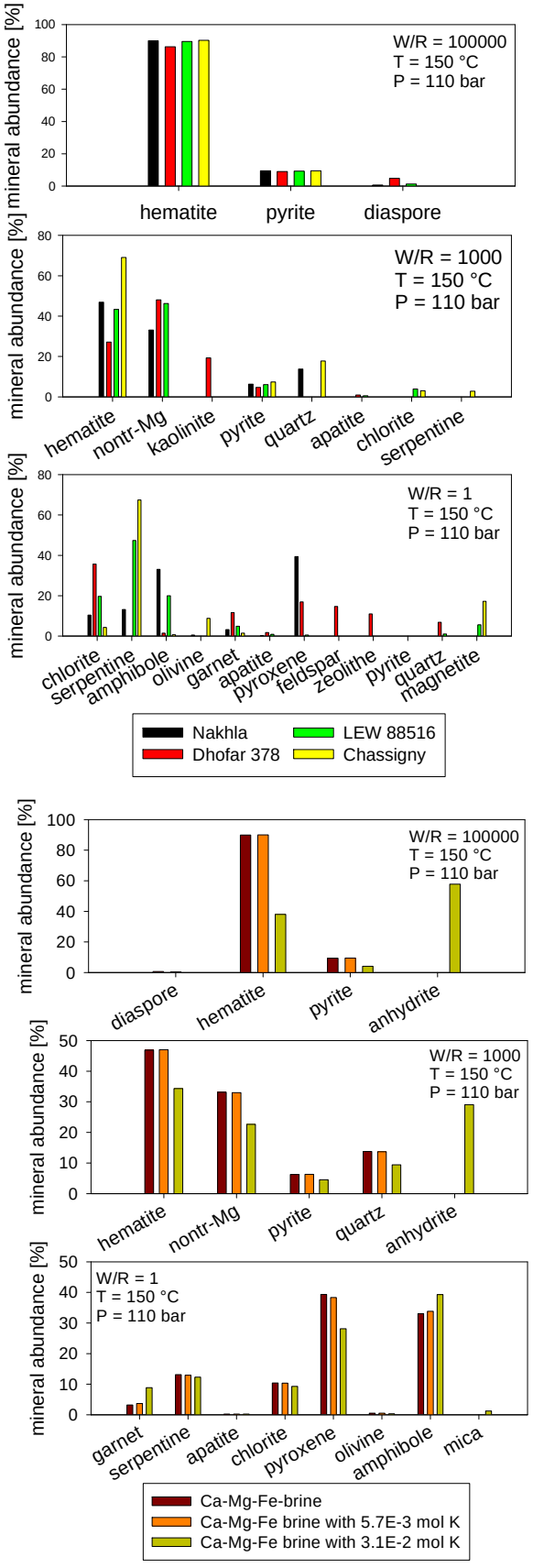

At W/R = 100000 the dominating phase is goethite (13 °C) or hematite (150 and 300 °C). The K ion is bound in nontronite at 13 °C: while the alteration products of Nakhla with our K-free starting fluid form Mg-nontronite, the clay phase is K-nontronite in the calculations with higher potassium concentrations. At higher temperatures K^+ stays in solution; however, the higher SO_4^{2-} concentration causes anhydrite to form where the K^+ (and thus SO_4^{2-}) concentration is highest.

Conclusion: At low W/R, altered pyroxenites form secondary pyroxene and amphibole, rather than the chlorite- and serpentine-rich assemblages produced from other protoliths. Smectite (including nontronite) forms from all mafic and ultramafic lithologies at W/R values of order 10^2. If significant K^+ and SO_4^{2-} occur in the fluid, then anhydrite precipitates at W/R of a few hundred to 100000. Hematite is abundant at the highest W/R values. These alteration assemblages are similar to those deteced by OMEGA and CRISM. We also note that secondary pyroxene may be a product of alteration and, thus, that it may contribute to the total amount of pyroxene found on Mars [14].

References: [1] Tanaka, K. L. et al. (1988) *Proc. LPSC*, **18th**, 665-678. [2] Kring, D.A. and Cohen, B.A. (2002) *J. Geophys. Res.*, **107** (E2), doi: 10.1029/2001JE001529. [3] Strom, R. G. et al. (2005) *Science*, **309**, 1847–1849. [4] Hartmann, W. K. & Neukum, G. (2001) *Space Sci. Rev.*, **96**, 165–194. [5] Rathbun, J.A. and Squyres, S.W. (2002) *Icarus*, **157**, 362-372. [6] Abramov, O. & Kring, D. A. (2005) *J. Geophys. Res.*, **110** (E12S09), doi: 10.1029/2005JE002453. [7] Schwenzer, S. P. & Kring, D. A. (2008a) *LPSC*, **XXXIX**: #1817. [8] Schwenzer, S. P. & Kring, D. A. (2008b) *Workshop on the Early Solar System Bombardment*, Abstr. #3027. [9] Schwenzer, S. P. & Kring, D. A. (2008c) *Workshop on Martian Phyllosilicates: Recorders of Aqueous Processes?* Abstr. # 7014. [10] Schwenzer, S. P. & Kring, D. A. (2009) LPSC, **XL**, #1421. [11] Dreibus, G. et al. (1982) *LPSC*, **XIII**, 186–1872. [12] Treiman, A.H. (2005) *Chemie der Erde*, **65**, 203-270. [13] Babeyko, A. Yu. & Zharkov, V. N. (2000) *Physics of the Earth and Planetary Interiors*, **117**, 421–435. [14] Poulet, F. et al. (2007) *JGR*, **112**, E08S02, doi: 10.1029/2006JE002840.

Figure 1 (top of opposite column). Comparing alteration minerals formed from Nakhla with alteration minerals formed from Dhofar 378, LEW88516, and Chassigny.

Figure 2 (bottom of opposite column). Comparing alteration minerals formed from Nakhla with a K-free Ca-Mg-Fe brine with alteration minerals formed from Nakhla with K-bearing brines.

HYBRID EXPERIMENTAL/THEORETICAL MODELS FOR ACIDIC SULFATE WATERS P. Sobron[1,2], F. Sobron[2], A. Sansano[2]. [1]Dept. Earth and Planetary Sciences and McDonnell Center for Space Sciences, Washington University, St. Louis, MO, 63130 USA (psobron@levee.wustl.edu). [2]Unidad Asociada Universidad de Valladolid-Centro de Astrobiología CSIC-INTA. Paseo Prado de la Magdalena s/n. Valladolid-47011, Spain. (sobron@iq.uva.es; asansano@fmc.uva.es),

Introduction: The discovery of ferric hydroxides/oxyhydroxides, jarosites (iron-bearing sulfates thought to have formed via aqueous activity) and other sulfate-bearing minerals in the Meridiani region provides strong evidence that liquid water once flowed on the Martian surface [1-3]. It is suggested that sulfate deposits enriched in iron and mixed iron oxyhydroxide were precipitated form meltwaters [4], thought to have been acidic.

Terrestrial acidic and sulfate-rich sites such as Rio Tinto and El Jaroso in Spain, Iron Mountain in California, and some lakes in Western Australia are exceptional sites for the study of acidic waters, its associated precipitates and efflorescent salts, and sulfate-forming processes in general in which the presence of microorganisms may be required. The characterization of the hydrogeochemistry of these sites is crucial in order to describe all of the different processes and settings of iron and sulfate deposition on Earth. Further, as these localities host mineralogical signals detected on Meridiani and other sites on Mars, the comparison may help to understand how these minerals formed. It is crucial then to characterize the range of environmental stability for each of these mineral, i.e., to classify the minerals as a function of their precipitation order, or increasing solubility in a given aqueous system. The reverse application of those precipitation models to the current Martian iron sulfate mineral phases will help obtaining a complete picture of the acidic waters that once flooded the planet's surface via describing phase relations in those waters.

In this work we show the investigations on synthetic acidic aqueous systems that mimic the conditions of the natural waters of the Rio Tinto Mars analog site. The physico-chemistry of two synthetic systems of special relevance: iron(II) sulfate- sulfuric acid-water, and iron(III)-sulfuric acid-water, is reported. Additionally, we investigated the mass transport properties of a third system, sulfuric acid-water. These systems are non-ideal multicomponent liquid mixtures whose structure is not known, mainly because there exists a large uncertainty in the available data for the activity coefficients in multicomponent systems. Techniques based on spectroscopy do allow the direct determination of the mole fractions of all components in a mixture. We have developed a procedure for the measurement of the physico-chemical properties of these systems using Raman spectroscopy.

Raman spectroscopy: The wavelength of a small portion of the light scattered from a sample is shifted from the wavelength of the incident light. Furthermore, this shift in wavelength depends only on the chemical bonding responsible of the scattering. Molecular vibrations of a huge number of complexes are determined by specific wavelengths in the Raman spectra. So, in principle, a single Raman spectrum of a sample – which does not have to prepared or damaged- can reveal the molecular structure of it. Chemical composition and abundance of species may also be retrieved from a Raman spectrum upon certain processing.

Results: Accurate quantitative analyses of concentrations of species present in the system iron(II) sulfate-sulfuric acid-water have been achieved, along with the characterization of the equilibriums in this system in terms of the activity coefficients product. This is essential in order to establish physico-chemical models of acid sulfate waters as this particular system turns out to have a highly non-ideal behavior. Additionally, Raman spectroscopy has provided a means to corroborate previous findings on the formation of iron(II) hexahydrate complexes in the mentioned system. The activity coefficients product (Fig. 1) has been calculated as a function of iron(II) sulfate concentration with iron concentrations exceeding Rio Tinto's. The logarithmic relationship between the activity coefficients product and the concentration of iron (II) sulfate found for this system gives an idea of the high non-ideality if this system, and allows to extrapolate values beyond the limits of salt concentrations used in this work.

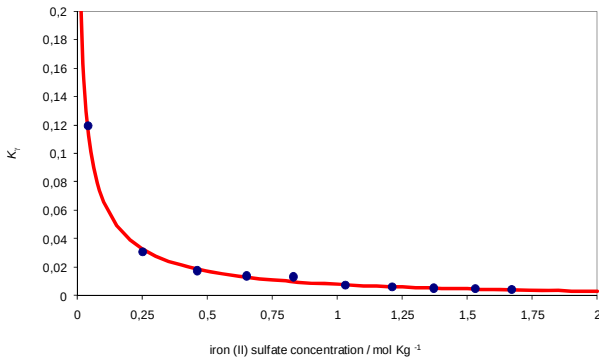

Fig. 1 Activity coefficients product, $K\gamma$ plotted against iron(II) sulfate concentration. Blue dots, experimental; red line, empirical function

The speciation in the iron (III)-sulfuric acid-water system was monitored by Raman spectroscopy, revealing the existence of sulfate-iron(III) interactions in the Fe^{3+} inner sphere through oxygens from the sulfate units and in the outer sphere through hydrogen bonds.

The Raman technique provides the accuracy and repeatability critical for this qualitative and quantitative analysis. Particularly, molecular vibrations of iron(III) complexes are determined by specific wavelengths in the Raman spectra, and intensity and width changes of the Raman bands corresponding to iron(III) complexes molecular vibrations can be quantified very rapidly.

Diffusion of the molecular species within the system sulfuric acid-water has been monitored by Raman spectroscopy (Fig. 2), a thermodynamic-chemical model of the mass transport properties of the species has been established, and its parameters optimized. It has been shown that the non-ideality of this system plays a crucial role in its mass transport properties, which however have been explained in terms of a diffusion model for the multicomponent system. In summary, the diffusion coefficients are not constant (characteristic of ideal systems) but are a function of the concentration of the species in solution. The model has been conceived in such a way that it can be adapted to any multicomponent mixture provided the equilibriums among the ions are known. Raman spectroscopy may provide the means to derive the speciation and concentration of species in multicomponent systems, and thus the model-based measurement of the diffusion properties using Raman is presented as a robust and accurate technique (Fig. 3).

Conclusion and future work: The results presented are just the first stage of the knowledge and advances in the modeling of the aqueous processes in acidic environments, such as those envisaged for early Mars, that can achieved by means of Raman spectroscopic investigations on acid mine drainage-related aqueous systems.

We are currently developing a experimental device that mimic the geometrical and thermal constrains of some of the ponds and springs more frequently found in the Rio Tinto acid sulfate area (Fig. 4). The controlled environment will allow for investigating the sequential evaporation-deposition processes related to acidic waters through in-line Raman spectroscopy of the mineral phases and liquor. From comparison of derived models for synthetic and natural precipitation of sulfate minerals within acid mine drainage and acid mine drainage-like aqueous solutions, information on the occurrence of mineral phases and their main features may be obtained and correlated with the aqueous systems, pressure, temperature, and biological activity (if present) conditions.

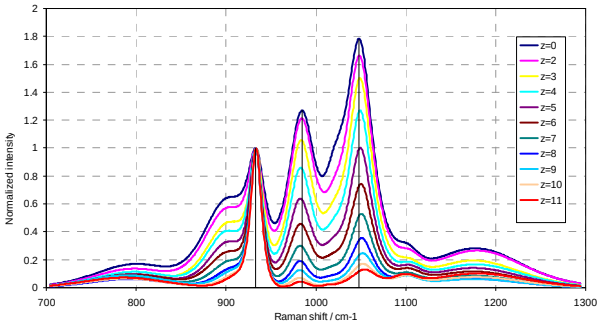

Fig. 2 Raman spectra recorded at t = 213 h and variable heights. The spectra have been normalized to the intensity of 935 cm^{-1} band (perchlorate band for internal reference)

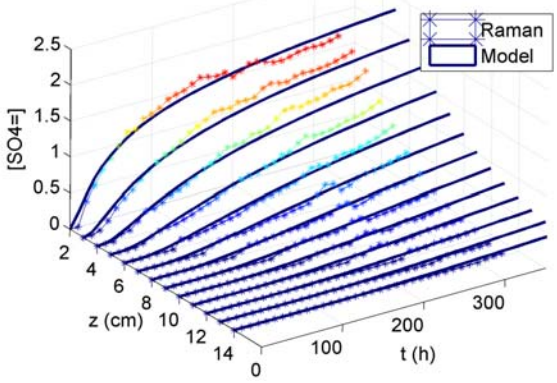

Fig. 3 Experimentally and model-based derived concentrations of sulfate and bisulfate ions concentrations as functions of time and height in the diffusion experiment

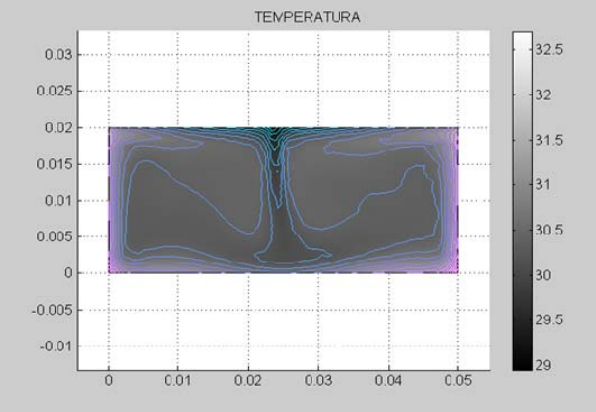

Fig. 4 Simulation of temperature distribution within the evaporation-precipitation device

Acknowledgement: Centro de Astrobiologia CSIC-INTA, Madrid, Spain.

References: [1] Klingelhöfer G. et al. (2004) *Science, 306,* 1740. [2] Clark B.C. et al. (2005) *Earth Planet. Sci. Lett., 240,* 73. [3] Rieder R. et al. (2004) *Science, 306,* 1746. [4] Burns R.G. (1994) In *Proc. Lunar Planet. Sci. XXV*, pp. 203.

THE DURATION OF CHEMICAL WEATHERING OF GUSEV CRATER'S WISHSTONE-WATCHTOWER SEQUENCE. B. Sutter[1], D.W. Ming[2], and D.C. Golden[3], [1]Jacobs/ESCG, Houston TX, 77058, brad.sutter-2@nasa.gov. [2]NASA Johnson Space Center, Houston, TX 77058. [3]ESCG/Hamilton Sundstrand, Houston, TX 77058.

Introduction: Mineralogical abundance of primary minerals versus secondary minerals, chemical mixing relationships, and elemental ratios have been used to assess the degree of aqueous alteration at Gusev Crater and Meridiani Planum [e.g., 1, 2, 3, 4, 5]. However, limited work has used Ti-normalized mass-balance analysis chemical data to quantify gains and losses of elements from altered materials as well as estimate the duration of aqueous alteration on Mars [6, 7]. The Ti-normalized mass-balance approach accounts for volumetric changes associated with geochemical alteration. If volumetric changes are not considered, observed geochemical trends based on unnormalized data have the potential to be misleading. Assessing gains and losses from altered materials can indicate the geochemistry of fluids involved in the alteration. Furthermore, elemental losses can be combined with dissolution rates to estimate the duration of chemical weathering. Knowledge of the duration of aqueous alteration will provide insight into the climate history of Mars as well as indicate the potential for microbial habitability. The Wishstone-Watchtower materials in Gusev Crater are suitable candidtates for Ti-normalized mass-balance analysis because mixing relationships of these two materials indicate that Watchtower materials may be derived from Wishstone-like materials [8]. The objectives of this work are to (1) employ Ti-normalized mass-balance to assess gains and losses from the Wishstone-Watchtower sequence and (2) to combine losses with laboratory dissolution rates to estimate alteration times of the Watchtower material.

Methods: The mass-balance equation was used to calculate elemental gains and losses (equation 1) [9,10]. The mass transport (τ_{jw}) of an element (j) in the weathered soil or altered rock (w) compared to its parent material (p) is calculated relative to an immobile element (i), where C is concentration of the respective elements:

$$\tau_{jw} = (C_{jw}/C_{iw} \,//\, C_{jp}/C_{ip}) - 1 \quad (1)$$

The gain or loss of mobile elements is determined by referencing the mobile element to an immobile element (e.g., Ti, Zr, Nb). When τ_{jw} is 0, the element is immobile; negative values indicate the element was removed from the weathered material, and positive values indicate the element was added from a source other than the parent material. For example, when τ_{jw} = -0.30, 30% of that element has been lost from weathered material relative to that element's starting concentration in the parent material.

Na loss was detected and determined to be derived from feldspar dissolution. Subsequently the remaining fraction (*f*) of feldspar is determind by

$$f = [(mM_{start} - mM_{end})/mM_{start}] \quad (2)$$

mM_{start} and mM_{end} refer to literature starting concentration of feldspar and calculated ending mineral concentration, respectively. If a starting particle size is assumed for a particular mineral then the fraction of the mineral that remains and its new particle size can be estimated by

$$\sqrt[3]{f \cdot r_{start}^{\,3}} = r_{end} \quad (3)$$

where r_{start} is the starting radius while r_{end} is the radius after the mineral has been dissolved.

The time for mineral dissolution is then calculated using the following equation [11]:

$$time = \frac{r_{end} - r_{start}}{-k \bullet V_m} \quad (4)$$

Where k is the literature rate constant and V_m is the molar volume of the mineral. For this work the rate constant is determined as a function of pH by [12]

$$\text{Log } k_{25C} = 9.5(pH)0.5 + 11.8 + 9.9(pOH)0.3 \quad (5)$$

The duration of dissolution can therefore be calculated as a function of pH and starting particle size.

The RATed Wishstone and Watchtower chemical data [13] were used to calculate gains and losses and to determine duration of chemical weathering.

Results/Discussion: Sodium is the primary element that was lost in the aqueous alteration of Wishstone to Watchtower materials (Table 1). Small losses/gains of Al, Ca, and P suggest that these elements are relatively immobile. Gains in Si, Fe, Mn, and Ni are indicated. Larger gains were determined for K, Mg, Zn, S, Cl and Br that mostly agree with the hypothesis that fluids enriched in Mg, Zn, S, and Cl were involved in altering Wishstone material to Watchtower material [8].

The moles of Mg, Fe, Si added to the Watchtower material indicates that the ratio of Mg and Fe to Si is 2.37. While this is not a perfect 2:1 ratio, this is close to the molar ratio of Mg and Fe to Si in olivine [$(Mg,Fe)_2SiO_4$].

Table 1. Mass transport τ_{jw} results for Watchtower-Joker-RAT relative to parent material Wishstone-Chisel-RAT.

Element	τ_{jw}	τ_{jw} error	mMoles/100g Gain/loss
Na_2O	-0.372	0.042	-29.9
Al_2O_3	-0.039	0.002	-5.7
P_2O_5	0.016	0.001	0.59
CaO	-0.019	0.001	-3.1
SiO_2	0.134	0.007	98.0
MnO	0.172	0.014	0.53
Ni	0.172	0.140	0.02
FeO	0.334	0.018	53.9
K_2O	0.521	0.075	3.5
MgO	1.604	0.094	180.5
SO_3	0.827	0.050	22.8
Cl	1.679	0.109	16.8
Zn	1.564	0.355	0.15
Br	12.371	9.069	0.34

This result suggests fluids involved in aqueous alteration of Wishstone to Watchtower may have derived Mg and Fe and Si from olivine dissolution. The ratio of Mg:Fe yields an olivine composition of $(Mg_{1.5},Fe_{0.5})SiO_4$. The excess Fe and Mg could be derived by incongruent dissolution of olivine where Fe and Mg are preferentially released relative to Si. Another possibility is that some Si is lost from feldspar as indicated by the negative $\tau_{j,w}$ for Na. The overall positive Si $\tau_{j,w}$ is a summation of some Si loss from feldspar coupled with Si addition from an outside olivine source.

The calculated Na loss indicated that Wishstone parent material lost feldspar in the formation of the Watchtower material. The feldspar loss was used to calculate duration of aqueous alteration as function of pH and particle size (Fig. 1). If the pH is assumed to be 4 [8] in this system then Wishtstone particles of 1 mm and 0.05 mm weathered over a period of 4300 and 217 years, respectively. However, laboratory rates used in these calculations can be 2 to 5 times faster than field rates [14] which can increase the time of aqeous alteration to as high as 45Kyr. Calculated aqueous alteration times are minimum times because laboratory rates are measured under high water to rock ratios, low ionic strength, and do not consider the formation of surface precipitates. Field conditions have low water:rock
ratios, higher ionic strengths, and surface precipitates that inhibit mineral dissolution and thus decrease dissolution rates. The addition of Si from proposed olivine dissolution would also contribute to slowing the dissolution of feldspar as well.

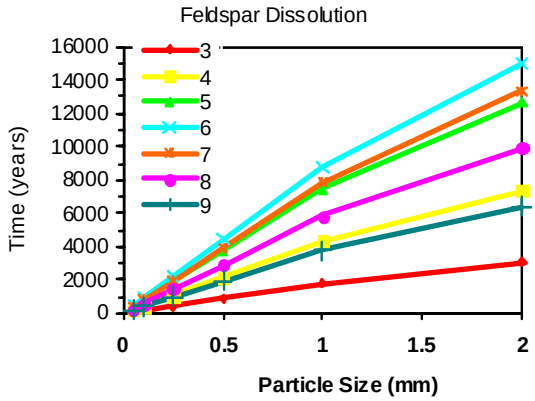

Fig. 1. Wishstone-Watchtower oligoclase dissolution times (y) as a function of particle size and pH.

Conclusions: Titanium-normailzed mass-balance results indicated that Na loss from feldspar dissolution occurred during the aqueous alteration of Wishstone to Watchtowerr materials. Minor gains in Fe, Mg, and Si suggested inputs from olivine dissolution from outside the Wishstone-Watchtower system. Alteration fluids also contained moderate levels of S and Cl. The amount of feldspar dissolution was derived from Na loss which was coupled with feldspar dissolution rates to estimate time of dissolution. Dissolution times of 217 to 4300 years were calculated and represent minimum times of dissolution. This work demonstrates the value of combining Ti-normalized mass-balance with laboratory dissolution rates in assessing duration of aqueous activity on Mars. Results from this work will serve as the foundation for developing more sophisticated kinetic dissolution calculations that will provide improved estimates of aqueous alteration times on Mars.

References: [1] Morris, R.V. et al., (2009) *JGR, Accepted*. [2] Ming, D.W. et al., (2008) *JGR,* 2008JE003195. [3] Hurowitz, J et al. (2006) *JGR*, *111*, 2006JE002795. [4] Schmidt, M.E. et al., (2008) *JGR, 113*, 207JE003027. [5] Yen, A. et al., (2008), *JGR, 113* 2007JE0029791979. [6] Hausrath et al., (2008), *Geology, 36*, 67. [7] Amundson et al. (2008) *Geochim Cos. Act 72*, 3845. [8] Hurowitz et al., (2006) *JGR, 111*, 2006JE002795. [9] Nesbitt, H.W. (1979), *Nature, 279,* 206. [10] Chadwick, O.A. et al., (1990) *Geomorph., 3*, 369. [11] Lasaga, A.C. (1984), *JGR,89*,4009. [12] Blum, A.E. & Stillings, L.L., (1995), *Rev. Min. 31*, 291. [13] Gellert, R. et al. (2006) *JGR, 111,* 2005JE002555. [14] White, A.F. and Brantly, S.L. (2003) *Chem. Geol 202*, 279.

MAGHNUM – A NUMERICAL SIMULATOR FOR NON-ISOTHERMAL FLOW AND TRANSPORT PROCESSES IN THE MARTIAN REGOLITH AND OTHER PERMEABLE MEDIA. B. J. Travis[1], J. Palguta[2], C. Barnhart[3], M. McGraw[4], W. C. Feldman[5], Computational Geosciences Group, Los Alamos National Laboratory, MS-F665, Los Alamos, NM 87545, bjtravis@lanl.gov; [2]Earth and Planetary Sciences Dept., UCLA; [3]Earth Sciences Dept., U. California, Santa Cruz; [4]U. Montana, Missoula, MT; [5]Planetary Science Institute, Tucson, AZ.

Introduction: There is an extensive body of physical and chemical evidence for the action of liquid water on the surface and in the near surface of Mars in the past. For example, a recent study [1], using THEMIS data, has found evidence of chloride salt deposits associated with a number of features on the surface of Mars, primarily in the southern hemisphere. Based on their interpretation of the data, precipitation from briny aquifers and surface ponds is a likely source of those salts. Other studies indicate high hydrogen content (and by inference, water content) at the surface of Mars in certain locales [2], even at the equator.

MAGHNUM model: To address dynamics of water, ice and salts in the Martian regolith, we developed the MAGHNUM numerical simulator. MAGHNUM provides a numerical solution of the governing partial differential equations for 1, 2, or 3-D, time-dependent non-isothermal fluid flow and reactive species transport in permeable media. Heterogeneous media (structured, or random/stochastic, or a mix), single liquid phase or two fluid phases (liquid and gas/vapor) plus an ice phase, determined by local thermodynamics, are model capabilities. Dependence of ice melt temperature on salt concentrations, changes in permeability/porosity due to mineral precipitation and dissolution, and hydrothermal-mineral alterations, are model features. It even has a microbial metabolic module.

Previous applications: A previous simulation study of aquifer dynamics in the Martian subsurface, using MAGHNUM, considered only pure water aquifers [3]. It found that hydrothermal convection develops for a range of geothermal gradients, for reasonable regolith properties. Despite a uniform surface temperature, uniform heat flux at depth, and uniform porosity/permeability structure, a non-uniform subsurface ice distribution can develop due to hydrothermal convection in the permeable subsurface. A subsequent, combined experimental and numerical study [4] considered both pure water and salty aquifer dynamics in response to a geothermal gradient. Salts not only depress the freezing point, but can add an unsteady characteristic to hydrothermal convection. Experiments of hydrothermal convection under cold conditions provided testing of the code, as well as measurements of viscosity vs temperature and salt concentration for subzero conditions (Fig. 1). Further experimental testing of hydrothermal circulation in brines under Martian conditions is needed.

Brine aquifers: The dominant Cl-containing salts in Martian subsurface aquifers are likely to be $CaCl_2$ and NaCl [5]. The NaCl eutectic point is about -22 ^oC, while for $CaCl_2$, the eutectic point is -52 ^oC. Geothermal gradients on Mars have been estimated to be in the range of 20 to 40 mW/m^2, with considerably higher values earlier in Mars' history, and possibly even now in certain areas such as the Tharsis region.

We are applying MAGHNUM to study dynamics of brine aquifers [6] having depth-dependent permeability and porosity and a high initial salt content ($CaCl_2$ at about 1 mole/liter) in the pore water, with surface temperature of -60 ^oC, and bottom heat flux of 30 mW/m^2. Using these values, the system convects; that is, the geothermal gradient drives an upward flow of brine through the soil pores. A downward return flow occurs in very narrow channels, "drainage pipes", that are essentially at the eutectic concentration and are completely liquid (see Fig. 2). The narrow "drainage pipes" lead to a non-uniform pattern of ice near the surface; there are icy lenses separated by liquid brine regions. The aquifer between the surface and a depth of about 400 m is partially frozen; fluid motion is still possible. The salinity at the top of the aquifer increases and then water begins to freeze out. Water ice fills the pores of the topmost 50 m of the aquifer, but there are also salt precipitate inclusions in the ice. Other simulations using higher heat flux result in locations where liquid brine is carried to the surface.

Considerable salt precipitates out in the ice layer, about 7.6 cm of pure salt per meter thickness of ice lens, on average for the lower geothermal gradients, and about 15.1 cm per meter for a shallow high heat flux case. If the lens ice evaporates over time, salt deposits will be left behind. Several 3-D geometry simulations have also been made; results are similar to the 2-D cases, but the near-surface pattern of ice is roughly polygonal. The "drainage pipe" features occur at the vertices of the polygons.

Impact crater outflow: Barnhart et al [7] are using MAGHNUM to investigate surface processes associated with impact hydrothermal systems. Fig. 3 shows the distribution of simulated water/rock ratios due to focusing of outflow towards the center of an impact crater, as a result of the cold surface and ice formation. Residual impact energy causes hydrothermal convective circulation below the crater floor, resulting in a non-uniform w/r ratio distribution.

Chemistry: MAGHNUM has been coupled to the PHREEQC chemical speciation code [8]. To date, it has been used for studying possible chemical reactions and hydrothermal circulation inside planetesimals, but it could just as well be applied to aqueous chemistry in the Martian regolith. We are also coupling the MAGHNUM code to FREZCHEM [9], a chemistry package designed specifically for chemical equilibrium reactions under cold conditions. This will allow us to model complex salt solutions and more accurately determine salt precipitate stratification and near surface mineral alteration.

Other applications: Several other Mars-related studies in progress include dark streaks as unsaturated flow in surface soils, planet scale hydrology, and seepage below polar caps. Non-Mars applications of MAGHNUM include planetesimals [10], hydrothermal convection in Europa's mantle, Enceladus [11], and permafrost on Earth.

References: [1] Osterloo M. M. et al (2008) *Science 319,* 1651–1654. [2] Feldman W. C. et al (2004) *JGR-Planets, 109*, 1-11. [3] Travis B. J., Rosenberg N. D. and Cuzzi J. N. (2003) *JGR Planets, 108,* 8040-8054. [4] McGraw M. A., Light A. S., and Travis B. J. (2006) *LPSC XXXVII,* abs. # 2224. [5] Knauth P. L. and Burt D. M. (2002) *Icarus 158*, 267-271. [6] Travis, B.J., and Feldman, W.C. (2009) *LPSC XL*, abs. #1315. [7] Barnhart, C. J., Nimmo, F., B. J. Travis, (2009*) LPSC XL*, abs. # 2013. [8] Palguta, J., Travis, B.J., Schubert, G. (2007) *LPSC XXXVIII*, #1370. [9] Giles, M., FREZCHEM – http://frezchem.dri.edu. [10] Travis, B. J., and Schubert, G. (2005) *EPSL* 240, 234-250. [11] Schubert, G., et al (2007) *Icarus* 188, 345-355.

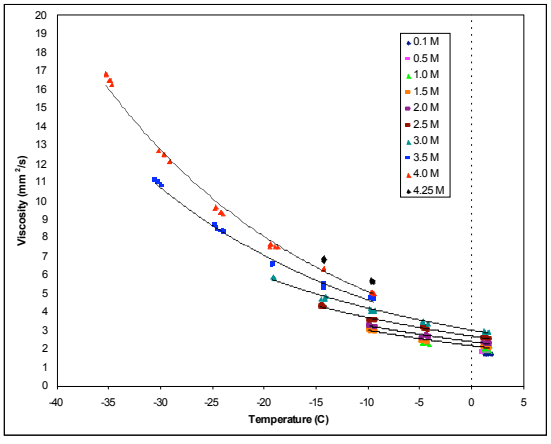

Fig. 1 Measured viscosity of $CaCl_2$ brine vs. temperature and salt concentration for subzero conditions. Viscosity increases by about an order of magnitude near the eutectic point compared to values at 0 °C.

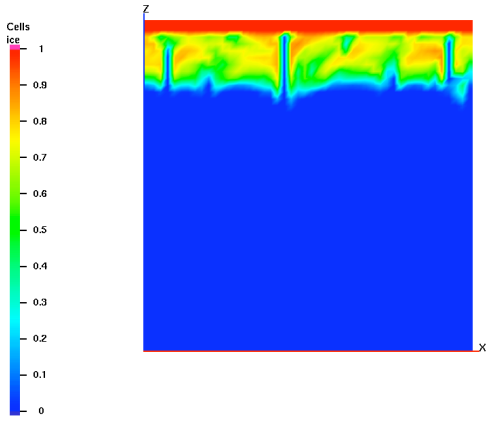

Fig. 2 Distribution of ice fraction on a vertical section through a brine aquifer after quasi-steady state has been established (~3000 yrs). The dimensions of the system shown are 2 km across by 2 km deep. "Ice fraction" here means fraction of pore water that is frozen. The upper 400 m are partially frozen. A roughly 50-100 m thick ice lens has developed at the surface. Narrow "drain pipes" form, that transport completely liquid brine back to the deeper aquifer. If salt were not present, the entire domain would be frozen.

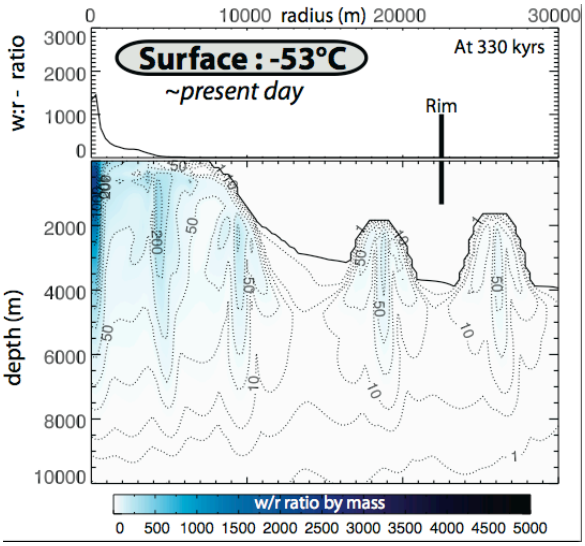

Fig. 3 Water/rock ratios after 330 kyrs after impact, below the floor of the impact crater (image from [7]). The cold surface and ice formation focuses outflow towards the center. The w/r = 1 contour marks the interface between ice and liquid water. The high w/r regions indicate hydrothermal upwelling locations.

MARTIAN AQUEOUS ALTERATIONS IN ALH 84001 AND THE NAKHLITE METEORITES.

A. H. Treiman, Lunar and Planetary Institute, 3600 Bay Area Blvd., Houston TX 77058 <treiman#lpi.usra.edu>.

ALH 84001: Water-deposited minerals are present throughout ALH 84001 [1]. They formed deposited at ~3.9 Ga [2], and bear witness the chemical and physical conditions of an ancient aqueous system. These clues are partially obscured by shock effects [3], and their interpretation has been muddied by now-discredited claims of evidence for biological activity.

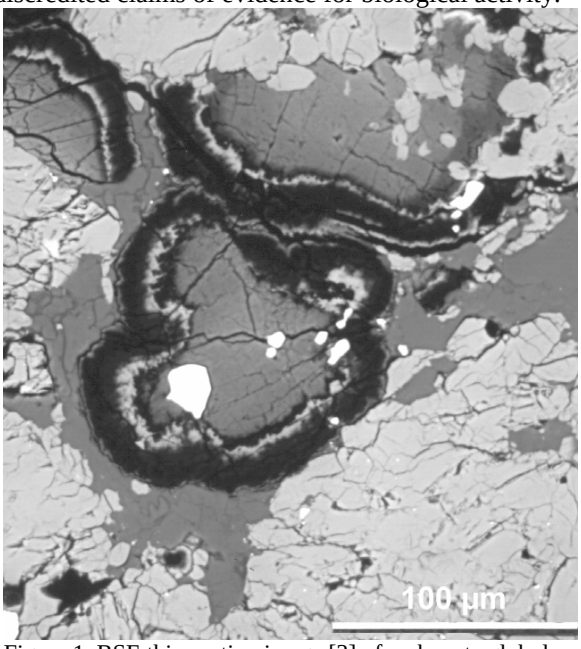

Figure 1. BSE thin section image [3] of carbonate globules (banded) in feldspathic glass (dark gray) among pyroxene (light gray). Pyrite grains (white) in globules. Note broken globule at upper left.

Carbonates. The dominant aqueous deposits in ALH 84001 are carbonate minerals, which form ellipsoids, discs, and other space-filling shapes, Figure 1 [1,4,5,6 etc]. These deposits are chemically zoned, nearly continuously from calcitic and ankeritic cores to magnesite-siderite compositions ranging from nearly pure magnesite to ~Mg45Fe45Ca10 (Fig. 2); hydromagnesite is not reported. The carbonates may have been deposited in several episodes [6,8]. The C and O isotope compositions of the carbonates vary in concert with cation compositions [6,9-11], consistent with formation by mixing of fluids. Early reports suggested carbonates formation near 700°C or from melts, but their chemical and isotopic zoning require hydrothermal to cryogenic conditions. Similar globules are reported on Earth in hydrothermal or groundwater alteration of basalt [5].

Other Primary Aqueous Effects. Associated with, and within, the carbonate globules are pyrite euhedra, rare sphalerite, and rare mica in submicron grains [12-14]. The S isotopic composition of the pyrite, $\delta^{34}S$ and $\Delta^{33}S$, suggest formation from low-temperature fluids that had interacted with the martian atmosphere [13,14]. Carbonate globules are spatially associated with small olivine grains [15], which may mean that the carbonates occupied void spaces produced by dissolution of other olivine grains [16,17]. Irregular textures on some orthopyroxene surfaces suggest dissolution and some precipitation of clays [18], but these effects are volumetrically minor. Veinlets of silica cut the carbonates and other minerals [19].

Subsequent Shock Effects. The carbonate globules and other aqueous deposits in ALH 84001 were strongly affected by a subsequent shock event [3]. Pre-shock void spaces (in which the globules grew [16]) were crushed, and globules were broken and transported in molten plagioclase [3]. In the thermal aftermath of the shock event [7], Fe-bearing carbonate was partially decomposed to Fe-poorer carbonate and magnetite, in shapes similar to those formed by some Earth bacteria [7,18,20-22]. Decomposition of siderite produces C-O (±H) gas species, which then reacts to form macromolecular carbon, catalyzed by the magnetite [4,7,23].

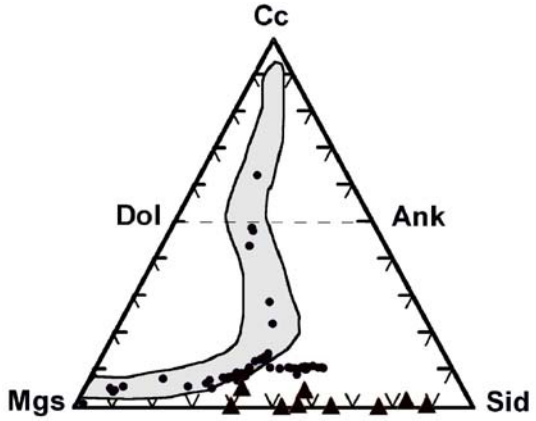

Figure 2. Carbonate compositions in ALH 84001 [7], shaded field is EMP analyses, comparable to other datasets. Dots are direct TEM analyses; triangles are spread-beam TEM of magnetite-rich areas (compositions of decomposed carbonate?).

Nakhlites: All of the nakhlite Martian meteorites (augite-olivine cumulate igneous rocks) contain deposits and alterations from Martian waters [24-26], mostly as veinlets and patches of red-brown 'iddingsite'. 'Iddingsite' is a sub-mm mixture of smectite clay, iron oxy-hydroxides, and salt minerals, formed by low-temperature aqueous alteration of olivine and glass (Fig. 3). Iddingsite forms veins

through olivine, stringers along cracks, and masses where mesostasis or intercumulus olivine once lay (Fig. 3). Iddingsite veins in olivine typically have serrated or saw-tooth borders formed of segments along the olivines' {021} planes. The coarsest smectite is in Lafayette, where grains (to ~100 mm) radiate from vein walls. The smectite has strong basal {001} cleavage with a broad diffraction of ~1.4nm [35], indicating significant disorder in stacking and intercalation. Near the centers of the veins are thin veinlets, a few mm wide, of submicron or amorphous material of smectite composition (refs in [26], [27]). These smaller veinlets cut across the structure and cleavages of the coarser smectite grains. This same pattern occurs terrestrial 'iddingsite' (e.g., Figs. 130, 131 of [28]). The iddingsite in Lafayette and Y000593 also contains iron oxide-hydroxide material, red isotropic masses in thin section. This material is Lafayette is nearly amorphous, and some diffracts as 'two-ring ferrihydrite' (Treiman, unpublished data). The iron oxide in NWA 817 is reported to be goethite [29].

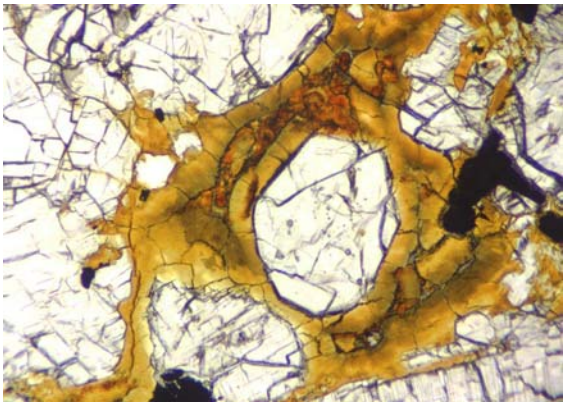

Figure 3. Iddingsite in Lafayette (plane polarized); smectite (yellow) and Fe-oxide material (red), & augite (clear) in Lafayette [26]; ~1 mm across. Iddingsite fills space among augites; smectite grains radiate inward; cores filled with round globules of Fe-oxide.

This iddingsite has a range of compositions, as can be seen on BSE imagery as bands and speckles of varying brightness. In bulk composition, iddingsite is equivalent (more or less) to mixtures of olivine, iron oxy-hydroxide, mesostasis glass, and water. Iddingsite in olivine has nearly no Al_2O_3, while that in mesostasis areas contains up to 5% Al_2O_3. Lafayette iddingsite has a REE pattern similar to that of the mesostasis, but at lower abundances [30]. Water in the iddingsite has a high $\delta^{18}O$ and a higher $\Delta^{17}O$ than the surrounding silicates – this is taken to indicate that the forming water had been in communication with Mars' surface and atmosphere [31].

Salt minerals are present associated with the 'iddingsite.' In Lafayette, there are grains or masses (to ~100 mm) of gypsum and calcic siderite [32,27]). The salt assemblage in Nakhla is more complex, with Mn-siderite, anhydrite, and halite [32]. These salts occur as unzoned, anhedral grains among feldspar and 'granitic' glass in the mesostasis, possibly associated with phosphates. MIL03346 contains gypsum associated with clay-like or amorphous material [33]. Jarosite is reported in several nakhlites, although it is not clearly pre-terrestrial. Sulfur in the sulfates [34] shows anomalous $\Delta^{33}S$, indicative of atmospheric effects.

In Nakhla, Lafayette, and Y000593, pyrite or marcasite occur with the iddingsite. Pyrite in Nakhla and Lafayette have sulfur isotope ratios near the solar-system initial, ($\delta^{34}S$ = ~3.4–+1.5‰) but with some mass-independent fractionation effects [14,34].

The biggest challenge of modeling alteration in the nakhlites will be dealing with its clay minerals, Fe-O-H phases and amorphous materials. Free energies of such materials are poorly defined, and they are subject to significant absorption and adsorption of cations, anions, and organic matter.

References: [1] Mittlefeldt D. (1994) *Meteoritics* 29, 214. [2] Borg L. et al. (1999) *Science* 286, 90. [3] Treiman A.H. (1998) *MaPS* 33, 753. [4] Steele A. et al. (2007) *MaPS* 42, 1549. [5] Treiman A.H. et al. (2002) *EPSL* 204, 323. [6] Eiler J.M. et al. (2002) *GCA* 66, 1285. [7] Treiman A.H. (2003) *Astrobiology* 3, 369. [8] Corrigan C. & Harvey R. (2004) *MaPS* 39, 17. [9] Niles P. et al. (2005) *GCA* 69, 2931. [10] Leshin et al. (1998) GCA 62, 3. [11] Saxton et al. (1998) EPSL 160, 811. [12] Brearley A.J. (2003) *MaPS* 38, 849. [13] Shearer C.K. et al.1(1996) GCA 60, 2921. [14] Greenwood J.P. et al. (2000) EPSL 184, 23. [15] Shearer C.K. et al. (1999) *MaPS* 34, 331. [16] Treiman A.H. (2005) *LPSC* XXXVI, Abstr. 1107. [17] Haustrath E. et al. (2008) *Astrobiology* 8, 1079. [18] Bradley J.P. et al. (1997) *Nature* 390, 454. [19] Valley J.W. et al. (1997) *Science* 275, 1663. [20] Golden et al. (2001) *Amer. Mineral.* 86, 370. [21] Golden et al. (2004) *Amer. Mineral.* 89, 681. [22] Bell M.S. (2007) *MaPS* 42, 935. [23] McCollum T.M. (2003) *GCA* 67, 311. [24] Bunch T.E. & Reid A.R. (1975) *Meteoritics* 10, 303. [25] Bridges J.C. et al. (2001) 365 in *Chronology and Evolution of Mars.* [26] Treiman A.H. (2005) *Chemie der Erde* 65, 203. [27] Changela H.C. & Bridges J.C. (2009) *Lunar Planet. Sci.* XXXX, Abstr. 2302. [28] Deligne (1998) *Atlas of Micromorphology of Mineral Alteration and Weathering*. Can. Mineral. Spec. Pub. #3. [29] Gillet et al., (2002) EPSL 203, 431. [30] Treiman A.H. & Lindstrom D.L. (1997) *J. Geophys. Res.* 102, 1953. [31] Romanek et al. (1998) *MaPS* 33, 775. [32] Bridges J.C. and Grady M.M. (2000) *EPSL* 176, 267. [33] Stopar et al., 2005 [34] Farquhar J. et al. (2000) *Nature* 404, 50. [35] Treiman A.H. et al. (2004) Lunar Planet. Sci. XXXVII, Abstr. 1179.

MINERALOGY IN THE MARTIAN HYDROSPHERE – DATA, ANALOGS AND EXPERIMENTS. D. T. Vaniman, EES-14, MS D462, Los Alamos National Laboratory, Los Alamos, NM 87545 (vaniman@lanl.gov)

Introduction: Mineral equilibria provide predictors of properties important in aqueous geochemistry (solubility, freezing, precipitation, dissolution, etc.). Prediction works well where groundwater is well above freezing, but less so where only thin films of cold water and ice are present. Calculations are also limited where water/rock ratios are small, the general case on Mars. On Mars many models of aqueous systems call on concentrated brines [1]. Recent low-temperature thermodynamic modeling has improved calculations [see presentations at this meeting], but much remains to be done in extending thermodynamic data to cold conditions, especially where mineral-H_2O reactions are solid-vapor rather than solid-liquid.

Dissolution and precipitation: High solubilities of salts and their abundance on Mars [2] make them a point of focus for studies of the martian hydrosphere. Sulfates and halides are a significant component of the martian regolith [3] and are common vein components in martian meteorites [4]. Lander chemical data from Viking, Pathfinder, and MER indicate a dominant sulfate component with less abundant halogen salts (Cl, Br). Orbital data support widespread distribution of sulfates of Mg, Ca, and Fe; carbonates are much rarer than expected. Recent results from Phoenix show perchlorate (ClO_4) salts at high latitude; associated salts include anhydrite and Ca-carbonate [5,6]. The surprising abundance of perchlorate at the Phoenix site shows that our ability to predict salt assemblages from available data is limited. Identification of Ca-carbonate at Phoenix shows that mineralogy seen from orbit may be insensitive to salt mixtures in low abundance or covered by soil that masks underlying material.

Silica is a common precipitate in the terrestrial hydrosphere; authigenic quartz coats and cements detrital grains in many sandstones and cristobalite and opaline silica are common terrestrial precipitates from silica-saturated fluids. These precipitates can greatly reduce porosity, permeability, and specific storage of aquifer rocks, especially clastic sediments. Simulated acid weathering of basalt under martian condition produces opal [7]. Recent spectral data from Mars suggest surface opaline deposits [8]. Silica leach rates from silicate glasses are greater than those from crystalline silicates; volcanic and impact glasses on Mars provide abundant material for silica in solution. Slow recycling of impact products on Mars is likely to leave a large inventory of shocked silicate materials susceptible to aqueous leaching. Special disordered materials such as maskelynite, rare on Earth, may be widely distributed on Mars and provide a special set of exceptionally reactive and leachable silicates.

Ferrihydrite is a common precipitate that can mature to hematite [9]. Goethite observed at Gusev implicates shallow aqueous alteration [10]; goethite can also mature to hematite. Hematite may thus be an indicator of ultimate aqueous origin. This rationale led to selection of Meridiani as a MER landing site on the basis of spectral identification of hematite. This decision was justified by the determination of abundant hematite at Meridiani, but the organization of hematite into small spherules ("blueberries") was not anticipated. These spherules and evidence for post-deposition dissolution (crystal molds) provide ongoing challenges to conceptual models for genesis of the assemblages, textures, and fabrics of sediments on Mars.

Salt, silicate, and oxide dissolution/precipitation processes on Mars may reflect a hydrosphere of the distant past [11] or may form in cycles repeated throughout martian history [12]. On Earth chemical deposition of silicates or oxides is generally separated in space and time from salt-depositing evaporites. Exceptions occur. One such is exception is siliceous calcrete, where water/rock ratios are low and the system is fed by acidic fluid that is quickly neutralized by reaction with soil detritus. This process is episodic, specific to low water/rock ratios, and produces soil zones and fracture fills distinct from hydrothermal or spring deposits [13]. Cycles of volcanic aerosol flux on Mars may result in similar mixed mineral precipitates; fracture fills at Meridiani may reflect mixed mineralogy derived from such a 'minimal' hydrologic system [14].

Alteration and water-rock interaction: Much of the authigenic mineralogy in Earth's hydrosphere is a product not of direct precipitation from solution but of water-rock reaction. Common alteration products include clay minerals and zeolites. Clay minerals are widely distributed on Mars and include smectites and kaolinites [15]. Zeolites are not as widely recognized but have been suggested [16]. Clay minerals have great influence over the hydrologic properties of rocks, particularly the swelling clays (smectites) that generate aquitards and aquicludes in the terrestrial hydrosphere. Models that include clay mineral formation in the hydrosphere can define the effect such alteration has on groundwater movement and composition.

Formation of clay minerals and zeolites is facilitated where a glass precursor is available. On Earth this is generally a volcanic glass; on Mars impact glasses and other impact-disordered phases may vie in

importance. Alteration by groundwater is seldom isochemical and is greatly influenced by water composition. Where silica-rich glass is the precursor, significant amounts of opal may form as a coproduct of zeolite growth; on Mars where silica-rich volcanic rocks are rare coproduction of silica may be much less common. Zeolites tend to form rather than phyllosilicates where waters are highly alkaline. Zeolitization of basaltic detritus produces low Si/Al zeolites such as thomsonite and phillipsite; generally the zeolite alteration products in basalts on Earth are in cavities or vugs and reflect elevated temperatures in the hydrosphere. On Mars long exposure of basaltic deposits to impact and local magmatic thermal systems could lead to similar alteration.

Reactive transport: Modern modeling of the terrestrial hydrosphere is rapidly increasing the ability to predict flow systems and host-rock reactions. Precipitation/dissolution, sorption/desorption, and cation exchange figure prominently in research directed at understanding problems such as fouling of hydrothermal power plants, sequestration and migration of hazardous wastes, and long-term viability of stressed aquifers. Models have been tested and modified through both laboratory studies and controlled field studies [17,18]. Mars presents plenty of surface evidence for high ionic strength fluids in the prevalence of regolith salts and evaporites, but the nature of deep groundwater is elusive. Nevertheless, models of reactive transport leading to saline fluids help address questions of whether evaporite minerals on the surface are products of groundwater brines or of evaporation from saline lakes.

Overcoming terrestrial bias. Terrestrial examples have been used throughout this discussion. This is natural, since our hands-on knowledge of mineralogy in a planetary hydrosphere is limited to Earth. It is important however to consider how different Mars is from Earth and those aspects of the Mars hydrosphere that present challenges to terrestrial analogy.

Stagnation. Water/rock reactions on Mars are generally slower than on Earth. Absence of plate tectonics to cycle wet sediment into the lithosphere results in a more static deep groundwater system with drier host rock. This system is perturbed by impact and volcanic events, but these leave relatively permanent scars that are not recycled into new lithosphere. Minerals formed in the martian hydrosphere that would have limited "lifespans" on Earth (e.g., salt hydrates, opal-A, smectites, zeolites) may persist on Mars indefinitely.

Cold, dry conditions. Some of the best terrestrial analogs for Mars are in polar regions such as the Dry Valleys of Antarctica. However, no terrestrial region is as persistently cold and dry as Mars. Very slow reaction rates, disequilibrium assemblages, and pathway-dependent reactions are likely to be far more prevalent on Mars than on Earth. In terms of mineralogy generated in the hydrosphere, it is likely that rich mineral associations not in equilibrium will be the norm, at least in surface and shallow zones accessible for study. Disequilibrium presents challenges to modeling mineral systems in the martian hydrosphere.

Severe obliquity cycles. Massive redistribution of ice on Mars follows obliquity excursions of a magnitude not seen on Earth. Subglacial and periglacial processes are thus relatively more significant on Mars [19]. In this situation, mineral alteration or precipitation in a thin zone of meltwater at the edge of a buried ice mass, or around dark lithic grains in ice [20], may be more significant than precipitation from an ephemeral lake.

Low water/rock ratios. Fluvial systems on Mars are abundantly represented by deltaic deposits, scoured channels, and other fluvial geomorphic features. Observed features point to high-energy environments with evidence of persistent standing bodies of water elusive. Episodic releases of water appear to be catastrophic with little time for water/rock reaction; dispersion of surface water into groundwater appears to have been rapid. At dispersed and low water/rock ratios the mineralogy of the hydrosphere is likely dominated by soluble salts. However, evidence of abundant clay minerals suggests higher water/rock ratios. A challenge to understanding the martian hydrosphere is in development of credible models for what appears to have once been a much wetter environment. The impact of this concept on Mars rivals the concept of a terminal cataclysm on the Moon, and is likely to be a source of debate for at least as long.

References: [1] Brass G. (1980) *Icarus* 42, 20-28. [2] Clark B. and VanHart D. (1981) *Icarus* 45, 370-378. [3] Clark B. (1993) *GCA* 57, 4575-4581. [4] Rao M. et al. (2005) *JGR* 110, E12. [5] Golden D. et al. (2009) *LPS XL*, Abstract #2319. [6] Boynton W. et al. (2009) *LPS XL*, Abstract #2434. [7] Tosca N. et al. (2004 *JGR* 109, E05003. [8] Squyres S. et al. (2008) *Science* 320, 1063-1067. [9] Michel F. et al. (2007) *Science* 316, 1726-1729. [10] Morris R. et al. (2008) JGR 113, E12S42. [11] Chevrier V. et al. (2007) *Nature* 448, 60-63. [12] Settle M. (1979) *JGR* 84, 8343-8354. [13] Vaniman D. et al. (1994) *Geoderma* 63, 1-17. [14] Knoll A. et al. (2008) JGR 113, E06S16. [15] Wray J. et al. (2008) *GRL* 35, L12202. [16] Michalski J. and Ferguson R. (2009*) Icarus* 199, 25-48. [17] Moore J. and Bullock M. (1999) *JGR* 104, 21,925-21,934. [18] Hausrath E. et al. (2008) *Geology* 36, 67-70. [19] Levrard B. et al. (2004) *Nature* 431, 1072-1075. [20] Priscu J. et al. (1998) *Science* 280, 2095-2098.

CORROSION TEXTURES FORMED BY AQUEOUS ALTERATION OF MARS METEORITE OLIVINE AND TERRESTRIAL ANALOGS. M. A. Velbel, Department of Geological Sciences, 206 Natural Science Building, Michigan State University, East Lansing, MI 48824-1115 (velbel@msu.edu).

Introduction: Olivine is a geochemically important mineral on Mars. It has been identified in Mars surface materials by instruments on the Mars Exploration Rovers [1-8] and several Mars orbiters [9-15]. Olivine dissolution is inferred to have contributed significantly to the solute composition of inferred Martian groundwaters [16-19]. Olivine is also a major constituent of Mars meteorites, including nakhlites [20, 21], chassignites [21], and many shergottites [21]. Many Mars meteorites contain small quantities of aqueous alteration minerals, some of which are associated with olivine [20-30]. In freshly fallen meteorites (*falls*), aqueous alteration minerals are pre-terrestrial, and record aqueous alteration on their parent body [23-30]. Most Mars meteorites available for scientific study are *finds*, recovered after some exposure to the terrestrial surface environment, with associated effects of terrestrial aqueous weathering and contamination superimposed upon the mineral assemblages of pre-terrestrial origin [25, 31-33].

This paper reports weathering textures of olivine in the Mars meteorite MIL03346 [20, 21, 34-35], recovered in Antarctica. Alteration phenomena include pre-terrestrial alteration of olivine along fractures to veins of iddingsite (a clay-oxide mixture), thermal pyrometamorphism of the Martian iddingsite near the meteorite surface during passage through Earth's atmosphere, and terrestrial corrosion of olivine. Olivine corrosion in MIL03346 is compared with textures formed by terrestrial aqueous corrosion of terrestrial olivine [36-39].

Background: Terrestrial olivine corrosion. Naturally weathered olivine occurring as phenocrysts in Hawai'ian volcanic rocks from several volcanic centers and regolith/outcrop settings [36, 37, 39], and as tectonized olivines from several metadunite bodies in the southern Appalachian Blue Ridge [38, 39] were examined in polished thin-section using transmitted polarized-light microscopy and scanning electron microscopy in backscattered electron imaging mode (SEM-BEI) with energy-dispersive spectroscopy (EDS) [36-39]. All naturally weathered olivines are similarly corroded. Conical (funnel-shaped) etch pits occur as individual pits, base-to-base pairs of cone-shaped pits, or *en echelon* arrays [36-39]. The orientation of the etch pits is crystallographically controlled, but the pits are anhedral; etch-pit walls are not common crystal planes of olivine [39]. The pointed end of each etch pit probably defines the dislocation around which the etch pit develops [36-39]. In SEM-BEI images of polished thin sections, olivine etch pits at grain boundaries, fractures, and contacts with veins appear as triangular (wedge-shaped) cross-sections through the funnels [37, 39]. In weathered terrestrial olivine, individual etch pits range in size from as small as the limit of SEM resolution to as large 80 μm in longest dimension [36-39]. The smallest etch-pit arrays visible in conventional SEM resemble even smaller features previously reported from transmission electron microscope investigations of olivine weathering.

Olivine etch pits occur in samples with chemical and/or mineralogical evidence of weathering, and/or are associated with, or proximal or directly connected to, fractures (the avenues along which aqueous solutions come into contact, and react, with the olivine) or exposed outcrop surfaces [38, 39]. Etch pits therefore form by weathering and not inherited from pre-weathering aqueous alteration (e.g., serpentinization, iddingsitization) of these parent rocks [39].

Natural weathering of olivine is surface-reaction-limited [39]. Many etch pits are devoid of weathering products, implying that olivine weathering can take place by congruent dissolution as well as by long-understood replacement mechanisms. Published laboratory dissolution experiments reproduce some morphologic features of natural weathering, but not under geochemical conditions resembling natural weathering. Etch pits similar to those formed during natural weathering [39] are formed on olivine altered in abiotic experiments at strongly acidic pH, but are not observed on olivine grains experimentally altered under biotically influenced conditions. Similarity of corrosion forms from naturally weathered olivine from multiple igneous and metamorphic parent-rock bodies suggests that olivine weathers in the same manner regardless of its specific crystallization/recrystallization history, eruption/weathering/exposure ages of the olivine's host rock, and the local regolith history [39].

Sample and methods: MIL03346 is an Antarctic nakhlite find. Original recovered mass was 715.2 g. At weathering category B, it is more weathered than at least half of all other U.S. Antarctic Mars meteorites. It is also the most fractured U.S. Antarctic Mars meteorite recovered to date. (Info from Astromaterials Curation at NASA JSC website, http://curator.jsc.nasa.gov/antmet/, U.S. Antarctic Meteorite Classification Database). Its petrology, geo-

chemistry and mineralogy have been previously described [20, 21, 34-35].

A polished thin-section was examine using transmitted polarized-light microscopy and scanning electron microscopy in backscattered electron imaging mode (SEM-BEI) with energy-dispersive spectroscopy (EDS).

Results from MIL03346: Both olivine and pyroxene are crosscut by alteration veins that also crosscut fusion crust. Consequently, vein materials (including Martian iddingsite) and their olivine host may have been influenced by terrestrial processes and contaminants [25, 31-33].

Incipient corrosion of olivine in MIL03346 occurs as individual etch pits with wedge-shaped cross-sections of typical form for olivine [33-36] but with maximum dimensions of only 1-2 μm, comparable to the onset of weathering in terrestrial olivine-bearing rocks [38, 39]. As in the weathered terrestrial olivines, etch pits in MIL03346 olivine are at or near fractures or iddingsite veins, the current or former avenues along which aqueous solutions enter the rock and come into reactive contact with the olivine. Olivine etching in MIL03346 occurs only in olivine within a few hundred microns of the meteorite's surface.

Implications: When subjected to aqueous solutions undersaturated with respect to olivine, Martian olivine corrodes in the same manner as terrestrial olivine from a variety of olivine-bearing parent rocks [36-39]. Incipient crystallographically controlled corrosion of olivine (small etch pits of typical form for olivine) occurs only along fractures or veins (avenues for solutions), and only within a few hundred microns of the meteorite's surface. This association of olivine etching with the meteorite's terrestrially exposed surface indicates that olivine corrosion is a terrestrial weathering effect, not the result of aqueous alteration of olivine on Mars. It also indicates that small quantities of cold initially dilute water (Antarctic supraglacial meltwater) are sufficient to weather olivine in Martian igneous rocks.

Olivine in the interior of Mars meteorite MIL03346 lacks etch pits. Therefore, either the water to which Mars meteorite falls were exposed on Mars was of a composition that did not corrode olivine (unlikely in light of the inferred importance of olivine in the evolution of Mars' groundwater chemistry [16-19]), or the olivines of Mars meteorite falls were exposed to even less water over their entire 1.3 Ga history on Mars than MIL03346 has been exposed to during its short residency on Earth.

Acknowledgments: Susan J. Wentworth, Ewa Danielewicz and J. Michael Ranck assisted with acquisition of SEM images. This research was supported by NASA Mars Fundamental Research Program grant NNG05GL77G.

References: [1] McSween H. Y. et al. (2004) *Science, 305,* 842-845. [2] Morris R. V. et al. (2004) *Science, 305,* 833-836. [3] Christensen P. R. et al. (2004) *Science, 305,* 837-842. [4] Squyres S. W. et al. (2004) *Science, 305,* 794-799. [5] Klingelhöfer G. et al. (2004) *Science, 306,* 1740-1745. [6] Christensen P. R. et al. (2004) *Science, 306,* 1733-1739. [7] Squyres S. W. et al. (2004) *Science, 306,* 1709-1714. [8] Morris R. V. et al. (2006) *JGR, 111,* E02S13. [9] Christensen P. R. et al. (2003) *Science, 300,* 2056-2061. [10] Hoefen T. M. et al. (2003) *Science, 302,* 627-630. [11] Bibring J.-P. et al. (2005) *Science, 307,* 1576-1581. [12] Mustard J. F. et al. (2005) *Science, 307,* 1594-1597. [13] Ehlmann B. L. et al. (2008) *Nature Geoscience, 1,* 365-368. [14] Mustard J. F. et al. (2008) *Nature, 454,*305-309. [15] Ehlmann B. L. et al. (2008) *Science, 322,* 1828-1832. [16] Rieder R. (2004) *Science, 306,* 1746-1749. [17] Squyres S. W. and Knoll A. H. (2005) *Earth and Planetary Science Letters, 240,* 1-10. [18] McLennan S. M. et al. (2005) *Earth and Planetary Science Letters, 240,* 95-121. [19] Tosca N. J. (2005) *Earth and Planetary Science Letters, 240,* 122-148. [20] Treiman A. H. (2005) *Chemie der Erde, 65,* 203-270. [21] Meyer, C. (2003) *Mars Meteorite Compendium*, http://curator.jsc.nasa.gov/antmet/mmc/mmc.htm. [22] Wentworth S. J. et al. (2005) *Icarus, 174,* 382-395. [23] Bridges J. C. and Grady M. M. (2000) *Earth and Planetary Science Letters, 176,* 267-279. [24] Gooding, J. L. (1986) *Geochimica Cosmochimica Acta, 50*, 2215-2223. [25] Gooding, J. L. (1986) *LPI Tech. Report 86-01,* 48-54. [26] Gooding J. L. et al. (1988) *Geochimica et Cosmochimica Acta, 52*, 909-915. [27] Gooding J. L. et al. (1991) *Meteoritics, 26*, 135-143. [28] Treiman A. H. et al. (1993) *Meteoritics, 28*, 86-97. [29] Wentworth S. J. and Gooding J. L. (1993) *LPS XIV,* 1507-1508. [30] Wentworth S. J. and Gooding J. L. (1994) *Meteoritics, 29*, 860-863. [31] Velbel M. A. (1988) *Meteoritics, 23,* 151-159. [32] Velbel M. A. and Gooding J. L. (1990) *LPI Tech. Report 90-01,* 94-98. [33] Velbel M. A. et al. (1991) *Geochimica et Cosmochimica Acta, 55*, 67-76. [34] Dyar M. D. et al. (2005) *JGR, 110,* E09005. [35] Day J. M. D. et al. (2006) *Meteoritics & Planet. Sci., 41,* 581-606. [36] Velbel M. A. (1993) *American Mineralogist, 78,* 408-417. [37] Velbel M. A. (2006) *LPS XXXVII,* Abstract #1807. [38] Velbel M. A. and Ranck J. M. (2008) *Min. Mag., 72,* 149-152. [39] Velbel M. A. (in revision) *Geochimica et Cosmochimica Acta*.

MEGAFANS AS HYDROUS ENVIRONMENTS. M. Justin Wilkinson,[1] R. McG. Miller,[2] C. C. Allen,[3] M.H. Kreslavsky,[4] F. Eckardt.[5] [1]Jacobs Engineering, NASA–Johnson Space Center, 2224 Bay Area Blvd., Houston TX 77058, USA. [2]PO Box 11222, Windhoek, Namibia. [3]NASA–JSC, 2101 NASA Parkway, Houston, TX 77058. [4]Earth and Planetary Sciences, University of California–Santa Cruz, 1156 High St., Santa Cruz CA 95064, USA. [5]Environmental & Geographical Science Dept., University of Cape Town, Cape Town 7701, South Africa.

Introduction: The mesoscale sedimentary environment known as the *megafan,* is a low-angle, partial cone of fluvial sediment generated where a river enters an unconfined basin where it begins the process of avulsing over wide areas. In shifting to different positions, the river lays down a partial cone of sediment and establishes a characteristic radial pattern of paleo courses. Fan radii reach several hundred km [1]. In a global study, provoked by features encountered worldwide in astronaut handheld imagery, more than 150 megafans (defined as >100 km in length, some exceeding 600 km) have been identified on Earth [1, 2]. Megafans are generated by processes different from those responsible for classic, small alluvial fans and deltas [1]. Nested megafans cover areas of 10^5 km^2 in Africa [1]. We argue elsewhere [3] that megafans ought to be common throughout the geologic history of Mars; and should therefore provide a viable model for some martian mesoscale fluvial sediment bodies.

The megafan model is parsimonious in the sense that it explains large, flat plains of low slope without the presence of a waterbody—despite the commonly expressed assumption that waterbodies are necessary for the formation of such plains (e.g. [4]).

Cubango Megafan, Kalahari Desert: The central and northern parts of the arid Kalahari basin of southern Africa are underlain by a suite of nested megafans [2]. The location of the largest (320 km radius) was successfully predicted [2] based on patterns apparent in a global survey. A source river and convex-downhill topographic contours confirmed the feature as a large fluvial cone (fig. 1). The finding was corroborated by surface geology and borehole data describing water-table slope, subsurface flow directions, and isotopic water-age trends [5]. Recognition of the feature had been hampered by its relict character (due to abandonment by the formative and now-incised Okavango R.), overprinting by linear dunes, flooding of distal slopes by the neighboring Cuvelai R., and by the smooth, flat topography (slope 0.02°).

The subsurface data show that groundwater is directed to the lower slopes of the fan, coinciding with a "major transboundary aquifer system" mapped along the Namibia–Angola border [6]. Subsurface flow is probably directed by an internal architecture of radial channel sands embedded within sheetlike bodies.

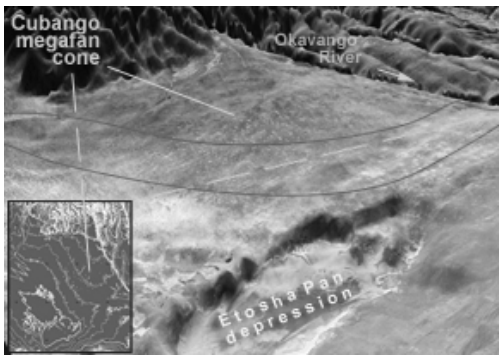

Fig. 1 Cubango megafan—north-looking oblique digital elevation model (DEM) with draped Landsat image overlay. Megafan, 320 km long (apex to Etosha depression), generated by the Okavango R., hosts a major, distal, subsurface water body (within curved lines). Namibia–Angola border—dashed line. Vertical exaggeration 1000x. (False color Landsat image, rendered as grayscale, draped on Shuttle Radar Topgraphy Mapping DEM.). *Inset:* SRTM-based contour lines (20 m) show partial cone morphology.

Possible Analogs on Mars: The apparent paucity of sedimentary bodies obviously tied to martian outflow channels may also relate to the difficulty of recognition due to their sheer size and featurelessness. However, the existence of megafans on Mars is being examined now that their ubiquity and characteristics on Earth are better understood. Accordingly we suggest two likely candidates on Mars.

We note that moderate water equivalent hydrogen (WEH) levels are recorded over both features [7].

Maja Valles fluvial cone (22–35N 150–175W). Mapped as a fluvial sediment body (unit $HNCc_1$ [8]) with a length of >100 km, the feature is described as a "broad, low cone of alluvial material" [9], and a "low relief, dissected fan" [10]. Generated apparently by sediments carried down Maja Valles, the fan apex is tied to the point where the Maja gorge cuts Xanthe Montes (fig. 2). Evidence of repeated flow in Maja Valles [e.g. 11], despite phases of incision, suggests that water has accumulated within the lower sediment body (fig. 2) where possible obstacles to distal fan development are noted.

Amazonis Planitia fluvial sedimentary bodies (17–19.5N 52–54W). Sourced from Martes Valles, a young Amazonis Planitia sediment mass (unit AAa_{2n} [8]) is here interpreted as a thin megafan. A diverging pattern

of channels is mapped, extending hundreds of km from the end of Martes Valles, spreading across areas on the order of 10^5 km^2 in the central planitia [12] (provisional unit (Achp) in [12])(fig. 3).

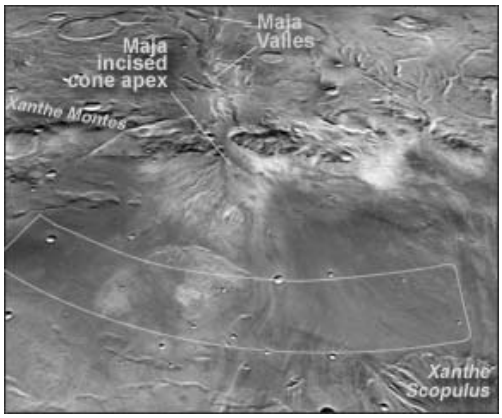

Fig. 2 Maja Valles incised fan feature occupies the center of this west-looking oblique image (THEMIS daytime IR mosaic). Fan apexed where Maja Valles gorge cuts through Xanthe Montes. Distal putative hydrous zone—within curved lines. Fan apex to Xanthe Scopulus is 107 km.

The topographic roughness algorithm that has been applied to Mars MOLA data [13, 14] was applied to Earth SRTM data for the Kalahari region [2] and more recently to most of the Earth (60N-60S)[15]. This study shows that all large areas of smoothest, low-slope topography on Earth's continents are almost exclusively megafan surfaces. The well-known extreme flatness of the martian planitia [12, 13, 14] accords with roughness signatures of terrestrial megafans, and suggests fluvial emplacement of young Amazonis units as argued in [12].

Two cryptic examples from Amazonis Planitia may be important for understanding subsurface hydrous accumulation. For at least some of its history, discharges from Mangala Valles likely resulted in megafans (in those scenarios when distal lakes/oceans were not synchronous with fluvial discharges [12]). Distances from the end of Mangala Valles to the northern (low) margin of the planitia are very large, a fact that has suggested that fluvial emplacement was unlikely [12]. However, the megafan model shows that long megafan radii are indeed feasible. It has been suggested further that discharge from Labou Vallis (8.5S 154.5W) must have led to fluvial sedimentation in the planitia [12]. We suggest that during locally non-lacustrine/ocean phases, this sedimentation would have occurred in the form of megafans.

Megafans emanating from Marte, Mangala and Labou valles have probably contributed to hydrous near-subsurface environments in their distal reaches—i.e. along the northern, eastern and southeastern margins of Amazonis Planitia at various times.

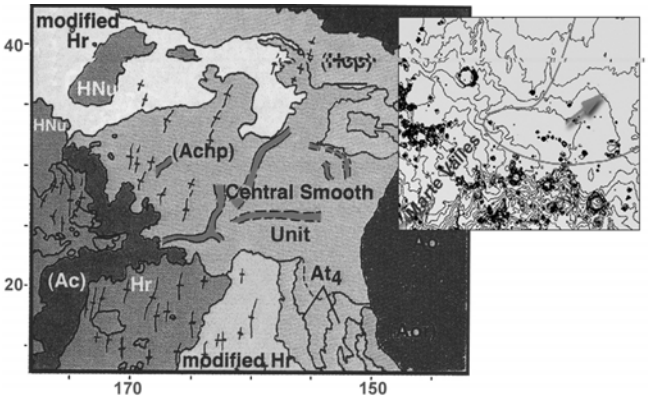

Fig. 3 Amazonis Planitia—Diverging drainage lines (dark sinuous features) on Central Smooth Unit (unit (Achp) in [12], AAa_{2n} in [8]). Marte Valles fills (Ac). Olympus Mons—black unit far right. Adapted from [12]. *Inset*: Martes Valles megafan apex zone: MOLA-based contour patterns (25 m). Confined Marte Valles opens onto unconfined plains of southwest Amazonis Planitia. Contours convex to fluid-flow directions (arrow) indicate partial cone morphology hundreds of km in extent (enclosed area top right).

Conclusion: Following a new terrestrial analog, we conclude groundwater has at times accumulated preferentially beneath distal slopes of the Maja Valles feature, and along the northern, eastern and southeastern margins of Amazonis Planitia.

References: [1] Wilkinson M. J. et al. (2006) *Jour. S. Amer. Earth Sciences 21*, 151-172. [2] Wilkinson M. J. & Kreslavsky M. A. (2008) 3rd Southern Deserts Conf. (Oxford U.), Molopo Lodge, Northern Cape, South Africa. [3] Wilkinson M. J. et al. (2008) *LPS XXVII,* Abstract #1392. [4] de Hon R. A. (1988) *LPS XIX*, Abstract #1134. [5] Miller, R. McG. (2008) *The Geology of Namibia*, *v. 3, ch. 24,* 24-1–24-76. [6] Struckmeier W. F. et al. (2006) Groundwater Resources of the World. Transboundary Aquifer Systems. *Fourth World Water Forum, Mexico City, March 2006.* [7] Berman D. C. et al. (2009) *LPS XL,* Abstract #1333. [8] Tanaka K. L. et al. (2005) *USGS Atlas of Mars, Sci. Investig. Map 2888 and Pamphlet.* [9] Rice J. W. et al. (1988) *LPS XIX*, Abstract #1494. [10] de Hon R. A. (1993) *LPS XXIV,* Abstract #1196. [11] Chapman M. G. et al. (2003) *JGR, 108 (E10),* 5113. [12] Fuller E. R. & Head J. W. (2002) *JGR, 107 no. E10*, 24 pp. [13] Kreslavsky M. A. & Head J. W. (1999) *JGR, 104,* 21,911-21,924. [14] Kreslavsky M. A. & Head J. W. (2002) *JGR, 105,* 26.695-26,712. [15] Wilkinson M. J. & Kreslavsky M. A. (2009) unpublished observations.

AQUEOUS CHEMICAL PROCESSES IN MARS' HISTORY. M. Yu. Zolotov, School of Earth and Space Exploration, Arizona State University, Tempe, Arizona 85287-1404, USA. E-mail: zolotov@asu.edu.

Introduction: The detection of layered deposits with sulfates and phyllosilicates, silica and carbonates implies dissolution of rocks and aqueous transport of chemical elements on ancient Mars [e.g., 1-5]. The presence of salts, phyllosilicates and carbonates in some martian meteorites also indicates aqueous processes [6]. However, aqueous solutions are not stable at the present surface, and observed minerals could have formed at different conditions in the past.

Although martian climate may have never been much warmer and wetter than today, strong impacts and igneous events led to episodic aqueous activity throughout history. During the Noachian epoch, aqueous fluids eroded highlands, formed valley networks and may have led to the formation of phyllosilicates [1-3]. During the Hesperian, formation of outflow channels could be attributed to igneous activity, which also supplied acid volatiles and initiated hydrothermal systems. Throughout history, low-temperature (T) processes could have involved brines in surface (at high obliquity) and ground ice-bearing deposits, and in deep subsurface rocks. Here I discuss major chemical processes that involve liquid water on Mars.

Magma-water and deuteric interactions: Water interacted with silicate melts during accretion, in a magma ocean, and during impacts and igneous activity throughout history. These processes led to oxidation of Fe^{2+} and sulfur followed by release and escape of hydrogen. High-T oxidation by H_2O can be responsible for the high oxidation state of crustal igneous rocks represented by some martian meteorites. A slow cooling of the magma ocean and large intrusions may have caused deuteric alteration. Although this process is not observed in martian meteorites, deuteric alteration of basic rocks may lead to phyllosilicates [7].

Rock alteration at depth: Below ice-bearing rocks, pore solutions could have existed throughout history. Alteration could have led to partially oxidized (Fe_3O_4-bearing) and hydrated carbonate-bearing rocks and alkaline, reduced (H_2-rich) and saline fluids. Although acid-base reactions may have approached equilibrium, reducing (H_2, HS^-, Fe^{2+}, CH_4) and oxidizing (SO_4^{2-}, HCO_3^-, etc.) species may have not equilibrated at low T. However, redox reactions can be sped up by chemotrophic life. Atmospheric CH_4 over some regions [8] could result from ongoing reduction of carbon by H_2 that forms via oxidation of Fe^{2+}-minerals [e.g. 9]. Hydrothermal alteration can also be possible down to ~30 km (when rocks become impermeable).

Chemical weathering: Over time, surface rocks have been affected by multiple precipitations of volcanic and impact generated aerosols and rains [10, 11]. Corresponding uneven low-pH dissolution of minerals was limited by freezing and evaporation leading to formation of amorphous silica, other semi-crystalline phases (Fe^{3+} and Al^{3+} hydroxides/oxyhydroxides), acid salts (e.g., Fe^{3+} sulfates), and resulted in accumulation of S, Cl and Br in salts. Preferable low-pH dissolution of Mg-Fe silicates led to Mg-Fe salts and Fe^{3+} oxides [e.g., 11-13]. Although Ca carbonates should have been destroyed by low-pH fluids, phyllosilicates are even more resistant than minerals of basic and ultrabasic rocks. Surface reactions rarely came to completion resulting in unequilibrated mineral assemblages.

Trapping of acid droplets in surface ice prevented their evaporation and may have led to long-term weathering of minerals in ice and underlying rocks at $T \geq \sim -70^oC$, which corresponds to stable H_2SO_4-HCl rich brines [11,14]. This process could have been important during periods of high obliquity [11,15] and may explain formation of layered sulfate-rich deposits formed after ice sublimation [15].

Although episodes of acid weathering were unavoidable in the early Noachian, larger amounts of surface fluids and/or a warmer climate may have caused complete neutralization of fluids and precipitation of smectites, zeolites and carbonates at neutral/alkaline pH. Phyllosilicates may have survived subsequent acid weathering episodes.

Redox processes: Several aqueous oxidation processes could have occurred in the atmosphere and at the surface. Atmospheric oxidation included formation of acid aerosols from SO_2, H_2S and N oxides after volcanic and/or impact events and involves ultraviolet (UV) photons and O_2 (photochemical or impact-generated). On early Mars, strong solar UV activity and intense photochemical production of O_2 [16,17] favored oxidation of S, C, N and Fe species in aerosols and fluids. Abundant sulfites may not form. Throughout history, oxidation can also be accelerated via dissolution of photochemically produced percolates [18].

Oxidation rates are proportional to O_2 partial pressure (p), and only limited oxidation may occur during a short episode of aqueous activity and at current atmospheric $pO_2=7\times10^{-6}$ bar. Sulfides and Fe^{2+} salts may precipitate before oxidation. Subsequent aqueous episodes would involve dissolution of these and other reduced minerals followed by some aqueous oxidation. This incremental process eventually leads to sulfates and Fe^{3+} oxides/hydroxides observed in Mars' soil and sedimentary deposits.

In hydrothermal environments caused by impacts [19,20] or magmatic activity, strong atmospheric oxidants should not play a role, and high-*T* oxidation occurs by water, as discussed above. Removal of formed H_2 facilitates formation of Fe^{3+} oxides and may produce sulfates.

Aqueous transfer of elements: Acidic conditions favor aqueous migration of many elements including Fe^{3+}, Al and P compounds, while silica is less mobile. Local occurrences of silica [4,21] and silica coatings implies removal of elements at low pH [11-13]. However, the martian surface may have never been exposed to large volumes of acids (at least at once), and aqueous transfer may have been restricted by freezing, evaporation and neutralization.

Neutral/alkaline solutions could have been more voluminous and accounted for much aqueous transfer during the Noachian and Hesperian. Highly soluble Mg and Na sulfates and Mg, Ca, and Na chlorides would be the most mobile. The thick layered deposits of Mg-rich sulfates in Valles Marineris and some craters [1], as well as chloride deposits [22] imply large-scale aqueous transport. However, an alternative explanation of layered salt-rich deposits is feasible [15].

Despite high solubility of Ca chlorides, aqueous migration of Ca should be limited to sulfate-less environments. Dissolution of Mg sulfates in Ca bearing fluids or dissolution of Ca chlorides in sulfate fluids leads to precipitation of gypsum. This may account for polar gypsum deposits.

Specifics of boiling, evaporation, freezing and precipitation: At present, low atmospheric *p* favors boiling of water at elevations, while lower *p* and/or higher *T* are needed to boil saline solutions. Boiling leads to colder saline fluids, and prolonged boiling may only be associated with near-surface hydrothermal activity associated with a heat source. Evaporation of surface fluids is slow owing to low *T* and low water activity [23] and freezing of surface fluids [11,14] may occur faster than evaporation. Boiling, evaporation and freezing all lead to sequential precipitation of highly-soluble salts (Na-Mg chlorides, Mg, Na sulfates) with minor amounts of other low-solubility solids (e.g., silica, gypsum, Fe^{3+} and Al^{3+} hydroxides, carbonates) which precipitate before high-solubility salts.

Low *T* and low water activity of typical martian fluids would cause oversaturation of solution with respect to many solids (phyllosilicates, carbonates). Magnesite, dolomite and siderite may not precipitate in near-freezing environments. Although oversaturation is less likely for salts, freezing or evaporation is likely to cause fractional rather than equilibrium precipitation. In hydrothermal conditions, precipitation of low-solubility Mg-silicates and $CaSO_4$ led to NaCl fluids; and their release at the surface may account for chloride deposits reported in [22].

Several dynamic environments at the near-surface (release of waters, cooling and degassing of hydrothermal fluids, fluid mixing, and soil-water interaction) would have also led to non-equilibrium precipitation. Martian precipitation would have led to multiple amorphous and semi-crystalline oxide/hydroxide and silicate phases that may have never crystallized. A discrepancy between near-infrared [1-3] and thermal infrared identification of phyllosilicates may be due to their poor crystallinity in some localities [24].

A decrease in CO_2/O_2 ratio in the Noachian atmosphere [16,17] may account for pH-Eh changes in surface waters and in the composition of secondary minerals. For example, a Fe^{3+}-nontronite–montmorillonite–kaolinite sequence in layered rocks in Mawrth Vallis [3] could be explained by those atmospheric changes caused by a decline in solar UV activity.

Summary: Multiple and diverse episodes of aqueous activity led to dramatic chemical transformations and unequilibrated mineralogical assemblages observed in martian materials.

Acknowledgements: I thank Susanne Schwenzer and Amy McAdam for comments. This work is supported by NASA MFR program.

References: [1] Bibring J-P. et al. (2005) *Science, 307*, 1576-1581. [2] Mustard J. et al. (2008) *Nature, 454*, 305-309. [3] Bishop J. L. et al. (2008) *Science, 321*, 830. [4] Squyres S. W. et al. (2008) *Science, 320*, 1063-1065. [5] Boynton W. V. et al. (2009) *LPSC 40*, Abstract #2434. [6] Bridges J. C. et al. (2001) *Space Sci. Rev*., *96*, 365-392. [7] McAdam A. C. et al. (2009) *LPS 40*, Abstract #1032. [8] Mumma M. J. et al. (2009) *Science*, *323*, 1041. [9] Chatain B., Chevrier V. (2007) *Planet. Space. Sci*., *55*, 1246-1256. [10] Segura T. L. et al. (2002) *Science*, *298*, 1977-1980. [11] Zolotov M. Yu., Mironenko M. V. (2007) *JGR, 112*, E07006. [12] Tosca N. J. et al. (2004) *JGR*, *109*, E05003. [13] Hurowitz J. A., McLennan S. M. (2007) *EPSL*, *260*, 432-443. [14] Marion G. M., Kargel J. S. (2008) Cold Aqueous Planetary Geochemistry with FREZCHEM. Springer, 251 pp. [15] Niles P. B., Michalski J. (2009) *Nature Geosci*., *2*, 215-220. [16] Tian F. et al. (2009) *GRL*, *36*, L02205; [17] Kasting J., (2008) AGU Fall Meet. presentation. [18] Hecht M. H. et al. (2009) *LPS 40*, Abstract #2420. [19] Newsom H. E. (1980) *Icarus*, *44*, 207-216. [20] Abramov O., Kring D. A. (2005) JGR, 110, E12S09. [21 Milliken, R. E. et al. (2008) *Geology*, *36*, 847-850. [22] Osterloo M. M. et al. (2008) *Science, 319*, 1651-1654. [23] Sears D. W. G., Chittenden J. D. (2005) *GRL, 32*, L23203. [24] Ruff S. W., Hamilton V. E. (2009) *LPS*, *40*, Abstract #2160.

NOTES

NOTES